

**Creation of a Fermi-Fermi mixture
of dysprosium and potassium
with resonant interactions**

Cornelis Ravensbergen

**Creation of a Fermi-Fermi mixture
of dysprosium and potassium
with resonant interactions**

Cornelis Ravensbergen MSc.



**Creation of a Fermi-Fermi mixture
of dysprosium and potassium
with resonant interactions**

DISSERTATION

by

Cornelis Ravensbergen MSc.

submitted to the Faculty of Mathematics, Computer
Science, and Physics of the University of Innsbruck,
in partial fulfillment of the requirements for the degree of
Doctor of Philosophy (PhD)

Innsbruck, April 2020

Advisor:

Univ.-Prof. Dr. Rudolf Grimm

Abstract

Ultracold Fermi gases represent highly tunable and controllable systems, ideally suited to model intriguing aspects of quantum many-body physics. Strongly interacting fermions are of interest in a large variety of research fields, from primordial matter, neutron stars and atomic nuclei to condensed-matter systems. Particularly enticing is the prospect to further our understanding of superfluids and superconductors. Realizing the strongly interacting regime in quantum-degenerate Fermi gases requires a mixture of two components with strong s -wave interactions, which can be achieved at a Feshbach resonance. Mass-imbalanced Fermi-Fermi gases go beyond the physics of spin mixtures, as they are predicted to favor exotic interaction regimes with unconventional pairing mechanisms.

This thesis reports on the realization of a Fermi-Fermi mixture that combines mass imbalance, tunability, and collisional stability. The constituents of the mixture, dysprosium and potassium atoms, differ in many crucial atomic properties, and these can be used to address, trap, or manipulate them independently. The dynamical polarizability is of fundamental importance for laser trapping, and we measured the dysprosium polarizability at the optical wavelength of 1064 nm. Our method is based on collective oscillations in an optical dipole trap, and it reaches unprecedented accuracy and precision by comparison with potassium as a reference species. We brought the mixture deeply into the quantum-degenerate regime by performing evaporative cooling of the dipolar dysprosium atoms. Potassium atoms are cooled down sympathetically through s -wave collisions with Dy, and we estimated the interspecies background scattering length through cross-species thermalization measurements. We identified a broad Feshbach resonance at a magnetic field of 217 G. Here the expansion from the trap is collisionally hydrodynamic, and the profiles reveal a bimodal behavior resulting from mass imbalance. Lifetime studies on resonance show a suppression of inelastic few-body processes by orders of magnitude, which we interpret as a consequence of the fermionic nature of our system. The work carried out within this thesis paves the way towards the realization of novel states of strongly correlated fermions with mass imbalance.

Contents

1	Introduction	4
2	Research Topics	7
2.1	Cooling Strategies for Fermions	7
2.2	Degenerate Fermi Gases	8
2.3	Feshbach Resonances in Cold Fermionic Gases	8
2.4	Strongly Interacting Fermi Gases	9
2.5	Fermi-Fermi Mixtures	10
2.6	Fermi-Fermi Mixture of Dy and K	10
2.7	Contents of this Thesis	11
3	Publication: Accurate Determination of the Dynamical Polarizability of Dysprosium	14
3.1	Introduction	15
3.2	Dynamical Polarizability	16
3.3	Experimental Setup	18
3.4	Systematic Effects	19
3.5	Determination of the Polarizability	22
3.6	Discussion and Conclusion	23
3.7	Supplemental material	24
3.7.1	Absence of Density Effect on Oscillation Frequency . .	24
3.7.2	Damping of Oscillations	25
3.7.3	Error Budget of the Frequency Ratio Measurement . .	27
3.7.4	Measurement of the Tensor Contribution	28
4	Publication: Production of a degenerate Fermi-Fermi mixture of dysprosium and potassium atoms	30
4.1	Introduction	31
4.2	Laser Cooling and Dipole Trap Loading	33
4.2.1	Magneto-Optical Traps	33
4.2.2	Sequential Dipole Trap Loading	35
4.3	Evaporative Cooling	36

4.3.1	Transfer from Reservoir into Main Dipole Trap	37
4.3.2	Evaporative Cooling of a Pure ^{161}Dy Cloud	38
4.3.3	Evaporative Cooling of the ^{161}Dy - ^{40}K Mixture	41
4.3.4	Effect of Magnetic Levitation	44
4.3.5	Interspecies Scattering Cross Section	48
4.4	Conclusion and Outlook	50
4.5	Appendix	51
4.5.1	Apparatus	51
4.5.2	Imaging of the Atomic Cloud	52
4.5.3	Cooling ^{40}K on the D1 Line	52
4.5.4	Interspecies Thermalization	54
5	Preprint: Resonantly Interacting Fermi-Fermi Mixture of ^{161}Dy and ^{40}K	56
5.1	Introduction	57
5.2	Sample Preparation	59
5.3	Interaction Characterization	59
5.4	Hydrodynamic Expansion	60
5.5	Lifetime	63
5.6	Discussion and Conclusion	65
5.7	Supplemental Material	66
5.7.1	Feshbach resonance scenario	66
5.7.2	Decay	74
5.7.3	Interaction-induced contraction	78
A	Experimental Setup	82
A.1	Design Considerations	82
A.2	Vacuum Chambers	83
A.2.1	Dy Oven Chamber	84
A.2.2	K 2D-MOT Chamber	85
A.2.3	Main Chamber	86
A.2.4	Viewports	87
A.3	Dy Transverse Cooling	89
A.4	Dy Zeeman Slower	89
A.5	Potassium 2D MOT	92
A.6	Dysprosium Laser Setup	94
A.6.1	Dy 421 nm Setup	94
A.6.2	Dy 626 nm Setup	95
A.7	Potassium Laser Setup	97
A.7.1	K D2 setup	97
A.7.2	K D1 Setup	99
A.8	MOT Optics	100
A.9	Optical Dipole Traps	101
A.9.1	Reservoir Dipole Trap	101

A.9.2 Science Dipole Trap	102
A.10 Magnetic Coils	103
A.10.1 Gradient Coil	103
A.10.2 Feshbach Coil	104
A.10.3 Curvature Coil	105
A.10.4 Jump Coil	105
A.10.5 Offset Coil	106
A.11 Imaging and Data Analysis	106
A.11.1 Horizontal Imaging	106
A.11.2 Vertical Imaging	107
A.11.3 Data Analysis	107
Bibliography	109
Acknowledgement	129

Chapter 1

Introduction

Science operates at the boundary of human knowledge, trying to push this boundary further and further away. A large effort in contemporary quantum physics is to gain better insight of macroscopic phenomena through a deeper understanding of the underlying microscopic system. This bottom-up approach has been very successful to explain, for example, superconductivity in metals through the Bardeen–Cooper–Schrieffer (BCS) theory [1], the integer quantum Hall effect [2] and purely 2D materials like graphene [3]. Many unanswered questions remain in very diverse topics. In solid-state physics they range from electron pairing different from the BCS type, and the interplay between magnetic ordering and conductivity. Both of these feature in high-temperature superconductivity [4], while the latter is vital for the giant magnetoresistance effect [5]. Another very diverse topic is the influence of topology on macroscopic properties like the phase diagram and transport.

A better understanding of even small parts of these systems holds great potential to develop novel technologies vastly improving areas like computation, data and energy storage, or energy transport. In solid-state systems, however, this usually is a very challenging task, because measuring microscopic properties is often impossible because of the extremely fast timescales (on the attosecond level), very short length scales (sub-nanometer) and imperfections in sample preparation or impurities. The result is that it can be hard to probe the validity of different models that try to explain a certain phenomenon.

There is another way to use the bottom-up approach: Through so-called quantum simulation, as proposed by Nobel laureate Richard Feynman [6],

one tries to engineer microscopic models directly in a well-controlled environment to measure macroscopic properties. For this method to work one needs a highly flexible, well resolved, and controllable system. A prime candidate that fulfills these requirements are systems of cold atoms in the quantum-degenerate regime.

The field of ultracold quantum gases has seen many breakthroughs, for example: the creation of a Bose-Einstein condensate (BEC) both with free atoms [7–9] and weakly bound molecules [10–12], and also the realization of a quantum phase transition [13]. The determination of the equation of state of a unitary Fermi gas [14–16] and the demonstration that this system remains superfluid through the BEC to BCS crossover. Cold atoms were also used to create a novel type of three-body bound state called an Efimov trimer [17, 18]. Bosons, in contrast to Fermions, also show novel behavior if the interactions are reduced, a BEC collapses [19], but sometimes stabilizes to liquid droplets [20] or can even become a supersolid [21–23]. By adding a periodic potential cold atoms were used to create the anti-ferromagnetic Neel ordered state [24], and by gradually adding a disordered potential one can observe localization [25].

The advances in cold atom research are also driven by metrological and technological applications, as colder and larger samples give a significant gain in resolution and precision. Optical lattice clocks use an optical transition as an ultra-stable reference to measure time, and are the current state-of-the-art with a fractional stability below 10^{-18} in a one-second integration time [26]. Matter-wave interferometry shows a much higher sensitivity to measure forces and accelerations than more conventional photonic interferometers [27]. Magnetic field sensors can be improved by orders of magnitude when based on an atomic gas [28].

Strongly interacting fermionic systems constitute a very rich and active field of research. Typical examples of such systems are the interior of neutron stars, quark-gluon plasmas and high-Tc superconductors [29], for all of which our current understanding is limited and large scale theoretical modeling is not possible. These vastly different environments could however share a single common underlying physical description through the universality of strongly interacting Fermi systems.

Spin mixtures of fermionic cold atoms become universal when the interactions, quantified by the scattering length, become larger than the inter-particle spacing. An important feature of cold atoms is that this scattering length can be tuned through a Feshbach resonance. Two different atomic species have been brought into this regime: lithium-6 and potassium-40,

both being alkali metals [30]. Both species feature a strong Feshbach resonance between the two lowest Zeeman states, and exhibit exceptional collisional stability in the universal regime. This enabled the study of BCS-type pairing (for negative scattering length), the formation of a molecular BEC (positive scattering length) and the smooth crossover between the BCS and BEC side of the resonance [31].

When the two constituents of the strongly interacting Fermi system are not two spin states but different species, the physics becomes much richer. The mass imbalance leads to an imbalanced Fermi surface between the two components, which enables novel types of pairing [32, 33]. In addition, mixed dimensional systems become accessible via species-selective potentials.

The realization of such a two species Fermi-Fermi mixture remains challenging because of the lack of a suitable Feshbach resonance in the only possible bi-alkali metal mixture of ${}^6\text{Li}$ and ${}^{40}\text{K}$. We therefore decided to set up a new experiment with a novel mixture of dysprosium and potassium. This combination features a mass imbalance with a factor of four, and both these species have been separately brought to quantum degeneracy. Dysprosium features two fermionic isotopes, which effectively doubles the chances of finding a suitable Feshbach resonance. In this thesis, a pathway to achieving a strongly interacting Fermi-Fermi mixture is shown through multiple published results, and in addition an overview of the setup is presented.

Chapter 2

Research Topics

This chapter aims to give a broad overview of the research field in which the experiments, in this thesis, were performed and introduces the underlying research topics. The research field of cold Fermi gases is introduced with a historical overview, starting with different cooling strategies discussed in Sec. 2.1, and continues with deeply degenerate Fermi gases in Sec. 2.2. The exploration of strong Feshbach resonances, presented in Sec. 2.3, in combination with degenerate Fermi systems has led to remarkable breakthroughs which are discussed in section 2.4. Section 2.5 details the large theoretical and experimental interest in strongly interacting mixtures of different fermionic species, and some of the achievements of this field are listed. Finally, Sec. 2.6 discusses the need for a new Fermi-Fermi experiment and the search for a suitable species combination.

2.1 Cooling Strategies for Fermions

Identical fermions scatter in odd partial waves, and when the temperature becomes lower than the p -wave barrier the scattering cross section for fermions interacting through a contact interaction potential vanishes [34]. Reaching very low temperatures with fermionic gases therefore requires an additional component: either another species through sympathetic cooling, or another spin state, or long-range interactions, like for example a dipole-dipole interaction. The first two methods both rely on a sufficiently large s -wave scattering length, in the case of sympathetic cool to allow for inter-species thermalisation, and in the case of a spin mixture to enable evaporative cooling [35]. Dipole-dipole interactions give rise to dipolar scattering which features a non-vanishing scattering cross section, even in the zero-temperature limit [36].

2.2 Degenerate Fermi Gases

All of the three cooling strategies mentioned in the previous section have been successfully used to create degenerate Fermi gases (DFG). While the transition of a thermal Bose gas into a BEC is characterized by a phase transition with a critical temperature, a thermal non-interacting Fermi gas gradually changes into a DFG [34]. This change can still be characterized by the phase-space density reaching unity, and the associated temperature is called the Fermi temperature. In 1999, a spin mixture of potassium-40 atoms was brought to degeneracy [37], while a little later lithium-6 also reached degeneracy by sympathetic cooling via the bosonic isotope (^7Li) [38, 39]. These two species are the only stable fermionic alkali metals, and they form the bedrock of this research field. Ytterbium has also been brought to degeneracy in a spin mixture [40]. Reaching degeneracy through sympathetic cooling has been very successful for many different atomic species: He [41], Sr [42, 43], Cr [44] and Dy [45]. And recently a cloud of fermionic KRb molecules has reached degeneracy [46], through molecule formation from a double degenerate mixture of ^{40}K and ^{87}Rb . Strongly magnetic lanthanides can reach a DFG through sympathetic cooling [45], or through universal dipolar scattering, to creating a single spin, single species DFG, as has been achieved for Er [47] and Dy [48].

2.3 Feshbach Resonances in Cold Fermionic Gases

When the energy of a bound (e.g. molecular) state, called the closed channel, coincides with the energy (at large separation) of two colliding free atoms, called the open channel, a very small coupling leads to severe modification of the scattering properties of the two free atoms. This process is called a Feshbach resonance (FB) [49, 50], and the energy difference between the closed and open channel can usually be tuned, either by a magnetic field, or by other means, like for example optical methods. For atoms interacting through a contact potential the scattering at low temperatures is fully defined by the s -wave scattering length a which shows a divergence at a Feshbach resonance, while the width of the resonance is characterized by Δ [50]. In bosonic systems Feshbach resonances are associated with strong losses due to the a^4 scaling of the three-body loss rate coefficient. Fermionic systems, however, not only show a remarkable stability near a strong Feshbach resonance, but can be even long lived on either side of the resonance, this in stark contrast to a BEC which is only stable for positive a .

2.4 Strongly Interacting Fermi Gases

Early experiments with resonantly interacting Fermi gases focused on realizing molecular condensates and fermionic superfluids. After investigating the resonance location and observing collisional hydrodynamic expansions [51], several groups managed to create molecular Bose-Einstein condensates [10–12]. The superfluidity across the resonance was probed through pair condensation [52], collective modes [53, 54], pairing gap measurements [55, 56] and finally vortices [57]. The presence of vortices provided an unambiguous demonstration that the system was superfluid on resonance, and it remained superfluid while tuning the scattering length continuously through the BEC to BCS crossover. After this breakthrough many more aspects of the strongly interacting superfluid were probed, for example the investigation of sound showed a critical sound velocity [58], and a special type of heat propagation called second sound [59]. Transport properties were also studied in a narrow channel between two reservoirs, both in a 2D channel [60], and in a quantum point contact [61]. Also spin transport was investigated in strongly interacting Fermi gases [62]. The equation of state of a unitary Fermi gas has been measured [14, 15] with increasing precision [16], marking a highlight in determining universal physical relations.

Exploration of the full phase diagram continued to a population imbalanced case, here phase separation was observed in a harmonic trap leading to a fully paired superfluid core [63]. At unitarity the phase diagram [64] of the population imbalanced Fermi gas has been measured. Population imbalance naturally leads to unmatched Fermi surfaces between the two spin states, and it is expected to allow for novel types of pairing, beyond the BCS type [65]. Unfortunately the required temperatures for three-dimensional systems are far below the current experimental conditions, efforts in lower dimensions continue however [66].

Recently high resolution imaging was implemented on DFG experiments with an optical lattice, reaching single-site and single atom resolution [67]. This realizes the Hubbard Hamiltonian, which considers spin 1/2 particles on a lattice with short-range interactions. The phase diagram of this Hamiltonian is largely unknown, with a confirmed anti-ferromagnetic Mott insulator phase [68], and a, as yet unobserved, superconducting phase. The Hubbard Hamiltonian features an interesting interplay between magnetism and superfluidity, which is thought to also play an important role for high-Tc superconducting cuprates [69], and is expected to enable novel many-body phases [70].

2.5 Fermi-Fermi Mixtures

For novel types of pairing and the resulting exotic phases, mass imbalance is predicted to offer a much higher critical temperature as compared to the mass-balanced case. The phase diagram is strongly modified when there is a mass imbalance between the two types of fermions [32, 33]. These experimentally accessible temperatures, together with the added tunability and probing flexibility of having two different species, kindled the construction of the only possible bi-alkali metal Fermi-Fermi mixture of ${}^6\text{Li}$ and ${}^{40}\text{K}$ [71–73]. The mixture with a non-alkali metal of ${}^6\text{Li}$ and ${}^{173}\text{Yb}$ [74] focuses more on creating cold molecules and exploiting the very large mass imbalance for Efimov and impurity physics. Recently narrow Feshbach resonances were found in this mixture [75]. The isotopic mixture of ${}^{171}\text{Yb}$ and ${}^{173}\text{Yb}$ has also realized [76], showing the versatility and possibilities of the large number of isotopes ytterbium offers.

A thorough search for suitable Feshbach resonances in the ${}^6\text{Li}$ - ${}^{40}\text{K}$ mixture followed, but the stability of the mixture was shown to be insufficient near the rather narrow resonance [77, 78]. Broad Feshbach resonances are highly desirable, beyond the ease-of-use in field stability, since they allow for strong loss suppression due to Pauli blocking [79]. Both ${}^6\text{Li}$ [80, 81] and ${}^{40}\text{K}$ [82] with their respective intraspecies broad Feshbach resonances show this strong loss suppression.

The limited lifetime around unitarity of this bi-alkali mixture makes the realization of novel quantum phases in the bulk a yet unrealized goal, but the strongly interacting regime was explored however, and hydrodynamic effects were observed in the expanding clouds [83]. The mass imbalance was shown to have a dramatic effect on the atom-dimer interaction on the repulsive side of the resonance [84] and the suppression of losses [78]. In the case of an extreme population imbalance, the system, consisting of a few impurities interacting strongly with a Fermi sea, realizes a paradigmatic quasi-particle called a polaron [85].

2.6 Fermi-Fermi Mixture of Dy and K

The exciting theoretical prospects of a strongly interacting Fermi-Fermi mixture motivates another experimental search for a suitable atomic mixture. Since ${}^6\text{Li}$ and ${}^{40}\text{K}$ are the only two fermionic alkali metals, a novel Fermi-Fermi mixture would need at least one non-alkali metal. Strontium and ytterbium both have been very successful in creating large degenerate Fermi gases, but due to their completely filled outer electron shell do not exhibit broad Feshbach resonances [86, 87]. The only other atomic species that

have been brought to Fermi degeneracy are Cr [44], Er [47], Dy [45], and metastable He [41]. Metastable helium needs a very large apparatus for cooling and trapping and, when mixed, could have strong collisional relaxation processes leading to losses. Chromium only very recently reached degeneracy due to the complex laser cooling scheme required for the fermionic isotope [44]. Making a deeply degenerate Fermi-Fermi mixture with Cr is therefore also complex, however, new attempts are on the way to create a Cr-Li mixture [88]. Apart from the possible cooling strategies the most important consideration when choosing an atomic mixture is the mass ratio. The combination of either Er or Dy with Li would have such an extreme mass imbalance that three-body interactions are expected to lead to losses [78, 89], while the combination between Er and Dy does not feature a sizable mass ratio at all.

A good choice to create a novel Fermi-Fermi mixture with an enhanced chance of success is a mixture of dysprosium and potassium, because Dy has two fermionic isotopes as opposed to only one for Er. This mixture has a mass ratio of about four, and therefore the interactions are strongly modified as compared to the equal mass case. The ground-state of Dy has a non-zero orbital angular momentum, which allows for the possibility of many Feshbach resonances [90]. Dysprosium, being part of the lanthanide series, features many suitable laser cooling transitions [91] ranging from very broad, to very narrow, making it ideally suited for advanced laser cooling schemes. And finally, the large magnetic dipole moment of $10 \mu_B$ enables spin-polarized evaporative cooling, simplifying the evaporative cooling strategy of the mixture, as only a single interspecies scattering process has to be taken into account. In addition, if both species are spin-polarized in their lowest Zeeman level, two-body loss processes are completely eliminated from the system.

2.7 Contents of this Thesis

This thesis describes the steps that were taken to develop a new cold atomic mixture experiment. No previous mixture between a lanthanide and alkali atom existed, and therefore many of the mixture's properties and experimental sequence optimizations had to be measured and characterized. The mixture of dysprosium and potassium atoms is in many ways much more complex than a bi-alkali atom mixture, featuring for example, strong dipole-dipole interactions and high angular-momentum states. This complicated nature, in combination with the novelty of the mixture has the consequence that not many theoretical models nor calculations exist. The methods used in this thesis to characterize the dysprosium properties, and that of the mixture, are therefore very general, and could also be applicable to other cases

where thorough theoretical knowledge is absent, like molecules and other complicated atomic species.

Chapter 3 gives a detailed account of our method to accurately determine the scalar and tensor polarizability of dysprosium at 1064 nm. Multiple theoretical calculations existed on the dysprosium polarizability, however, accurate measurements are very challenging in single species experiments. Potassium plays a key role in this chapter, since it allows us to directly compare its known polarizability with the unknown dysprosium one. The ratio of the trap frequencies of two species in a harmonic trap only depends on the polarizability and mass ratios, and it can therefore be used to determine the unknown polarizability. We measure the trap frequency by exciting a center-of-mass oscillation by shifting the single beam dipole trap slightly, the momentum of the cloud is then measured, using time of flight, after letting the cloud oscillate for a variable time. Our dipole trap only approximates a harmonic trap in its center, and if the cloud explores the non-harmonic parts of the trap, either through a large oscillation amplitude, or when the cloud size is large due to its finite temperature, the measured oscillation frequency deviates from the trap frequency. We measure and take these anharmonicity effects into account as it affects both species differently, before taking the frequency ratio to determine the polarizability.

Chapter 4 explains and characterizes our experimental sequence to create a doubly degenerate Fermi-Fermi mixture. We start by loading a magneto-optic trap for each species sequentially and we then mix and store the two spin-polarized species in a large volume reservoir trap. During a short evaporation sequence we transfer both into a more tightly focused crossed dipole trap, where the rest of the evaporation down to degeneracy takes place. We utilize the strong dipole moment of dysprosium to enable evaporative cooling of a spin-polarized Fermion, while potassium is cooled down by being in thermal contact with the dysprosium cloud. The sympathetic cooling of potassium works in our case because dysprosium has a lower polarizability and higher mass, both leading to a much lower trap depth for dysprosium. We measure the thermalization rate between the potassium and dysprosium and determine an estimate on the background interspecies scattering length.

Chapter 5 describes the strongly modified behaviour of the expansion dynamics of a resonantly interacting Fermi-Fermi mixture. The divergence of the interaction strength at a Feshbach resonance gives rise to hydrodynamic behavior during the free expansion from the trap, and we observe a markedly different cloud profile in our lighter, minority, component as compared to the mass-balanced case. The observed non-Gaussian distribution of

the potassium cloud is fully quantified by simulating the expansion on resonance with a Monte-Carlo simulation. We measure the position and width of the Feshbach resonance through interspecies thermalization, and this data in combination with a resonant scattering model give us the behavior of the interspecies scattering length in the considered magnetic field region. The collisional stability of the mixture near the resonance is measured by performing loss-spectroscopy.

Appendix A concludes this thesis with a broad overview of the different components of the experimental setup with which all described experiments were performed. The design and construction of a new cold atom experiment is a very time intensive task, as it involves many different technologies to make a double degenerate mixture of cold atoms. These technologies range from an extensive ultra-high vacuum setup, numerous laser setups, precision high-current manipulation, time critical sequence control and image acquisition and data extraction.

Chapter 3

Publication: Accurate Determination of the Dynamical Polarizability of Dysprosium

Published as:

C. Ravensbergen, V. Corre, E. Soave, M. Kreyer, S.
Tzanova, E. Kirilov, and R. Grimm.
[Phys. Rev. Lett. **120**, 223001 \(2018\)](#)

Author contribution: The author took a leading role in the process of acquiring and analyzing the data described in this publication as well as writing the manuscript.

Changes with respect to the published version: Subsection headlines have been added.

We report a measurement of the dynamical polarizability of dysprosium atoms in their electronic ground state at the optical wavelength of 1064 nm, which is of particular interest for laser trapping experiments. Our method is based on collective oscillations in an optical dipole trap, and reaches unprecedented accuracy and precision by comparison with an alkali atom (potassium) as a reference species. We obtain values of 184.4(2.4) a.u. and 1.7(6) a.u. for the scalar and tensor polarizability, respectively. Our experiments have reached a level that permits meaningful tests of current theoretical descriptions and provides valuable information for future experiments utilizing the intriguing properties of heavy lanthanide atoms.

3.1 Introduction

The dipole polarizability is a quantity of fundamental importance in light-matter interaction, as it characterizes the linear response of a neutral particle to an electric field. The polarizability is related to other important physical quantities, like the van-der-Waals dispersion coefficient, and its knowledge is of great relevance for a deep understanding of many-electron systems, for example in heavy atoms, molecules, and clusters [92]. The static polarizability characterizes the response to a constant electric field by a single real number. The dynamic polarizability (DP) describes the response to an oscillating field and is represented by a complex frequency-dependent function. Naturally, the DP is much richer and contains much more information on the properties of a particle, in particular on its resonance behavior. While various different methods have been established to measure the static polarizability with high accuracy [93, 94], measurements of dynamic polarizabilities are notoriously difficult. Accurate laser-spectroscopic methods only provide access to differential polarizabilities, whereas other methods like deflection from a laser beam suffer from the problem of characterizing the interaction region well enough.

In the realm of ultracold atoms, both the real and imaginary part of the DP play an essential role for controlling the external and internal atomic degrees of freedom. The imaginary part is related to the absorption and scattering of light. The real part gives rise to Stark shifts, which are primarily utilized for constructing optical dipole traps [95] in a wide range of different geometries. Zero crossings of the DP, which occur at tune-out wavelengths, can be used to engineer species-selective traps [96]. Optical lattice clocks operate at a so-called magic wavelength, where the differential DP between the two relevant atomic states vanishes [97]. The DP also enables coherent spin manipulation, which is the basis of many spin-orbit coupling schemes [98].

The optical manipulation of ultracold magnetic lanthanide atoms has attracted considerable interest [20, 45, 99–105]. Their exceptional magnetic properties arise from a partially filled, submerged 4f shell. They feature a very rich atomic spectrum, including narrow optical transitions, and a large orbital angular momentum gives rise to substantial non-scalar contributions to the polarizability. These special properties make magnetic lanthanide atoms excellent candidates to implement advanced light-matter coupling schemes, such as spin-orbit coupling [48, 106], and to realize novel regimes of quantum matter. The electronic configuration makes advanced calculations of the DP very challenging and interesting [107–112]. To benchmark theoretical models, measurements are highly desirable with uncertainties on the percent level. Experimental results have been reported for dysprosium [100, 113, 114], thulium [109, 112] and erbium [115], in the latter case also demonstrating the anisotropic nature of the DP. However, all these measurements have been subject to large systematic uncertainties, imposed by the methods at hand.

In this Letter, we report on the accurate determination of the real part of the DP of a magnetic lanthanide atom at a wavelength of particular interest for cooling and trapping experiments. We investigate dysprosium atoms and utilize an idea often applied in precision metrology, performing a measurement relative to a known reference. As a reference species, we use potassium atoms, for which the DP is known on the permille level, and measure the trap frequencies of both species in the same single-beam optical dipole trap (ODT). The frequency ratio is then independent of major experimental systematics and imperfections. In a further set of experiments, we determine the tensor contribution to the DP.

3.2 Dynamical Polarizability

The interaction of atoms with the electric field \vec{E} of laser light is described by the Hamiltonian $H = -\frac{1}{2}\vec{E}^\dagger\vec{\alpha}\vec{E}$, where $\vec{\alpha}$ is the dynamical polarizability tensor operator [116]. The energy shift for a given quantum state corresponds to the optical trapping potential and is

$$U(\mathbf{r}, \omega_L) = -\frac{2\pi a_0^3}{c} I(\mathbf{r}) \tilde{\alpha}(\omega_L), \quad (3.1)$$

where ω_L is the laser frequency, $I(\mathbf{r})$ the position-dependent intensity, a_0 the Bohr radius, and c the speed of light. Here we define $\tilde{\alpha}(\omega_L)$ as a dimensionless quantity corresponding to the real part of the DP of the quantum state of interest in atomic units (1 a.u. = $4\pi\epsilon_0 a_0^3$, where ϵ_0 is the vacuum permittivity). For a Gaussian laser beam, the central region (trap depth \hat{U}) can be approximated by a harmonic potential. The corresponding radial

trap frequency

$$\omega_r = \sqrt{\frac{4\hat{U}}{mw_0^2}} = \sqrt{\frac{16a_0^3 P \tilde{\alpha}(\omega_L)}{c w_0^4 m}} \quad (3.2)$$

is determined by the laser beam parameters (power P and waist w_0) and atomic properties (polarizability $\tilde{\alpha}$ and mass m) [95].

The DP can generally be decomposed into the three irreducible contributions $\tilde{\alpha}_S$, $\tilde{\alpha}_V$, and $\tilde{\alpha}_T$ (scalar, vector, and tensor polarizability), with weights depending on the angular momentum quantum numbers and the polarization of the trapping light. In our work, we focus on the elementary case of linearly polarized light and atoms in a stretched state ¹, where we can decompose $\tilde{\alpha}$ into

$$\tilde{\alpha}(\omega_L) = \tilde{\alpha}_S(\omega_L) + \frac{3\cos^2\theta - 1}{2}\tilde{\alpha}_T(\omega_L); \quad (3.3)$$

here θ is the angle between the polarization axis and the quantization axis, the latter being defined by the magnetic field. Note that within a hyperfine manifold $\tilde{\alpha}_S$ and $\tilde{\alpha}_T$ only depend on the wavelength.

The usual method to measure the dynamical polarizability in an ODT [100, 109, 112, 113, 115] is to determine the trap frequency ω_r by observing collective oscillations in a trap with a given power P and a well-defined waist w_0 , and to use Eq. (3.2). A major complication arises from the strong dependence $\tilde{\alpha} \propto w_0^4$. An accurate determination of w_0 at the position of the atoms is crucial, but very difficult to achieve in practice. In addition, any aberrations from an ideal Gaussian beam are not accounted for. Moreover, a real cloud with its finite spatial extent will experience some anharmonicity, which will alter the measured oscillation frequency. The combination of these systematic problems typically limits the accuracy of such DP measurements to a few 10% [115].

The above limitations can be overcome by referencing the trap frequency of the particle of interest (or state [117]) to a species with a known polarizability [118, 119]. Figure 3.1 illustrates the situation for two species in the same optical trapping field, where different potential depths result from the different polarizabilities. Within the harmonic trap approximation, the DP of the unknown species, in our case Dy, is then obtained as

$$\tilde{\alpha}_{\text{Dy}} = \tilde{\alpha}_{\text{K}} \frac{m_{\text{Dy}}}{m_{\text{K}}} \left(\frac{\omega_{\text{Dy}}}{\omega_{\text{K}}} \right)^2, \quad (3.4)$$

¹Angular momentum projection on the quantization axis equals plus or minus the total angular momentum ($|m_J| = J$)

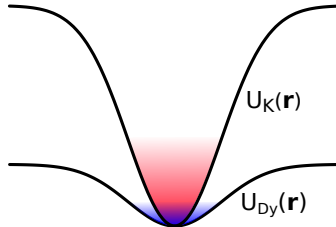


Figure 3.1: Schematic illustration of the species-dependent optical trapping potential U filled with potassium or dysprosium atoms in a beam with a Gaussian profile. Here, in the ideal case, the ratio T/\hat{U} is equal for the two species, the atoms explore exactly the same region in the trap, and thus experience the same anharmonicity and beam aberrations.

where $\tilde{\alpha}_K$ is the polarizability of the reference species (in our case K), and m_{Dy}/m_K is the known mass ratio. Experimentally, one only has to measure the frequency ratio $\omega_{\text{Dy}}/\omega_K$, which eliminates the need to determine w_0 or P . This scheme also removes the effects of anharmonicity provided that the ratio of the temperature to the trap depth is the same for both species. In this ideal case, illustrated in Fig. 3.1, the two thermal clouds fill exactly the same region in the trap, and thus experience the same relative effect of anharmonicity. Introducing another species with a different mass may lead to a different gravitational sag and thus to a shift of the frequency ratio. This effect, however, can be suppressed by using a sufficiently deep and tight trap.

3.3 Experimental Setup

In our experiments, we use the isotopes ^{164}Dy and ^{40}K , with a mass ratio $m_{\text{Dy}}/m_K = 4.102$. For trapping we use the standard near-infrared wavelength of 1064.5 nm. At this wavelength the polarizability of potassium is $\tilde{\alpha}_K = 598.7(1.1)$ [120, 121]². Based on the available theory values for Dy [107, 110], we can estimate $\tilde{\alpha}_K/\tilde{\alpha}_{\text{Dy}} \approx 3.2$ and $\omega_K/\omega_{\text{Dy}} \approx 3.6$.

We produce a thermal cloud of either ^{164}Dy or ^{40}K atoms in a single-beam ODT. For dysprosium, we employ a laser cooling and trapping scheme similar to Refs. [105, 122]. After loading the ODT and some evaporative cooling, we typically trap 10^6 atoms, spin-polarized in Zeeman substate $|J = 8, m_J = -8\rangle$, at about $8 \mu\text{K}$. For potassium, after a sub-Doppler

²At 1064.5 nm the polarizability of potassium is without any significant tensor contribution

cooling stage [123] which also enhances ODT loading, we have 3×10^5 unpolarized 2 atoms at $\sim 30 \mu\text{K}$. The trapping laser (Mephisto MOPA 18 NE) operates on a single longitudinal mode, is linearly polarized, and its power is actively stabilized. All measurements reported here are performed with $P = 2.5 \text{ W}$, $w_0 \approx 30 \mu\text{m}$, and a magnetic field strength of 250 mG.

We measure the trap frequencies by exciting a center-of-mass (CoM) oscillation, the so-called sloshing or dipole mode. In a harmonic potential, this mode does not involve a compression of the cloud and the frequency is thus not affected by the interactions within the cloud or by its quantum statistics [124]. We excite a pure radial sloshing oscillation by displacing the trap position abruptly in the vertical direction using an acousto-optic modulator. The displacement amounts to approximately $2 \mu\text{m}$, which is smaller than the in-trap radial cloud size of about $\sigma_r = 6 \mu\text{m}$. After a variable hold time we switch off the trap and perform standard time-of-flight (ToF) absorption imaging. The cloud position is extracted from the images by performing a one-dimensional Gaussian fit to a vertical slice taken from the central part of the elongated trap. Both species are imaged using the same optical path and camera.

A typical measurement run for both dysprosium and potassium is shown in Fig. 3.2. The magnetic field is chosen to be parallel to the polarization of the trapping light ($\theta = 0$), and therefore from Eq. (3.3) we get $\tilde{\alpha} = \tilde{\alpha}_S + \tilde{\alpha}_T$. We fit the oscillations with an exponentially damped sine wave to extract the frequency ω^{fit} and the damping time τ of the oscillation. The two species oscillate at different frequencies because of their different mass and polarizability. By relative scaling of the horizontal axes of Fig. 3.2 with the expected factor of 3.6 the oscillations exhibit a nearly identical behavior. This already confirms that the theoretical values of Refs. [107, 110] provide a good estimate for the Dy polarizability. The identical damping behavior, with $\omega^{\text{fit}}\tau$ being the same for both species, is consistent with our assumption that the main source of damping is dephasing resulting from the trap anharmonicity 3.7.

3.4 Systematic Effects

The measured frequency ratio exhibits a residual anharmonicity effect. After trap loading, plain evaporative cooling reduces the temperature to a certain fraction of the trap depth. This effect is similar, but not exactly equal for both species. We take this into account by a small correction to the dysprosium oscillation frequency. For a given potassium temperature T_K the corresponding dysprosium temperature would be $(\tilde{\alpha}_{\text{Dy}}/\tilde{\alpha}_K)T_K$. A deviation from this ideal value can be quantified by $\Delta T_{\text{Dy}} = T_{\text{Dy}} - (\tilde{\alpha}_{\text{Dy}}/\tilde{\alpha}_K)T_K$. The

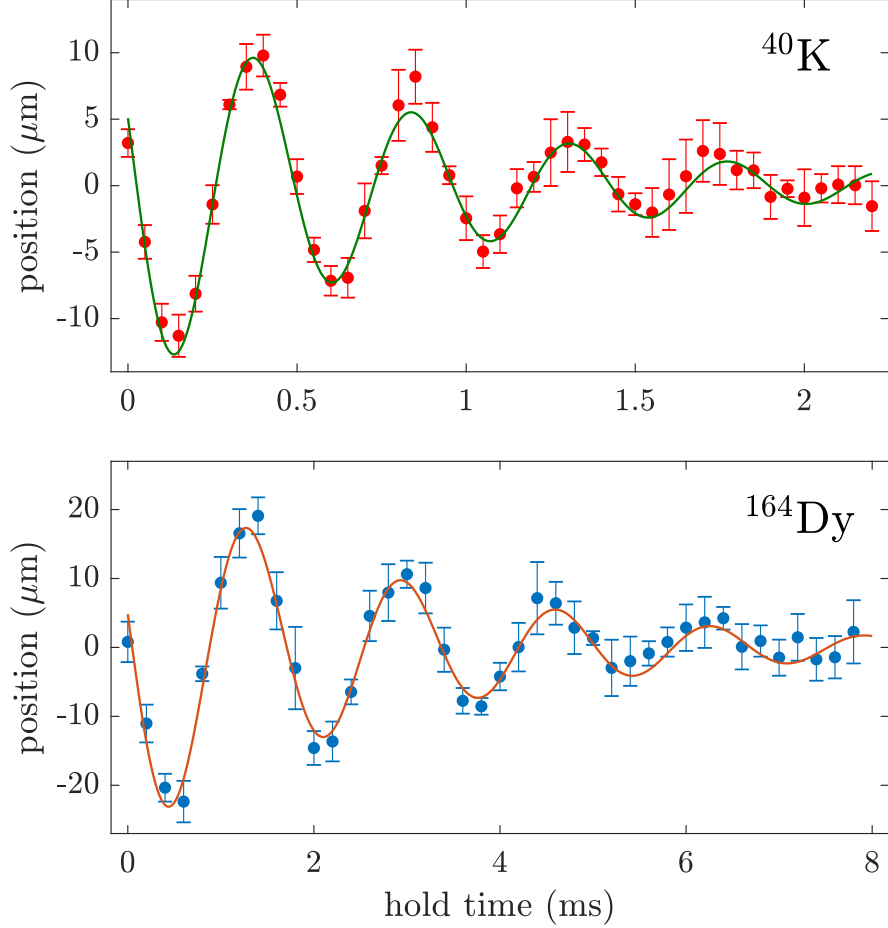


Figure 3.2: Radial sloshing mode oscillation for potassium and dysprosium. The cloud position after ToF is plotted against the hold time in the trap after the excitation. We obtain $\omega_{\text{K}}^{\text{fit}}/2\pi = 2140(10)$ Hz and $\omega_{\text{Dy}}^{\text{fit}}/2\pi = 601(2)$ Hz, $\tau_{\text{K}} = 0.8(1)$ ms and $\tau_{\text{Dy}} = 2.9(1)$ ms. The temperatures are $T_{\text{K}} = 36(3)$ μK and $T_{\text{Dy}} = 8.3(2)$ μK , and the ToF is 0.3 ms for K and 2 ms for Dy. Note that the time scales for K and Dy differ by a factor of 3.6. The error bars show the sample standard deviation of five individual measurements at the same hold time.

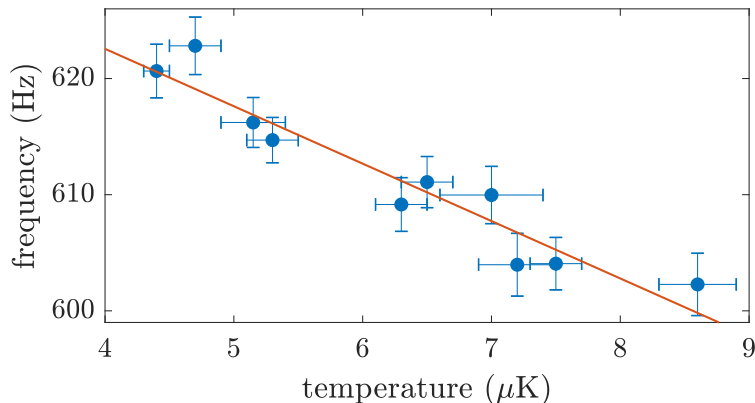


Figure 3.3: Anharmonicity effect on the trap frequency. The Dy CoM oscillation frequency is plotted as a function of the cloud temperature. The weighted linear fit takes both frequency and temperature errors into account, and for the displayed set of measurement yields a slope $\beta/2\pi = -5.1(7)\text{Hz}/\mu\text{K}$.

anharmonic frequency shift depends on the slope $\beta = d\omega_{\text{Dy}}/dT_{\text{Dy}}$, which gives a corrected frequency ratio

$$\frac{\omega_{\text{K}}}{\omega_{\text{Dy}}} = \frac{\omega_{\text{K}}^{\text{fit}}}{\omega_{\text{Dy}}^{\text{fit}} - \beta\Delta T_{\text{Dy}}}. \quad (3.5)$$

With this correction, Eq. (3.4) allows to determine $\tilde{\alpha}_{\text{Dy}}/\tilde{\alpha}_{\text{K}}$ in an accurate way.

In order to determine β , we vary the temperature of the dysprosium atoms and measure the oscillation frequency. The temperature, determined by standard TOF expansion, is changed by an evaporation ramp down to a variable trap power followed by a re-compression to the standard power and a hold time for thermalization. We observe a frequency decrease with increasing temperature, as is shown in Fig. 3.3. From this set of measurements and a second one taken under similar conditions (not shown in Fig. 3.3), we obtain the combined result $\beta/2\pi = -4.5(4)\text{Hz}/\mu\text{K}$. Note that the anharmonicity shifts the measured Dy frequency, for our typical temperatures and trap depth, by about 5% as compared to the harmonic approximation of Eq. (3.2).

Possible remaining systematics affecting the frequency ratio could include density-dependent interactions, the finite excitation amplitude, and the effect of gravity. We do not observe a density dependence of the oscillation frequency of Dy when varying the atom number over a wide range 3.7, confirming that the frequency shift observed in Fig. 3.3 can be fully attributed

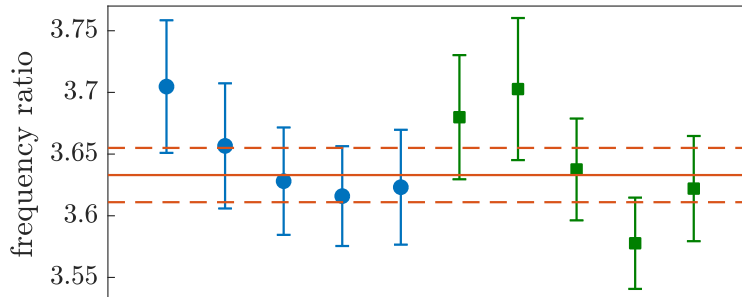


Figure 3.4: Repeated measurements of the frequency ratio ω_K/ω_{Dy} , including small anharmonicity corrections. The two symbols (blue dots and green squares) represent the data sets taken on two different days. The error bars include the fit errors of the frequency measurements and all uncertainties in the anharmonicity correction. Because of the latter, the uncertainties are partially correlated, which we properly take into account in our data analysis when combining the individual results. The solid line marks the final result $\omega_K/\omega_{Dy} = 3.632(22)$, with the dashed lines indicating the corresponding error range 3.7.

to a change in temperature. The frequency ratio should not be affected by the excitation amplitude, because, for an equal amplitude, both species are affected in the same way. In addition, we varied the excitation amplitude for a single species (Dy) and we did not observe any significant shift for the amplitude used here. The estimated gravitational frequency shift in our trap is $\sim 0.1\%$ ³, which we neglect in our analysis. Moreover, we noticed that the fitted frequency may slightly depend (on the subpercent level) on the time interval chosen for the analysis. To avoid systematic deviations in the comparison of both species, we choose the time intervals to follow the scaling factor of 3.6. With 0-2.2 ms for K and 0-8 ms for Dy, the intervals then correspond to about twice the respective $1/e$ damping time τ_K or τ_{Dy} .

3.5 Determination of the Polarizability

We now turn our attention to an accurate and precise determination of the frequency ratio ω_K/ω_{Dy} . We measure the potassium and dysprosium CoM oscillation frequency, in the same trap, in an alternating fashion to eliminate possible slow drifts over time, and repeat this 10 times. The resulting frequency ratios, including small anharmonicity corrections, are shown in Fig. 3.4. The data were taken on two different days, which were

³The relative frequency downshift caused by the gravitational sag can be approximated by: $-2(g/w_0\omega^2)^2$

one week apart, and the consistency shows the robustness of the presented method. The differential anharmonicity effect from Eq. (3.5) yields a small correction of about 1.4% and 2.2% for the frequency ratio of the two data sets. The combined result for the frequency ratio is $\omega_K/\omega_{\text{Dy}} = 3.632(22)$; for details on the error budget see 3.7.

In a second set of experiments, we measure the frequency ratio $\omega_{\parallel}/\omega_{\perp}$ for Dy in a magnetic field parallel and perpendicular to the polarization of the laser field. In this way, we can identify the tensor part which is expected to be more than 100 times smaller [110] than the scalar part. Here we perform in total 11 pairs of measurements 3.7, alternating the angle θ between 0 and $\pi/2$. We obtain the combined result $\omega_{\parallel}/\omega_{\perp} = 1.0070(24)$, which significantly deviates from one and thus reveals a tensor contribution.

From the measured frequency ratios and Eqs. (3.1-3.3), it is now straightforward to derive the polarizability ratios $(\tilde{\alpha}_S + \tilde{\alpha}_T)/\tilde{\alpha}_K = 3.217(40)$ and $(\tilde{\alpha}_S + \tilde{\alpha}_T)/(\tilde{\alpha}_S - \tilde{\alpha}_T/2) = 1.014(5)$. Solving for the scalar and tensor part and using the reference value for $\tilde{\alpha}_K$, we finally obtain $\tilde{\alpha}_S = 184.4(2.4)$ and $\tilde{\alpha}_T = 1.7(6)$.

Our result for the scalar polarizability lies between the two theoretical values of 180 a.u. [107] and 193 a.u. [110], being consistent with both of them within the corresponding error estimates of a few percent [125, 126]. For the small tensorial part, our result is consistent with the theoretical value of 1.34 a.u. [110].

3.6 Discussion and Conclusion

Already in its present implementation, the experimental uncertainty of our method to determine the DP of a magnetic lanthanide atom is smaller than the uncertainties of theoretical calculations. This, in turn, means that our new result already provides a benchmark and sensitive input for refined theoretical calculations. In extension of our work, much more information on the DP can be obtained by measuring at other optical wavelengths [115], which is straightforward to be implemented experimentally. Furthermore, experimental uncertainties may be reduced considerably by using the well-defined environment of optical lattices instead of macroscopic trapping schemes. Further advanced DP measurements could provide a wealth of accurate information on the interaction of light with atoms that feature a complex electronic structure, which would go far beyond the present state of the art.

The presented technique should also be largely applicable to the rapidly

expanding field of ultracold molecules [127, 128], where diatomic molecules combining alkali and alkaline earth atoms are produced routinely in numerous labs. The increased complexity of the molecular structure, relative to its atomic constituents, renders the precise determination of the dynamic polarizability challenging. Another emerging field aims at direct laser cooling and trapping of more exotic molecules [129, 130], with the benefit of a larger ground state electric dipole moment or applicability to precision measurements. In such systems sympathetic cooling by ultracold alkali atoms [131, 132] or even by ultracold hydrogen has been proposed [133] as a route to reach quantum degeneracy. In all of the above experiments a spectroscopically well understood species exists either as a constituent forming the molecule or as a coolant, naturally enabling reference measurements of polarizability and other physical quantities.

In our future experiments, we are particularly interested in mass-imbalanced Fermi-Fermi mixtures and possible new superfluid pairing regimes [33, 134–140]. For the combination of ^{161}Dy and ^{40}K and not far from our present experimental conditions, a “magic” wavelength is expected to exist where the polarizability ratio for the two species corresponds to the inverse mass ratio. An optical dipole trap operating at this particular wavelength would automatically match the Fermi surfaces of both species after deep evaporative cooling. Based on Refs. [107] and [110] for Dy and [120] for K, we would expect this wavelength to be at 982 nm or 954 nm, respectively, and our present measurement suggests it to be in between these two values. The precise location will be subject of further studies.

3.7 Supplemental material

In Sections 3.7.1 and 3.7.2 we present measurements on Dy testing systematic effects introduced by atomic density and temperature. Section 3.7.3 provides additional information on our measurement of the tensor part of the polarizability of Dy. Section 3.7.4 reviews the different contributions to the uncertainty on our measurement of the polarizability of Dy.

3.7.1 Absence of Density Effect on Oscillation Frequency

Throughout our determination of the polarizability of Dy we assume that the frequency of the CoM oscillations is independent of the atomic density, as is expected in a harmonic potential. In this section we test this basic assumption by investigating the effect of density on our frequency measurements. We prepare samples of largely different atom number and determine the frequency for the same trap depth as used in the main text. The atom number is controlled through the MOT loading time. We use a standard (reduced) loading time of 4 s (0.2 s), resulting in a cloud of about 1.1×10^6 (4.5×10^5)

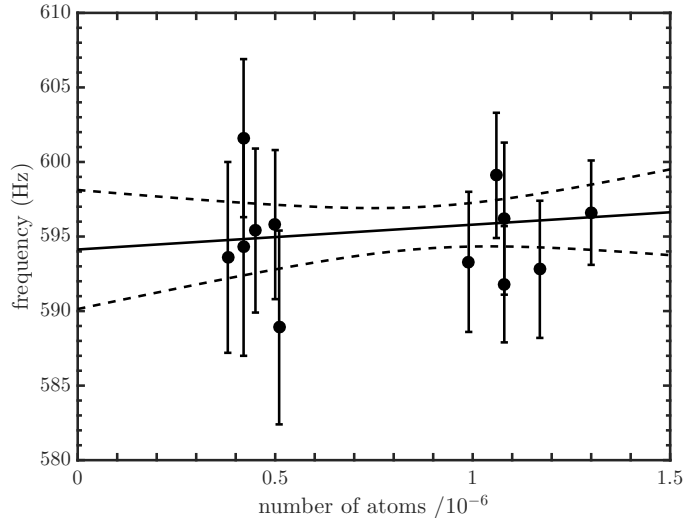


Figure 3.5: Test of the effect of atomic density on the oscillation frequency. The measured frequency is plotted against the atom number. The solid line is a linear fit, and the dashed line shows the 68% (1σ) confidence band.

atoms. We measure alternately using one loading time, then the other one, and repeat the procedure to eliminate the effect of possible slow drifts. After each individual measurement the temperature of the cloud is measured by ToF expansion. Based on these temperatures, the measured trap frequencies are corrected to account for the effect of anharmonicity of the trap, using the coefficient β defined in the main text. Note, however, that we do not observe a significant correlation between temperature and atom number. The results are presented in Figure 3.5. A linear fit gives a slope of 0.28(70)% per million of atoms, which is consistent with the absence of a density effect. This confirms our assumption of a density independence of the oscillation frequency on the level of 1% for our standard experimental conditions.

3.7.2 Damping of Oscillations

In the main text we introduce the assumption that the damping of the CoM oscillations originates essentially from the anharmonicity of the trap: Different classes of atoms explore different regions of the trap as they oscillate, hence experiencing slightly different trap frequencies and eventually dephasing. Such a behavior would mean that the CoM oscillations that we observe result from a superposition of pure single-particle oscillations. This assumption is supported by the equal damping behavior of the two species, as pointed out in the main text, and by an estimation based on our experi-

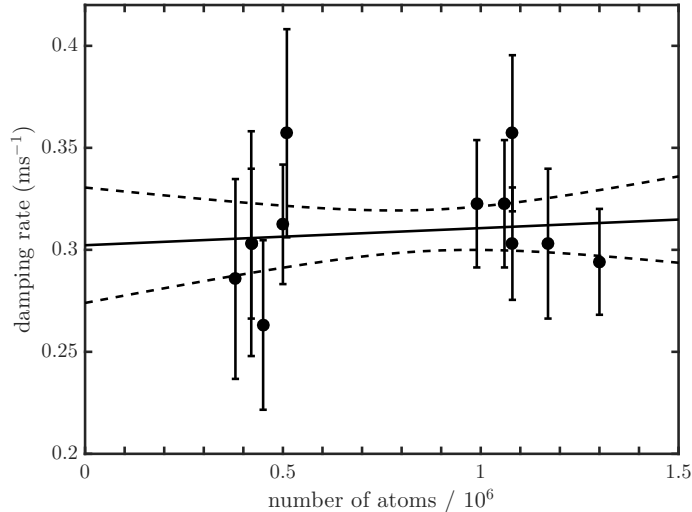


Figure 3.6: Density independence of the damping rate. The solid line is a linear fit, and the dashed lines show the 68% (1σ) confidence band.

mental settings of the collision rate of dysprosium atoms, which yields 80 s^{-1} (a similar calculation for potassium gives a collision rate of about 90 s^{-1}). Given the radial trap frequency of about 600 Hz (2 kHz for K), the radial motion in our trapped samples is far away from the hydrodynamic regime. Here we further test our assumption on the origin of the observed damping by considering the density and temperature dependence of the damping rate of the CoM oscillations.

From the analysis of the set of experiments presented in Sec. A we also obtain the damping rate of the oscillations. Its behavior as a function of atom number is plotted in Figure 3.6. A linear fit gives a slope of $+0.008(30) \text{ s}^{-1}$ per million atom and thus does not show any significant density dependence on the 10% level for our standard atom number. This observation support our assumption of damping being essentially due to dephasing effects.

We now turn our attention to the study of the dependence of the damping rate on the temperature. From straightforward arguments, one expects the damping rate to be proportional to the temperature. Indeed, for small oscillation amplitudes, the anharmonic frequency shift of a particle in a Gaussian potential scales linearly with its energy, such that the width in Fourier space of the CoM oscillation increases linearly with the temperature of the cloud, finally leading to a linear dependence of the damping rate on the temperature. In the main text, we present a measurement of the dependence of the frequency on the temperature of the cloud (see Figure 3 in the main

text). The analysis of the corresponding oscillation data also allows us to investigate the dependence of the damping rate of the oscillations on the temperature. The results are shown in Figure 3.7. We observe an increase of the damping with temperature. A linear fit without offset gives a slope of $0.409(15) \text{ ms}^{-1} \mu\text{K}^{-1}$, and a reduced χ^2 of 0.96, showing that our simple model fits well to the data. This behavior also supports our interpretation on dephasing being the main source of damping.

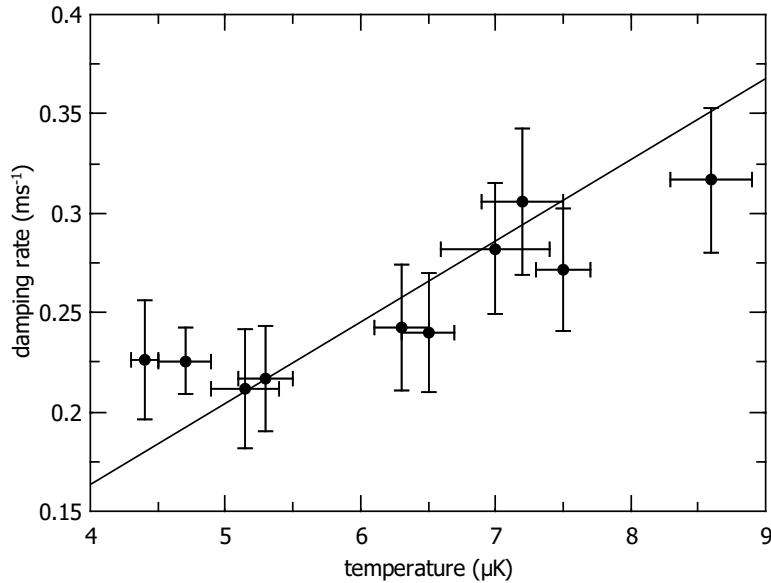


Figure 3.7: Temperature dependence of the damping time. The solid line is a linear fit without offset, with weights taking both horizontal and vertical error bars into account.

3.7.3 Error Budget of the Frequency Ratio Measurement

We measure the trap frequency ratio in two sets of data obtained on two different days. Each set of data is corrected for the residual anharmonicity, based on the anharmonicity coefficient β and on the measured temperatures of the two species. A part of the uncertainty originates from the statistical distribution of the measured frequency ratios $\omega_{\text{K}}/\omega_{\text{Dy}}$. The rest of the uncertainty originates from the error in the anharmonicity correction and has five contributions: the error on the anharmonicity coefficient β , and the error on the measured temperatures of the K and Dy clouds. The respective contributions to the absolute uncertainty on $\omega_{\text{K}}/\omega_{\text{Dy}}$ are listed in Table 3.1.

The total absolute uncertainty that results from the anharmonicity correction is 0.019, and the statistical uncertainty from the 10 combined individual

Table 3.1: Error budget for the measurement of ω_K/ω_{Dy} .

parameter	value	uncertainty in parameter	uncertainty in frequency ratio
T_{Dy} set 1	8.3 μK	0.2 μK	0.003
T_K set 1	7.6 μK	0.3 μK	0.004
T_{Dy} set 2	35.7 μK	3.2 μK	0.015
T_K set 2	30.3 μK	2.0 μK	0.008
β	-4.50 Hz/ μK	0.43 Hz/ μK	0.006

measurements is 0.012. These two errors are quadratically combined, which finally yields the quoted uncertainty of 0.022.

3.7.4 Measurement of the Tensor Contribution

We measure oscillation frequencies for two different orientations of the magnetic field: Always being perpendicular to the propagation axis of the trapping laser, the field is either aligned with the polarization axis of the trapping laser, or perpendicular to it. All other parameters are kept identical. The strength of the field is in both cases 250 mG. In the latter case we take care that the spin state of the atoms adiabatically follows the rotation of the magnetic field. We measure alternately the trap frequency for one orientation of the field, then for the other one, and repeat the procedure to eliminate systematic effects from possible slow drifts. We measure in total 11 pairs of trap frequencies over two different days, which gives us 11 values for the frequency ratio, as shown in Figure 3.8. A weighted average yields $(a_s + a_t)/(a_s - a_t/2) = 1.0140(48)$.

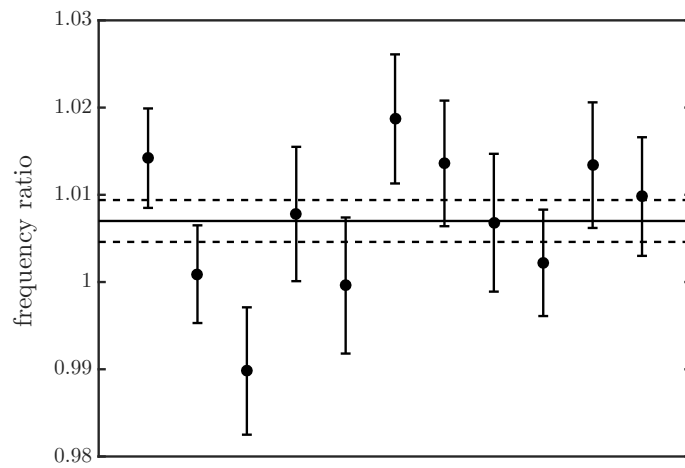


Figure 3.8: Repeated measurements of the frequency ratio $\omega_{\parallel}/\omega_{\perp}$. The first five points have been measured on one day, the remaining six ones on a second day. The solid line shows the weighted average $\omega_{\parallel}/\omega_{\perp} = 1.0070(20)$ with the dashed lines showing the corresponding statistical error range.

Chapter 4

Publication: Production of a degenerate Fermi-Fermi mixture of dysprosium and potassium atoms

Published as:

Cornelis Ravensbergen, Vincent Corre, Elisa Soave, Marian Kreyer, Emil Kirilov, and Rudolf Grimm
[Phys. Rev. A **98**, 063624 \(2018\)](#)

Author contribution: The author took a leading role in the process of acquiring and analyzing the data described in this publication as well as contributed to the writing of the manuscript.

Changes with respect to the original publication: Due to a calibration error the published atom numbers had to be reduced by a factor of 2.27. In this chapter the stated atom number, Fermi temperature, density, phase-space density and scattering length have been adjusted accordingly. Subsequently, all figures have been corrected.

We report on the realization of a mixture of fermionic ^{161}Dy and fermionic ^{40}K where both species are deep in the quantum-degenerate regime. Both components are spin-polarized in their absolute ground states, and the low temperatures are achieved by means of evaporative cooling of the dipolar dysprosium atoms together with sympathetic cooling of the potassium atoms. We describe the trapping and cooling methods, in particular the final evaporation stage, which leads to Fermi degeneracy of both species. Analyzing cross-species thermalization we obtain an estimate of the magnitude of the inter-species s -wave scattering length at low magnetic field. We demonstrate magnetic levitation of the mixture as a tool to ensure spatial overlap of the two components. The properties of the Dy-K mixture make it a very promising candidate to explore the physics of strongly interacting mass-imbalanced Fermi-Fermi mixtures.

4.1 Introduction

Strongly interacting systems composed of imbalanced fermions offer an increased complexity as compared to the balanced case by adding effective exchange interaction and dissimilar dispersion of the constituents. The physics emanating from new pairing mechanisms is rather enriched compared to the standard population and mass-balanced case, described by the established Bardeen-Cooper-Schrieffer (BCS) attractive interaction [141]. Appearing in various fields, such systems have been predicted to generate exotic pairing such as breached and inhomogeneous pairing, the last exhibiting a spatially varying order parameter [29]. In nuclear physics the possibility for neutron-proton correlations and Cooper pair condensation has been investigated in several contexts ranging from heavy-ion collisions to astrophysical processes [142]. Inhomogeneous superconductivity has been argued to exist for asymmetric nuclear matter in supernovae and neutron stars [143]. In quantum chromodynamics, a phenomena coined color inhomogeneous superconductivity is expected to take place [144–148]. Because of its ubiquity, such states of matter are also discussed and searched for in condensed matter physics, where experimentally favorable systems include heavy-fermion, organic, or high- T_c superconductors [144].

In the context of ultracold two-component Fermi gases, some exotic phases like the paradigmatic Fulde-Ferrell-Larkin-Ovchinnikov (FFLO) [65, 149, 150], Sarma [151] as well as interior [134] and exterior gap breached-pair phases [152], have been theorized. Specifically, the FFLO phase seems to be experimentally achievable in mass-imbalanced systems at unitarity, because of the higher superfluid transition temperature [32, 33, 139, 153] relative

to the equal-mass case. In general the mass-imbalanced strongly interacting fermionic mixtures based on cold atoms, as a result of the generated Fermi surfaces and single-particle dispersion mismatch, exhibit a rich phase diagram, which includes a Lifshitz point and population-dependent asymmetry [137, 154–156]. Such systems can be also employed to study itinerant ferromagnetism [157], a phenomenon where microscopic understanding is still evolving [158]. As a further example, a crystalline phase of weakly bound molecules consisting of heavy and light fermions has been predicted [159], countering the intuitive expectation of a gas phase.

Fermionic mixtures of ultracold atoms are also well suited to tackle impurity physics and the polaron problem [157]. One open aspect is an impurity coupled to a non-equilibrium Fermi gas, where multicomponent cold gases are well suited to explore the non-equilibrium Anderson catastrophe and the influence of the environment on the impurity dynamics [160, 161]. Fermionic mixtures made out of different atomic species additionally allow for the use of a species-selective optical lattices [96]. This handle opens the possibility in multicomponent systems for the realization of Kondo-related physics in transport measurements [162]. It should also be emphasized that two-component Fermi gases also offer a variety of interesting few-body effects such as atom-dimer resonant scattering [84, 163] and confinement-induced Efimov resonances in systems with mixed dimensionality [164].

Up to now, the ^{40}K - ^6Li mixture has represented the only tunable mixture of fermionic species realized in the laboratory [71, 73, 165, 166]. The mass ratio makes this combination in principle attractive for pursuing many of the above goals. In this system, effects of strong interactions near Feshbach resonances (FR) have been observed in hydrodynamic expansion [83], in impurity physics [85, 167, 168], and in three-body interactions [84]. However, at resonant interspecies interaction, this mixture suffers from lifetime limitations owing to the narrow character of the FR [77, 169]. The width of the FR, together with Pauli suppression of few-body collisions [89, 170–174], is a prerequisite for achieving long lifetimes in strongly interacting fermionic atomic mixtures and weakly bound dimers made of fermionic atoms. This enhanced stability against inelastic decay has been observed in numerous experiments of both single-species [51, 80, 81, 175, 176] and recently also in dual-species experiments [78]. This facilitated the realization and exploration of numerous research avenues, including molecular Bose-Einstein condensation, BEC-BCS crossover physics, the unitary Fermi gas, and superfluid pairing [177–179].

Here, we introduce a different mass-imbalanced Fermi-Fermi mixture, namely,

the dysprosium-potassium (Dy-K) mixture ¹. For creating a Fermi-Fermi mixture, a number of combinations could be selected from the variety of chemical elements that have been brought to Fermi degeneracy [37–45, 47]. The important criteria to adhere to are as follows: (i) mass ratio well below 13.6 to suppress Efimov-related losses [174], (ii) tunable interactions, and (iii) collisional stability [78]. Complying with these criteria narrows down the possible combinations to ¹⁶¹Dy-⁴⁰K, ¹⁶³Dy-⁴⁰K, ¹⁶⁷Er-⁴⁰K, and ⁵³Cr-⁶Li. We have chosen specifically the Dy-K combination, anticipating a favorable scattering spectrum, which is on one hand not chaotic, but it is conveniently dense, extrapolating from [181]. We note that, combinations utilizing a closed-shell fermion (¹⁷¹Yb, ¹⁷³Yb, or ⁸⁷Sr) in its electronic ground state with an alkali-metal atom offer only extremely narrow resonances [86, 87], and therefore are not suited for our purpose.

In this article, we present the preparation and cooling of a Fermi-Fermi mixture of ¹⁶¹Dy and ⁴⁰K atoms, reaching deep quantum degeneracy for both species. In Sec. 4.2, we first summarize the laser cooling procedures that provide the starting conditions for subsequent evaporation. In Sec. 4.3, we then report our main results. We first demonstrate deep cooling of spin-polarized ¹⁶¹Dy based on universal dipolar scattering. Then we investigate cooling of a mixture of ¹⁶¹Dy with ⁴⁰K, where the K component is cooled sympathetically by thermal contact with Dy. We also demonstrate the effect of magnetic levitation as an interesting tool for future experiments, and we present a first measurement of the interspecies scattering cross section. In Sec. 4.4, we finally give a brief outlook on future steps to realize a strongly interacting, mass-imbalanced fermionic mixture.

4.2 Laser Cooling and Dipole Trap Loading

In this section, we summarize the laser-cooling steps in our experimental sequence, which prepare the starting point for subsequent evaporative cooling in an optical dipole trap. In Sec. 4.2.1 we describe the loading of dysprosium and potassium atoms into two respective magneto-optical traps (MOTs). In Sec. 4.2.2 we discuss the procedure used to transfer the atoms into a large-volume optical dipole trap, where they coexist in a mixture.

4.2.1 Magneto-Optical Traps

Our dysprosium preparation scheme is similar to the one described in Refs. [105, 122]. As a source of Dy atoms, we use a high-temperature effusion

¹Mixture experiments with magnetic lanthanide atoms represent a new frontier in the research field. The only other experiment reported so far has been carried out on mixtures of Er and Dy and reported quantum-degenerate Bose-Bose and Bose-Fermi mixtures [180]

oven operating at about 1000 °C combined with a Zeeman slower operating on the broad line (natural linewidth of 32 MHz) at 421 nm. Dy atoms are collected in a MOT operating on the narrow ($\Gamma_{626} = 2\pi \times 135$ kHz) intercombination transition at 626 nm. Further details on the apparatus can be found in Appendix 4.5.1. The MOT uses a magnetic field gradient of about 2 G/cm along the strong vertical axis. We use 35-mm-diameter ($1/e^2$ intensity drop) beams, with an intensity of $170 I_{\text{sat},626}$ per beam (where $I_{\text{sat},626} = 72 \mu\text{W cm}^{-2}$ is the saturation intensity of the 626 nm line). The laser is detuned by a few MHz to the red of the transition² and subsequently spectrally broadened by a high-efficiency electro-optical modulator to increase the loading efficiency [122]. Using these parameters we typically load 2.2×10^7 atoms of ^{161}Dy atoms in 3 s. After loading, the MOT is compressed by abruptly switching off the spectral broadening and, within 170 ms, ramping the detuning closer to resonance, the power down to $I \approx 0.5 I_{\text{sat},626}$, and the gradient of magnetic field down to 1.4 G/cm. The atoms are then held in the compressed MOT for 80 ms. During this hold time, the Dy atoms are naturally optically pumped into the stretched state $|F = 21/2, m_F = -21/2\rangle$ [105]. The temperature after the compressed MOT is approximately 8 μK .

The source of K atoms is a two-dimensional MOT in a glass cell, connected to the main chamber via a differential pumping tube, similarly to [166]. In the chamber the atoms are collected in a three-dimensional MOT operating on the D2 line at a wavelength of 767 nm. The K MOT beams combine the cooler and repumper frequencies (the latter being created by a free-space electro-optical modulator). They have an intensity of $I_{\text{cool}} = 6 I_{\text{sat},767}$ and $I_{\text{rep}} = 0.3 I_{\text{sat},767}$, and are detuned by $\delta_{\text{cool}} = -4.4 \Gamma_{767}$ and $\delta_{\text{rep}} = -2.7 \Gamma_{767}$ relative to the $F = 9/2 \rightarrow F' = 11/2$ and $F = 7/2 \rightarrow F' = 9/2$ transitions, respectively. Here $I_{\text{sat},767} = 1.75 \text{ mW cm}^{-2}$ is the saturation intensity of the D2 line of K, and Γ_{767} its natural linewidth. The gradient of magnetic field is set to 9.6 G/cm along the strong axis. We typically load the MOT for 3 s, which gives 0.9×10^6 atoms of ^{40}K . Once loaded, the K MOT is compressed by simultaneously ramping up the gradient of magnetic field to 25 G/cm, ramping down the detunings to $\delta_{\text{cool}} = -1.1 \Gamma_{767}$ and $\delta_{\text{rep}} = 0$ and the powers down to $I_{\text{cool}} = 0.5 I_{\text{sat},767}$ and $I_{\text{rep}} \approx 0.01 I_{\text{sat},767}$, all in 4 ms. At the end of the compressed MOT phase the temperature of the K cloud is 110(30) μK . We then perform gray molasses cooling on the D1 line, which allows us to lower this temperature to approximately 30 μK . Details on the gray molasses stage are given in Appendix 4.5.3.

²We define detunings as $\delta = \omega_{\text{laser}} - \omega_{\text{atom}}$, such that a red (blue) detuned laser corresponds to a negative (positive) detuning

4.2.2 Sequential Dipole Trap Loading

The transfer of atoms from a MOT or a molasses into an optical dipole trap is a common procedure in cold-atom experiments. The optimum transfer strategy depends on the particular properties of the atomic species and on the cooling scheme applied prior to the dipole trap loading. In many dual-species experiment, however, the optimum loading conditions for both components are incompatible with each other, such that a sequential loading scheme is necessary. In the case of Dy and K atoms, the main constraint is imposed by the vastly different gradient of the magnetic field required in the respective MOTs. Indeed, the larger gradient used to load K atoms would induce a strong compression of the Dy cloud, which in turn would lead to large losses. We therefore sequentially load the K atoms and then the Dy atoms into a reservoir optical dipole trap (RDT).

The RDT is created by two intersecting beams derived from a single, longitudinally multimode, fiber laser (IPG YLR-100-LP, wavelength 1070 nm) and crossing in the horizontal plane under an angle of 18° ; see Fig. 4.1. The RDT is already switched on during the K-MOT stage, with a power per beam of 11.5 W, corresponding to a depth $U_{\text{RDT}}^{\text{K}}/k_{\text{B}} = 260 \mu\text{K}$. After compression of the K MOT (Sec. 4.2.1), the atoms are transferred into the RDT, while being cooled by the gray molasses (App. 4.5.3). We typically load 2.2×10^5 ^{40}K atoms, corresponding to a transfer efficiency of 20%, at a temperature of $33(1) \mu\text{K}$ ³.

After the gray molasses, a 0.8 ms laser pulse is applied to optically pump the atoms in the $|F = 9/2, m_F = -9/2\rangle$ state. The pulse has σ^- polarization with a small admixture of π polarization, and has frequency components resonant with the D1 transitions $F = 7/2 \rightarrow F' = 9/2$ and $F = 9/2 \rightarrow F' = 7/2$, such that the $|F = 9/2, m_F = -9/2\rangle$ state is a dark state. During the pulse, the gradient of magnetic field is turned off and a homogeneous field of approximately 1 G is applied along the direction of the beam. The optical pumping only has a minor effect on the temperature of the cloud: We measure an increase of the temperature on the order of $1 \mu\text{K}$. To check the polarization of the K sample we perform resonant absorption imaging at high magnetic field (155 G), where the splittings between the different $|F, m_F\rangle \rightarrow |F', m_{F'} = m_F + 1\rangle$ transitions are large compared with the natural linewidth. After the pulse we still observe approximately 10% of atoms left in $|9/2, -7/2\rangle$.

We then load the Dy MOT for 3 s, while holding the K atoms in the RDT. As we start loading Dy, the power of the RDT is increased, resulting in

³In the absence of dipole trap, the D1 cooling allows us to reach temperatures as low as $8(1) \mu\text{K}$

a depth $U_{\text{RDT}}^{\text{Dy}}/k_{\text{B}} \approx 110 \mu\text{K}$ for Dy and $U_{\text{RDT}}^{\text{K}}/k_{\text{B}} \approx 360 \mu\text{K}$ for K [182]. This compression increases the temperature of K to $37(2) \mu\text{K}$. Since the Dy MOT forms below the zero of the quadrupole magnetic field, it is spatially separated from the K cloud and does not affect the lifetime of the K atoms in the dipole trap, which is measured to be 4 s. Finally, the compression of the Dy MOT (Sec. 4.2.1) moves it upward, such that it overlaps with the RDT, where Dy atoms are transferred. At this stage the central region of the RDT typically contains 5×10^6 Dy atoms at a temperature of $17(1) \mu\text{K}$, corresponding to a loading efficiency of 10%, and approximately 0.9×10^5 K atoms at a temperature of $28(2) \mu\text{K}$. The fact that the temperature of the K sample decreases during the 3 s hold in the RDT is also observed in the absence of Dy and is presumably an effect of plain evaporation allowed by the remaining spin polarization imperfection. We do not observe interspecies thermalization on the considered time scale at this point.

At the end of the Dy MOT stage, all resonant light is switched off and the gradient of magnetic field is set to zero. A homogeneous magnetic field of approximately 430 mG is applied along the vertical direction to define a quantization axis and to maintain the polarization of the two clouds. At this point, we do not observe any population in higher spin states of K and Dy, which we attribute to rapid intraspecies and interspecies dipolar relaxation. The conditions after the loading of both species in the RDT are summarized in Table 4.1.

4.3 Evaporative Cooling

In this Section, we present our main results on evaporative cooling down to deep degeneracy of both fermionic species. We evaporatively cool fully spin-polarized Dy [45, 48] (see also related work on fermionic Er [47, 183]), relying solely on universal dipolar scattering [36]. The K component, for which the optical trap is much deeper, is cooled sympathetically. This cooling scheme is closely related to earlier experiments on the attainment of quantum degeneracy in Yb-Li mixtures [74, 184, 185], where the heavy lanthanide species experiences a shallower trapping potential than the light alkali-metal species. As in our work, evaporative cooling acts on the heavier species, which then cools the lighter one in a sympathetic way. The main difference to our work is the origin of elastic collisions among the heavier atoms, which in the Yb cooling scenarios result from *s*-wave collisions between identical bosons or non-identical fermions, and not from universal dipolar scattering between identical fermions.

We employ a sequence of two optical dipole traps. A first evaporative cooling step is performed in the RDT. Atoms are then transferred into the main

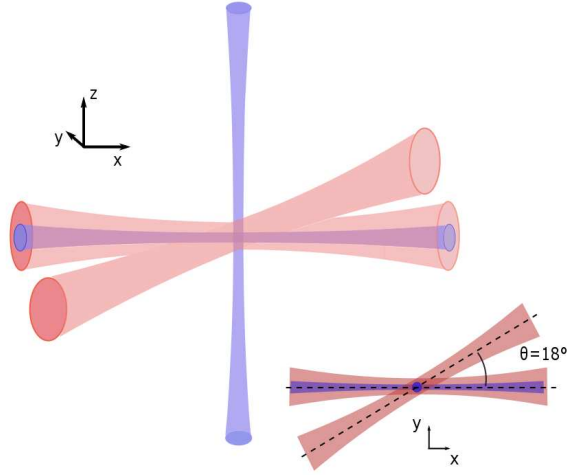


Figure 4.1: Optical dipole traps scheme. The two beams of the large volume RDT propagate in the horizontal x - y plane and intersect under an angle of 18° , while the two orthogonal beams of the CDT propagate in the x - z plane. The lower right scheme shows a view from the top.

dipole trap, where evaporative cooling continues. In Secs. 4.3.2 and 4.3.3, we characterize the evaporation process in two situations: We first describe the evaporation of ^{161}Dy atoms alone, and then the evaporation of the mixture. In Sec. 4.3.4 we discuss the effect of gravity and its compensation by a levitation field. Finally, in Sec. 4.3.5 we show the results of an interspecies thermalization measurement, from which we give an estimate of the interspecies s -wave scattering cross section, a quantity of primary importance in the efficiency of the simultaneous cooling of the two species.

4.3.1 Transfer from Reservoir into Main Dipole Trap

With the phase-space density reaching values in the 10^{-4} range for each species, the RDT provides favorable starting conditions for evaporative cooling. However, the large waist of the beams forming the RDT does not allow us to maintain a large enough collision rate in this trap when its power is lowered. Aside from this, as a technical issue, the RDT is created by a longitudinally multimode laser, where evaporation of Dy is known to be hindered by heating processes [113, 186]. We therefore perform a two-step evaporation: After a first evaporation ramp taking place in the RDT, the atoms are transferred into a tighter crossed dipole trap (CDT), where the evaporative cooling continues.

Table 4.1: Cloud parameters after transfer into the RDT. The given parameters describe the cloud in the RDT immediately after the Dy MOT is turned off. U_{RDT} refers to the depth of the optical potential, n_{peak} to the peak density in the center of the trap, PSD to the phase-space density. The errors in n_{peak} and in the PSD result from the propagation of the errors in N and T , whereas the systematic errors in U_{RDT} and in $\bar{\omega}$ are not propagated.

	^{161}Dy	^{40}K
$\bar{\omega}/2\pi$	154(6) Hz	558(22) Hz
$U_{\text{RDT}}/k_{\text{B}}$	110(8) μK	360(20) μK
N	$5.3(4) \times 10^6$	$8.8(9) \times 10^4$
T	17(1) μK	28(2) μK
n_{peak}	$1.0(1) \times 10^{13} \text{ cm}^{-3}$	$5.3(9) \times 10^{11} \text{ cm}^{-3}$
PSD	$3.5(9) \times 10^{-4}$	$0.7(2) \times 10^{-4}$

The CDT is created by a longitudinally single-mode Nd:YAG laser (Mephisto MOPA 18 NE) at 1064 nm. The configuration of dipole traps is depicted in Fig. 4.1. One beam of the CDT overlaps in the horizontal plane with one beam of the RDT and has a waist of approximately 30 μm , while the second beam propagates along the vertical axis and has a waist around 60 μm .

During the first 20 ms after completion of the RDT loading, the power of the RDT is kept fixed while the powers in the horizontal and vertical beams of the CDT are ramped up from 0 to 1.6 and 0.7 W, respectively. This results in a depth of approximately 54 μK for Dy, and of 174 μK for K. From that point, as illustrated in Fig. 4.2, the power of the RDT is reduced in an exponential ramp to 1.6 W per beam in 100 ms, while the power in the horizontal beam of the CDT is ramped up to 3.5 W. The power in the vertical beam is kept constant during this time. At the end of these ramps, the RDT is turned off. At its full power, the CDT has a depth $U_{\text{CDT}}^{\text{Dy}}/k_{\text{B}} = 130 \mu\text{K}$ and the trap frequencies are $[\omega_x, \omega_y, \omega_z] = 2\pi \times [88, 1040, 1037]$ Hz for Dy. Typically, 0.9×10^6 Dy atoms and 2.9×10^4 K atoms are loaded into the CDT, with a temperature of 24(1) μK for Dy and 28(1) μK for K. The phase-space density after the transfer is on the order of 10^{-3} for both Dy and K. The cloud parameters immediately after transfer into the CDT, i.e., the starting conditions for the subsequent evaporative cooling, are summarized in Table 4.2.

4.3.2 Evaporative Cooling of a Pure ^{161}Dy Cloud

We now turn to the second phase of the evaporation, which is carried out in the CDT. We first consider the efficiency of the evaporative cooling of pure ^{161}Dy , i.e. in the absence of K atoms. As soon as the RDT is switched off, the evaporation ramp is started. The magnetic field is kept at 430 mG, thus

Table 4.2: Starting conditions for the evaporation in the CDT. N_{center} gives the number of atoms in the central region of the trap, while N_{arms} corresponds to the atom number trapped outside the region where the two beams cross, in the arms of the potential. U_{CDT} refers to the depth of the optical potential created by the CDT, n_{peak} to the peak density and PSD stands for phase-space density. As in Table 4.1, the errors in n_{peak} and in the PSD are obtained from the errors in N in T only.

	^{161}Dy	^{40}K
$\bar{\omega}/2\pi$	456(18) Hz	1460(60) Hz
$U_{\text{CDT}}/k_{\text{B}}$	130(5) μK	419(17) μK
$N_{\text{center}}; N_{\text{arms}}$	$7.9(4) \times 10^5; 1.3(1) \times 10^6$	$2.8(2) \times 10^4; \sim 5 \times 10^4$
T	24(1) μK	28(1) μK
n_{peak}	$2.7(2) \times 10^{13} \text{ cm}^{-3}$	$4.4(4) \times 10^{12} \text{ cm}^{-3}$
PSD	$6.2(9) \times 10^{-4}$	$6.6(9) \times 10^{-4}$

avoiding crossing any major Feshbach resonance [187]. The evolution of the power in the two dipole traps is depicted in Fig. 4.2 and is optimized in terms of the final temperature ratio T/T_F achieved, where $k_{\text{B}}T_F = \hbar\bar{\omega} (6N)^{1/3}$ is the Fermi temperature (in the following, we use the atom number in the central region of the CDT to calculate T_F). We adopt a standard evaporation scheme in which the power in the horizontal beam of the dipole trap is decreased while the power in the vertical one is increased [100, 101, 188, 189]. The power in the horizontal beam of the CDT is lowered in an exponential ramp to 150 mW within 15 s, while the power in the vertical beam is first increased linearly to 1.17 W within 10 s and then to 1.75 W within 5 s.

Figure 4.3 shows a time-of-flight image of the degenerate cloud obtained at the end of the evaporation ramp (a brief description of our imaging scheme is presented in Appendix 4.5.2). The two panels on the right show cuts along two orthogonal axes through the two-dimensional (2D) density profile. The solid red lines result from a fit of the density profile by a polylogarithmic function. We obtain 3.5×10^4 atoms at a temperature of 60(10) nK, corresponding to $T/T_F = 0.11(1)$. The trap depth at this point is $U = k_{\text{B}} \times 720$ nK and the trap frequencies are $[\omega_x, \omega_y, \omega_z] = 2\pi \times [133, 248, 176]$ Hz, both calculated including the effect of gravity. The peak number density is $0.7 \times 10^{14} \text{ cm}^{-3}$.

In Fig. 4.4 we show the evolution of the atom number in the central region of the trap, of the temperature T , and of the ratio T/T_F during the evaporation in the CDT. After approximately 10 s, we observe a change of slope in the evolution of the atom number in the central region [see Fig. 4.4(a)]. We attribute this effect to the presence of atoms in the arms of the trapping

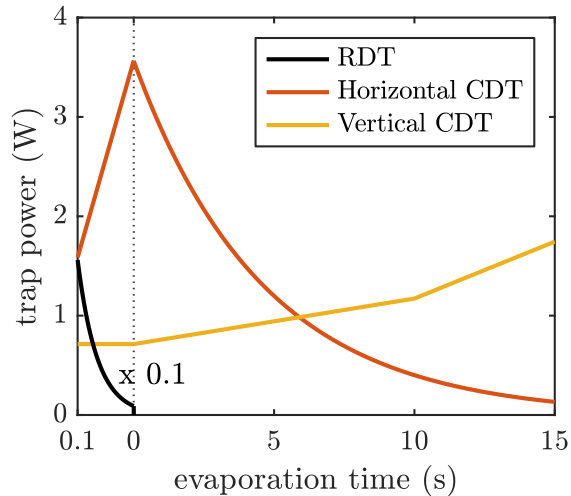


Figure 4.2: Evaporative cooling sequence. Power in the RDT (black) and in the horizontal (red or dark gray) and vertical (orange or light gray) beam of the CDT. The origin of time ($t = 0$) corresponds to the start of the evaporation in the CDT. The power in the RDT and in the horizontal beam of the CDT is decreased in exponential ramps. The sequence is identical for the pure Dy cloud and for the Dy-K mixture.

potential. At $t = 0$, around 1.3×10^6 trapped Dy atoms are present in the horizontal arms. In the first 10 s, these atoms are then preferentially evaporated, cooling also the cloud in the central region. After 10 s, the arms of the trap are found to be empty and, from that point on, the evaporation takes place in the central region of the potential only. The initial fast gain in phase-space density [$\text{PSD} \propto (T/T_F)^{-3}$] associated with the slow decrease of the atom number in the central region suggests that the atoms in the arms play an important role in the efficiency of the forced evaporative cooling.

The temperatures shown in Fig. 4.4(b) are extracted from the observed column density profiles by Gaussian fits or by polylogarithmic fits. The first ones are applied at higher temperatures, the second ones at lower temperature. The fit by a polylogarithmic profile provides two parameters: the size σ , related to the temperature T , and the fugacity ζ . The Fermi temperature is obtained from the measured atom number and the calculated averaged trap frequency. The fugacity on the other side gives direct access to $T/T_F = [-6\text{Li}(-\zeta)]^{-1/3}$. The ratio T/T_F shown in Fig. 4.4(c) is obtained from the measured T and the calculated T_F . A comparison with the second method using the fugacity is presented in the inset for the lowest temperatures achieved, and shows good agreement between the two methods. The

change between the Gaussian and polylogarithmic fit models happens for $T/T_F \approx 1$. The ratio T/T_F levels off after 14 s of evaporation. At this point, the trap depth is on the order of the Fermi energy $E_F = k_B T_F$ and we enter the spilling regime, where efficient evaporation stops.

In Fig. 4.4(b) we compare the measured temperature T with the calculated trap depth U (where the effect of gravity is taken into account). We find that the forced evaporation is well characterized by a truncation parameter $\eta = U/k_B T \approx 7$ throughout the whole evaporation process.

The trapping potential created by the CDT is deformed by gravity. In particular, the trap depth is reduced and, in the very final stage of the evaporation, the trap frequency along the vertical axis is lowered. In our scheme, after 14 s of evaporation, the depth of the CDT is reduced from $5.3 \mu\text{K}$ (depth without gravity) to 720 nK , and the trap frequency along the vertical axis is reduced from 210 to 176 Hz. The reduction of the trap depth is actually beneficial for the evaporative cooling, as pointed out with cesium atoms in [190]. Indeed, the reduction achieved by decreasing the laser power is inherently accompanied by a lowering of the trapping frequencies, which in turn implies a lower collision rate and a less efficient evaporative cooling. Gravity reduces the trap depth essentially without affecting the confinement strength of the trap (the lowering of the trap frequencies only appears at very low trap depth), and allows us to maintain a higher collision rate at low trap depths.

We achieved the lowest temperature $T/T_F = 0.085(10)$ after 14 s of evaporation. For longer evaporation times, the decreasing trap depth reaches the Fermi energy and we observe spilling of the dysprosium cloud. As in earlier work on evaporative cooling of fermions (see, e.g., [191]), we find that the optimal cooling is achieved just before the onset of spilling.

4.3.3 Evaporative Cooling of the ^{161}Dy - ^{40}K Mixture

We now characterize the combined cooling of the Fermi-Fermi mixture. Starting with both components loaded into the RDT, the experimental procedure is identical to the one described for Dy alone, as we find that it also provides the best results for the mixture, provided that the K atom number is kept small (typically, MOT loading time shorter than 3 s, resulting in a final atom number of a few 10^3). Indeed, we observe that an increase of the K atom number (achieved by extending the K MOT loading) compromises the cooling of the Dy sample. As before, the strength of the magnetic field is set to 430 mG.

We first describe the process of evaporative cooling. The atom number in

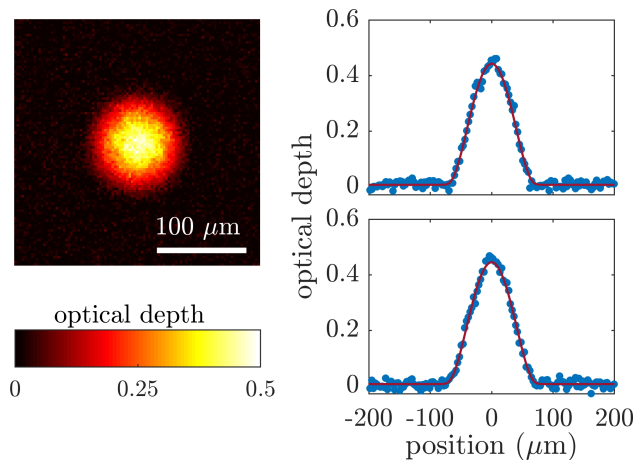


Figure 4.3: Deep evaporative cooling of pure ^{161}Dy . The density profile on the left-hand side is an average of ten absorption images of clouds of approximately 3.5×10^4 ^{161}Dy atoms taken after 14 s of evaporation in the CDT and a subsequent release from the trap (time of flight of 10 ms). The images on the right-hand side show cuts through the two-dimensional optical depth along the x and y axes. The solid lines show the corresponding profiles resulting from a two-dimensional polylogarithmic fit. From the fit we extract $T/T_F = 0.085(10)$.

the central region of the trap and the temperature of the two samples in the CDT are shown in Fig. 4.5. In these measurements, the atoms are held at fixed power during 10 ms before a time-of-flight expansion is performed. The behavior of the number of Dy atoms is essentially the same as observed in the evaporation of pure Dy, with the same change of slope after 10 s of evaporation. The number of K atoms on the other hand decreases very slowly, its final value being approximately half the initial one. Given the deep potential seen by the K atoms, we can exclude evaporation losses, and we therefore attribute the decrease in K atom number to inelastic processes.

The equality of the two temperatures seen in Fig. 4.5(b) demonstrates the efficiency of the sympathetic cooling. However, we observe that the temperature of the K sample decouples after approximately 13 s in the evaporation ramp from the temperature of the Dy component. While the temperature of the Dy follows the evolution of the trap depth, the K temperature decreases much more slowly. As a consequence of this behavior, the ratio $T_K/T_{F,K}$ essentially levels off, at a value close to 0.2. This observed decoupling is not an effect of a spatial separation of the components induced by the gravitational sag [185], as we verified by applying a levitation field that ensures full spatial overlap (see Sec. 4.3.4). This effect may indicate a relatively weak thermal coupling between the two species, which is then further reduced

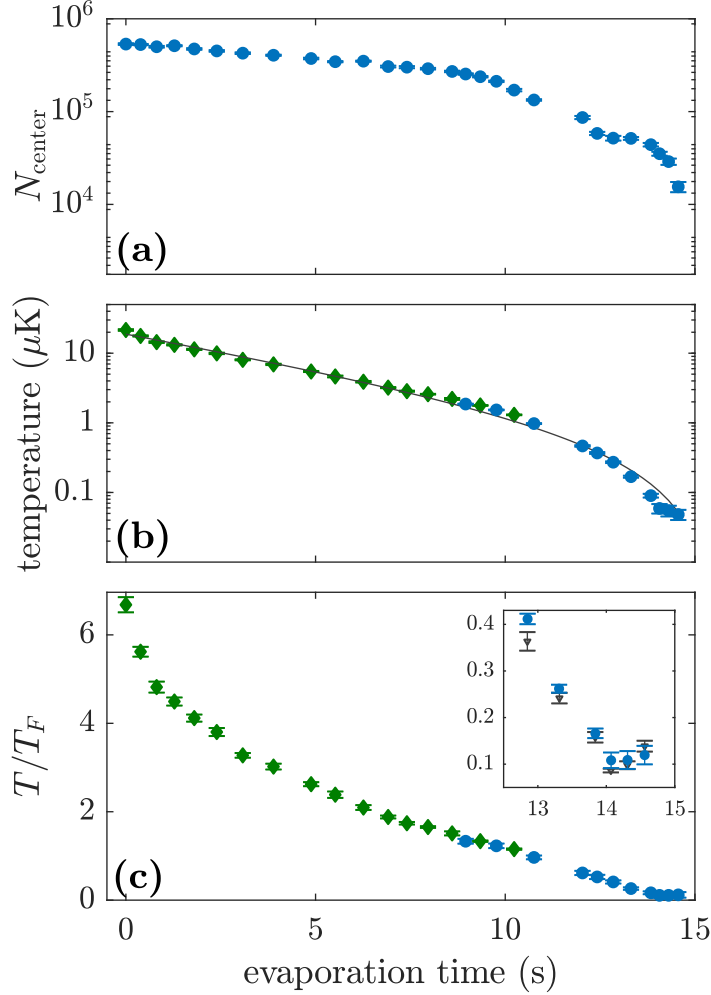


Figure 4.4: Evaporative cooling of ^{161}Dy . Atom number, temperature and temperature ratio T/T_F of the pure dysprosium cloud during the evaporation of the CDT. In (b) and (c), green diamonds show the temperature extracted from a Gaussian fit of the column density, while blue circles are extracted from a polylogarithmic fit. In (b), the solid black line shows the calculated trap depth reduced by a factor of 7. In (c) the inset shows a zoom-in on the final part of the evaporation ramp. Blue circles show the temperature ratio T/T_F obtained from the size of the polylogarithm fit, while black triangles show the ratio obtained from the fitted fugacity through the relation $T/T_F = [-6\text{Li}(\zeta)]^{-1/3}$. In all figures, the error bars show the standard error derived from 10 repetitions. The time $t = 0$ refers to the beginning of the evaporation in the CDT.

by Pauli blocking in the deeply degenerate regime. Further investigation is needed to understand the final limitations of our cooling scheme.

Figure 4.6 shows our final cooling results for the evaporation ramped discussed before. The absorption images were taken after 14.2 s of evaporation and a time of flight expansion of 2.5 ms for K and 7.5 ms for Dy. The lower panel shows cuts through the 2D profile, and the solid lines show the corresponding fits by a polylogarithmic function. We obtain 4×10^3 K atoms and 1.8×10^4 Dy atoms. At this point the two Fermi energies are calculated to be $E_{F,K}/k_B = 850$ nK for K and $E_{F,Dy}/k_B = 380$ nK for Dy. We measure temperatures of $T_K = 250(10)$ nK and $T_{Dy} = 45(4)$ nK, respectively, corresponding to $T/T_F = 0.29(3)$ for K and $T/T_F = 0.12(1)$ for Dy.

By varying the K MOT loading time we can control the number of ^{40}K atoms in the RDT and the resulting population ratio of the two species at the end of the evaporation. Indeed, after the transfer in the RDT, the K cloud is hotter than the Dy one and a larger number of K atoms thus represents a larger heat load for the Dy cloud, affecting its evaporation dynamics. For final number ratios N_{Dy}/N_K from approximately 4 (corresponding to the situation described in Figs. 4.5 and 4.6) down to 2, we obtain similar cooling performance, with the two species as cold as $T/T_F \approx 0.2$. Then, if we further reduce the number ratio by increasing the initial number of K atoms, the K component reaches lower $T_K/T_{F,K}$ ratios at the expense of $T_{Dy}/T_{F,Dy}$. The absolute temperatures T_{Dy} and T_K achieved actually only weakly depend on the population imbalance. The main effect of the number ratio on the respective T/T_F comes from the dependence of the Fermi temperature on the atom number. In the extreme case where the Dy atom number is zero at the end of the evaporation, we achieve $T/T_F \approx 0.15$ for K.

4.3.4 Effect of Magnetic Levitation

Mixing two species in an optical dipole potential requires careful consideration of the effect of gravity [185]. The effect on the total potential seen by each species is twofold: its minimum is shifted in the vertical direction (referred to as gravitational sag), and its depth is reduced. Because of the different masses and polarizabilities, these two effects have different magnitudes for the two species. In our mixture, gravity has a much stronger effect on Dy than on K, because of both the larger mass and the weaker polarizability. As discussed in Sec. 4.3.2, when we reach optimum cooling results for Dy after 14 s of evaporation, the potential depth is reduced by gravity to only 14% of the optical potential depth. In contrast, the K trap depth is only reduced to 88% of the optical potential depth. At the same point, the potential seen by the Dy atoms is shifted by approximately $7 \mu\text{m}$, which is already comparable to the size of the two clouds, while the sag experienced

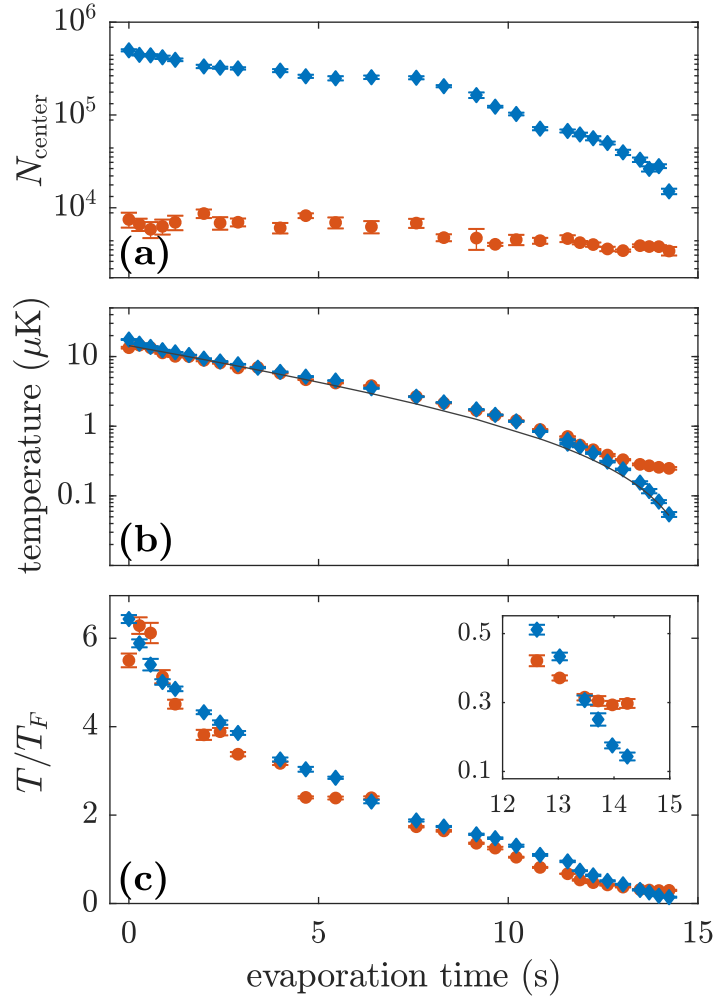


Figure 4.5: Sympathetic cooling of ^{40}K by the evaporatively cooled ^{161}Dy . Atom number, temperature and temperature ratio T/T_F of the ^{40}K (red circles) and ^{161}Dy (blue diamonds) samples during the evaporation of the CDT. As in Figure 4.4, the solid black line in (b) shows the trap depth for Dy reduced by a factor 7. The error bars show the standard error derived from ten repetitions. As in Figure 4.4, the time $t = 0$ refers to the beginning of the final ramp of the CDT.

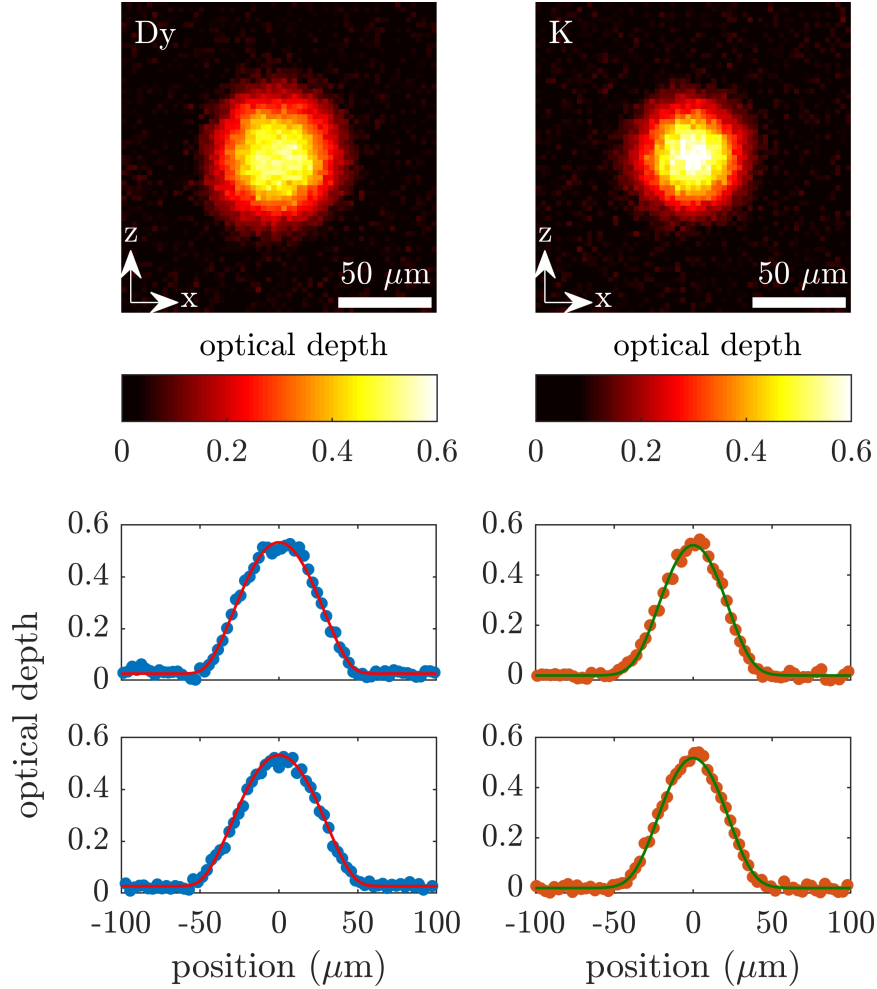


Figure 4.6: Deep cooling of the ^{161}Dy - ^{40}K mixture. Density profile of a cloud of ^{161}Dy (^{40}K) atoms after a time-of-flight expansion of 7.5 ms (2.5 ms) for a ratio $T_{\text{Dy}}/T_{F,\text{Dy}} = 0.12(1)$ ($T_{\text{K}}/T_{F,\text{K}} = 0.29(3)$). Atom numbers are $N_{\text{K}} = 4.0(4) \times 10^3$ and $N_{\text{Dy}} = 1.8(2) \times 10^4$. The upper panel shows the averaged column density of six images obtained with resonant absorption imaging. The lower panels show cuts of the column density along the x (top) and z (bottom) axes. The solid lines are cuts of a 2D fit with a polylogarithmic function.

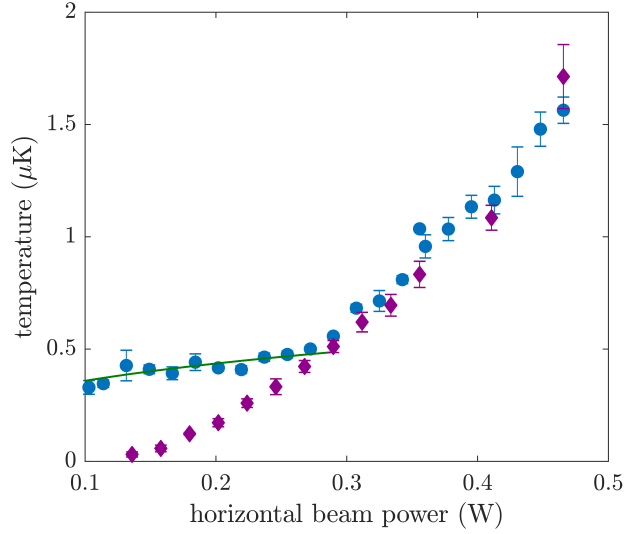


Figure 4.7: Effect of levitation on evaporative cooling. The temperature of a cloud of Dy is measured during the evaporation of the CDT in the absence of levitation (purple diamonds) and when the levitation fields are switched on below 0.3 W (blue points). The solid green line is a fit of the temperature below 0.30 W by an adiabatic cooling model assuming that the temperature for a power P_f in the trap is proportional to the average trap frequency $\bar{\omega}$ at this power: $T(P_f) = b \bar{\omega}(P_f)$ (see main text). The error bars show the standard error derived from six repetitions.

by the K atoms is small (around 500 nm).

When considering a single paramagnetic species, the common way to cancel the effect of gravity is to apply a gradient of magnetic field such that the spatially varying Zeeman energy creates a force opposing the gravitational force [7, 192]. The atomic cloud is then levitated. Because of their different magnetic dipole moments and masses, the strength of the gradient of magnetic field for levitation is different for two different atomic species. Yet, there exists a “magic” value of the gradient such that the gravitational sag of the two species is identical for any power of the optical dipole trap [191]. In the case of Dy and K, the much stronger dipole moment of Dy atoms brings this “magic” value (2.69 G/cm) very close to the value for the levitation of dysprosium (2.83 G/cm).

We demonstrate the effect of the levitation gradient by performing the following experiment. We evaporate dysprosium atoms in the CDT down to a given final power of the horizontal beam and turn on a levitation field when the ramp of power reaches below a threshold value set to 0.3 W. We then

hold the cloud in the trap for 100 ms and finally release it for 8 ms. We extract the temperature from a polylogarithmic fit to the two-dimensional density profile. The measured temperatures are presented in Fig. 4.7. We observe that the evaporation essentially stops when the levitation is turned on, which is a consequence of the corresponding increase of the trap depth. With decreasing power, the temperature still decreases slowly. The green line in Fig. 4.7 is a fit of the temperature for final powers lower than 0.3 W by a function of the form $T(P_f) = b \bar{\omega}(P_f)$, where $\bar{\omega}(P_f)$ is the calculated average trap frequency for a final trap power P_f , and b is a fit parameter. The good agreement between the fit and the measured temperatures shows that the decrease of the temperature in the presence of levitation can be fully attributed to the adiabatic opening of the confinement.

Levitation is an efficient technique to ensure the spatial overlap of two species, and will be a very useful tool in further experiments investigating the physics of Fermi-Fermi mixtures, where full overlap of the two constituents is required. Yet, in our scheme, even in the absence of levitation the two species remain in thermal contact throughout the evaporation ramp, as shown by the efficiency of the sympathetic cooling. This means that we can apply the levitation after the evaporation ramp and benefit from both the positive effects of gravity on evaporative cooling and of levitation on the spatial overlap.

4.3.5 Interspecies Scattering Cross Section

To determine the cross section for elastic collisions between ^{161}Dy and ^{40}K atoms we perform an interspecies thermalization measurement [193–195]. We interrupt the evaporation process in the CDT when the power in the horizontal beam reaches 350 mW. At this point, there are no atoms left in the arms of the CDT. Then we recompress the trap by increasing the power in the horizontal beam to 680 mW to stop plain evaporation. The two atom numbers are $N_{\text{K}} \approx 1 \times 10^4$ and $N_{\text{Dy}} \approx 5 \times 10^4$. The two components are in the thermal regime and their temperatures are equal, around 2 μK . The average trap frequency is $\bar{\omega} = 2\pi \times 1007$ Hz for K atoms, and the peak densities are $n_{\text{K}} = 1.6 \times 10^{13} \text{ cm}^{-3}$ and $n_{\text{Dy}} = 1.4 \times 10^{13} \text{ cm}^{-3}$. We then suddenly displace the horizontal beam in the vertical direction using an AOM and, after a time δt , suddenly displace it back to its original position. After this sequence of two trap displacements, we hold the atoms in the CDT for a variable time and finally measure the temperature of the two components. By setting $\delta t = 2\pi/\omega_z^{\text{Dy}}$ the energy injected in the Dy cloud by the two successive kicks ideally vanishes, while it does not for the K cloud. This kinetic energy of the K atoms is transformed after some typical time τ in thermal energy through collisions with Dy atoms. We measure this thermal energy after a variable hold time by measuring the size of the

K cloud after a time of flight expansion. Following the model developed in [193] and considering the zero energy limit for elastic collisions, the total collision rate is obtained from $\Gamma_{\text{coll}} = \sigma_{\text{el}} v_{\text{rel}} I$, where σ_{el} is the scattering cross section for elastic collisions between Dy and K atoms, v_{rel} is the mean relative velocity of two colliding atoms and $I = \int n_{\text{K}} n_{\text{Dy}} dV$. The relation between the measured thermalization time τ and the total collision rate is described in Appendix 4.5.4.

Figure 4.8 shows a thermalization curve, where the measured size of the K sample is interpreted in terms of a temperature ⁴. The temperatures of the two species approach each other as we hold the cloud in the trap. Because of the number ratio $N_{\text{Dy}}/N_{\text{K}} \approx 5$, the dominant effect is observed as a reduction of the K temperature, while the Dy temperature only slightly increases. Our observation is consistent with a simple heat transfer from the K sample to the Dy one. Atom numbers of both species are constant on the time scale of the measurement.

The temperatures of the two species enter in the value of v_{rel} and of the overlap integral I ; see Appendix 4.5.4. It turns out that, given the mass and polarizability ratios of Dy and K, the opposite effects of temperatures on v_{rel} and I nearly balance each other and thus lead to an almost constant value of Γ_{coll} for a temperature ratio $T_{\text{K}}/T_{\text{Dy}} \lesssim 2$. Since at these temperatures the elastic scattering cross section is almost constant, the measured temperatures evolve in a quasi-exponential way during the thermalization process. From an exponential fit of the temperature of K for hold times larger than 80 ms we extract a thermalization time constant of $\tau = 130$ ms. This corresponds to an elastic scattering cross section of $\sigma_{\text{el}} \approx 1.4 \times 10^{-16} \text{ m}^2$, with an estimated error of 15% including all statistical and systematic errors. We calculate the cross section for elastic dipolar collisions between Dy and K atoms to be two orders of magnitude smaller than the measured cross section ⁵. We therefore attribute the measured cross section to the contact interaction and deduce the corresponding scattering length $|a_{\text{DyK}}| \approx 62 a_0$. We point out that the measured interspecies cross section is one order of magnitude smaller than the dipolar cross section for elastic collisions be-

⁴Since the ⁴⁰K cloud cannot thermalize by itself after the excitation, interspecies collisions are needed to reach thermal equilibrium. For shorter times, the ⁴⁰K cloud can therefore not be described by a temperature in a strict thermodynamic sense. Here we use an effective temperature as a measure of the cloud's kinetic energy in the center-of-mass frame.

⁵The elastic dipolar cross section for interspecies collisions is obtained from $\sigma_{\text{dip}} = (16/45)\pi a_D^2 + (16/15)\pi a_D^2$, where the two terms represent the contributions of even and odd partial waves respectively. The dipolar length a_D is given by $a_D = \mu_0 \mu_{\text{K}} \mu_{\text{Dy}} m_r / (4\pi \hbar^2)$. Here μ_0 is the permeability of vacuum, μ_{K} and μ_{Dy} are the magnetic dipole moments of K and Dy atoms in the relevant spin states, and m_r is the reduced mass. We calculate $\sigma_{\text{dip}} = 7.2 \times 10^{-19} \text{ m}^2$

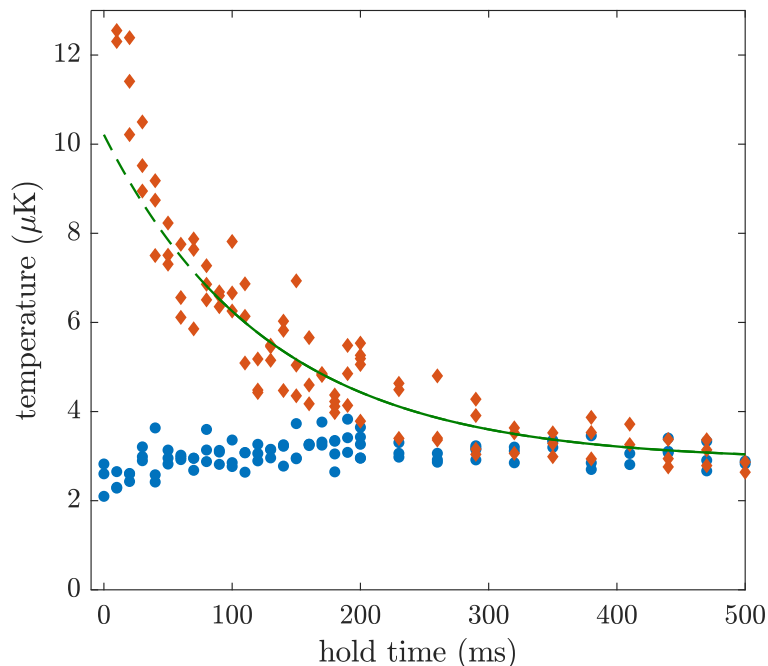


Figure 4.8: Cross-species thermalization measurement. The temperatures of the ^{40}K (red diamonds) and ^{161}Dy (blue circles) are shown versus the hold time after the species-selective heating by the trap displacements (see text). The solid green line is a fit of the temperature of the K atoms by an exponential curve for a hold time bigger than 80 ms. The dashed line extrapolates the fit.

tween identical ^{161}Dy atoms ($\sigma_{\text{dip,Dy}} = 7.2 \times 10^{-16} \text{ m}^2$).

4.4 Conclusion and Outlook

We have demonstrated how a deeply degenerate Fermi-Fermi mixture of ultracold ^{161}Dy and ^{40}K atoms can be efficiently produced in an optical dipole trap. The cooling process relies on the evaporation of the spin-polarized Dy component, with elastic collisions resulting from universal dipolar scattering. The K component is sympathetically cooled by elastic s -wave collisions with Dy. In this way, we have reached conditions with about 2×10^4 Dy atoms and about 5×10^3 K atoms at temperatures corresponding to $\sim 10\%$ and $\sim 30\%$ of the respective Fermi temperature. This represents an excellent starting point for future experiments aiming at the realization of novel quantum phases and superfluid states in mass-imbalanced fermionic mixtures.

The next challenge in our experiments will be the implementation of inter-species interaction tuning by means of magnetically tuned Feshbach resonances [50]. Although the particular interaction properties of our mixture are yet unknown, one can expect many Feshbach resonances to arise from the anisotropic electronic structure of the Dy atom [90, 196]. The key question, which we will have to answer in near-future experiments, is whether sufficiently broad Feshbach resonances exist to facilitate interaction tuning along with a suppression of inelastic losses. Reason for optimism is given by the fact that rather broad Feshbach resonances have been found in single-species experiments with Er and Dy [197–199].

If nature will be kind to us and provide us with a good handle to control interactions in the resonant regime, then the future will look very bright for novel superfluid phases in Dy-K Fermi-Fermi mixtures. A very favorable property of this mixture, as we pointed out already in Ref. [182], is the fact that the polarizability ratio of the two species in an infrared optical dipole trap nearly corresponds to the inverse mass ratio. This will allow to easily match the Fermi surfaces of both species even in the inhomogeneous environment of a harmonic trap, and to investigate pairing and superfluidity of unequal mass particles in the crossover from molecular BEC to a BCS-type regime. Moreover, our preparation naturally produces a situation with a majority of heavier atoms, which is exactly what will be needed to realize FFLO states in mass- and population-imbalanced fermionic mixtures [32, 33].

4.5 Appendix

4.5.1 Apparatus

Here, we describe briefly our apparatus. We use two independent and spatially separated atomic sources for the two species, which provide collimated atomic beams in the main vacuum chamber through two different ports. As mentioned in Sec. 4.2.1, our source of Dy atoms consists of a commercial high-temperature effusion oven operating at about 1000°C combined with a Zeeman slower. The atomic flux through the Zeeman slower is increased by a transverse cooling stage applied at the exit of the oven, operating on the same broad transition as the Zeeman slower.

The K source is a two-dimensional MOT in a glass cell [200], loaded from the background pressure created by commercial isotopically enriched K dispensers (Alvatec), placed directly inside the glass cell. The glass cell is connected to the main vacuum chamber by a differential pumping tube. The two-dimensional MOT operates on the D2 line of K, and is created by two perpendicular retro-reflected elliptical laser beams and by a two-dimensional

quadrupole magnetic field realized by two pairs of coils. The transversally cooled atoms are trapped around the line of zero magnetic field, forming a cigar-shaped cloud. An additional beam pushes the cloud through the differential pumping tube in the main chamber.

The K and Dy three-dimensional MOT beams are overlapped in a four fiber cluster, which distributes the light to the four MOT beam paths. The MOTs are created by two retro-reflected orthogonal beams in the horizontal plane, and by two counter-propagating vertical beams. The narrow character of the 626 nm line causes the Dy cloud to sit below the zero of the magnetic field, hence requiring the large diameter MOT beams (35 mm in our case). The laser light at 626 nm is spectrally broadened by a high-efficiency electro-optical modulator resonant at 104 kHz, which adds around 30 sidebands.

4.5.2 Imaging of the Atomic Cloud

The K and Dy atoms are imaged through the same imaging set-up, on a single sCMOS camera (Andor Neo), along an axis that lies in the horizontal plane (about 40° to the x axis). We use resonant absorption imaging on the D2 line of wavelength 767 nm for K, and on the broad line at 421 nm for Dy. The two probe beams are overlapped on a dichroic mirror and have σ^- polarization. The imaging sequence involves four laser pulses and one background picture: each species requires one pulse to image the atoms followed by one normalization pulse. The background picture without probe light is taken in the end of the imaging sequence. From the moment where the CDT is switched off, we wait a time corresponding to the time of flight for K, and shine the pulse imaging K atoms for 10 μ s. We then wait a variable time which sets the difference between the two values for the time of flight applied to K and Dy, and shine the pulse imaging Dy atoms for 10 μ s. The minimum time between the two pulses is 500 ns. The two normalization pictures are taken 40 ms after the respective pictures of the atoms. In both cases, the scattering cross section is assumed to be the resonant cross section for a two-level system.

4.5.3 Cooling ^{40}K on the D1 Line

After preparation in the MOTs, the K and Dy components have very different temperatures. However, optimal efficiency of the subsequent evaporative cooling stage requires similar starting conditions for the two species. In order to reach this situation, we perform after the MOT stage sub-Doppler cooling of the K atoms in the form of a gray molasses on the D1 line. While this cooling technique has been demonstrated in free space [123], we describe here its successful implementation in the presence of our large-volume reservoir

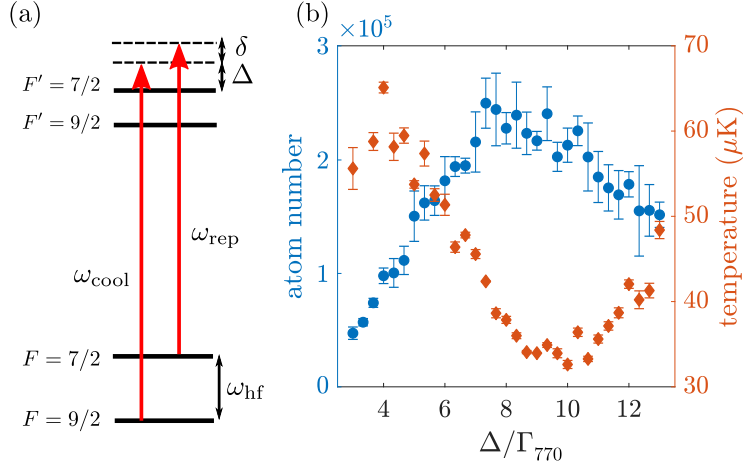


Figure 4.9: D1 cooling of ^{40}K . (a) Levels structure of the D1 transition and laser scheme. (b) Atom number and temperature at the end of the D1 cooling step in the RDT, as a function of the detuning Δ , when δ is kept to zero.

optical dipole trap (Sec. 4.2.2). In this situation, the dissipative nature of the molasses cooling improves significantly the phase-space density reached after transfer into the optical dipole trap. We account for the effect of the space-dependent light shift by ramping the laser parameters, as we describe in the following.

The laser beams creating the gray molasses are overlapped on polarizing beam splitters with the MOT beams, which fixes their polarization to circular with opposite helicity compared to the MOT beams. The cooler and repumper beams are blue-detuned relative to the $F = 9/2 \rightarrow F' = 7/2$ and $F = 7/2 \rightarrow F' = 7/2$ transitions respectively. We define Δ as the detuning of the cooling beam relative to the bare (in the absence of light shift) $9/2 \rightarrow 7/2$ line and $\delta = \omega_{\text{rep}} - \omega_{\text{cool}} + \omega_{\text{hf}}$, where ω_{cool} is the frequency of the cooling beam, ω_{rep} is the frequency of the repumper, and ω_{hf} is the hyperfine splitting in the ground state of ^{40}K ; see Fig. 4.9(a).

After the compression of the K MOT, the gradient of magnetic field is set to zero, and residual homogeneous magnetic fields are canceled to the level of 10 mG. The D2 light is switched off and D1 light is switched on. The RDT is turned on beforehand during the MOT and its power is kept unchanged (see Sec. 4.2.2). At this point, the cloud sits on top of the crossed RDT, though being larger.

Because the polarizability of the excited state at 1064 nm is negative, the transition is shifted to higher frequency by the ac Stark shift in the center of the trap compared to the wings of the potential. We therefore use a two-step D1 cooling scheme, in which the intensities and the detuning Δ are first kept constant and then tuned in linear ramps. During the initial capture phase of 0.6 ms, the power and detunings are kept constant at $I^{\text{cool}} = 5.8 I_{\text{sat},770}$, $I^{\text{rep}} = 0.11 I_{\text{sat},770}$ and $\delta = 0, \Delta = 3 \Gamma_{770}$ (where $I_{\text{sat},770} = 1.70 \text{ mW cm}^{-2}$ is the saturation intensity of the D1 line of K and Γ_{770} its natural linewidth), which are the parameters found to be optimal for D1 cooling in free space. In the second phase, powers are ramped down in 20 ms to $I^{\text{cool}} = 0.18 I_{\text{sat}}$ and $I^{\text{rep}} \approx 0.01 I_{\text{sat}}$ while the cooler and repumper are detuned further to the blue. The ramp of frequencies thus allows us to cool atoms from the outer region into the trap. Figure 4.9(b) shows the final atom number and temperature of the K cloud as the final value of Δ is varied. We achieve a temperature of 27(1) μK for a final value $\Delta = 9 \Gamma_{770}$.

4.5.4 Interspecies Thermalization

We summarize here the model developed by Mosk *et al.* [193], which describes the thermalization between two species in a harmonic trap (we assume here that the two species have the same central position). We reproduce in particular the relation between the elastic cross section σ_{el} and the thermalization time τ . First, we calculate the total collision rate $\Gamma_{\text{coll}} = \sigma_{\text{el}} v_{\text{rel}} I$. The mean relative velocity is obtained as

$$v_{\text{rel}} = \sqrt{\frac{8k_{\text{B}}}{\pi} \left(\frac{T_{\text{K}}}{m_{\text{K}}} + \frac{T_{\text{Dy}}}{m_{\text{Dy}}} \right)}. \quad (4.1)$$

Assuming a thermal density distribution of the two components, one calculates the overlap integral

$$I = N_{\text{K}} N_{\text{Dy}} \bar{\omega}_{\text{Dy}}^3 \left(\frac{2\pi k_{\text{B}} T_{\text{Dy}}}{m_{\text{Dy}}} \right)^{-3/2} \left(1 + \frac{\alpha_{\text{Dy}}}{\alpha_{\text{K}}} \frac{T_{\text{K}}}{T_{\text{Dy}}} \right)^{-3/2}. \quad (4.2)$$

Based on the ratios of polarizabilities, masses, and temperatures, we define the quantity

$$A = \left(1 + \frac{m_{\text{Dy}}}{m_{\text{K}}} \frac{T_{\text{K}}}{T_{\text{Dy}}} \right)^{1/2} \left(1 + \frac{\alpha_{\text{Dy}}}{\alpha_{\text{K}}} \frac{T_{\text{K}}}{T_{\text{Dy}}} \right)^{-3/2}. \quad (4.3)$$

Combining (4.1,-4.3) we deduce the collision rate

$$\Gamma_{\text{coll}} = \sigma_{\text{rel}} \frac{m_{\text{Dy}} \bar{\omega}_{\text{Dy}}^3}{\pi^2 k_{\text{B}} T_{\text{Dy}}} N_{\text{Dy}} N_{\text{K}} A. \quad (4.4)$$

We assume [193] that the average energy transfer during one Dy-K collision is given by $\Delta E = \xi k_B(T_K - T_{\text{Dy}})$, where $\xi = 4m_{\text{Dy}}m_K/(m_{\text{Dy}}+m_K)^2$ accounts for the effect of the mass imbalance. Using this expression, we obtain the relation relating the collision rate Γ_{coll} and the thermalization time τ :

$$\tau^{-1} = \frac{1}{\Delta T} \frac{d}{dt} \Delta T = \xi \frac{N_{\text{Dy}} + N_K}{3N_{\text{Dy}}N_K} \Gamma_{\text{coll}} . \quad (4.5)$$

One finally finds the relation

$$\tau^{-1} = \sigma_{\text{el}} \frac{\xi}{3\pi^2} \frac{m_{\text{Dy}} \bar{\omega}_{\text{Dy}}^3}{k_B T_{\text{Dy}}} (N_{\text{Dy}} + N_K) A \quad (4.6)$$

between the thermalization time and the scattering cross section. Given the mass and polarizability ratios of Dy and K [182], there is only a weak dependence of A on the temperature ratio for the range of temperatures that we consider. We calculate $A \approx 1.5$, which allows us to analyze the near-exponential thermalization curve presented in Fig. 4.8.

Chapter 5

Preprint: Resonantly Interacting Fermi-Fermi Mixture of ^{161}Dy and ^{40}K

Preprint available as:

C. Ravensbergen, E. Soave, V. Corre, M. Kreyer,
B. Huang (黄博), E. Kirilov and R. Grimm
[arXiv:1909.03424v3](https://arxiv.org/abs/1909.03424v3)

Author contribution: The author took a leading role in the process of acquiring and analyzing the data described in this publication as well as contributed to the writing of the manuscript.

Changes with respect to the original publication: Subsection headlines have been added.

We report on the realization of a Fermi-Fermi mixture of ultracold atoms that combines mass imbalance, tunability, and collisional stability. In an optically trapped sample of ^{161}Dy and ^{40}K , we identify a broad Feshbach resonance centered at a magnetic field of 217 G. Hydrodynamic expansion profiles in the resonant interaction regime reveal a bimodal behavior resulting from mass imbalance. Lifetime studies on resonance show a suppression of inelastic few-body processes by orders of magnitude, which we interpret as a consequence of the fermionic nature of our system. The resonant mixture opens up intriguing perspectives for studies on novel states of strongly correlated fermions with mass imbalance.

5.1 Introduction

Ultracold Fermi gases with resonant interactions have attracted a great deal of attention as precisely controllable model systems for quantum many-body physics [34, 177–179]. The interest spans across many different fields, from primordial matter, neutron stars and atomic nuclei to condensed-matter systems, and in particular concerning superfluids and superconductors [29]. Corresponding experiments in ultracold Fermi gases require strong *s*-wave interactions, which can be realized based on Feshbach resonances [50] in two-component systems. The vast majority of experiments in this field relies on spin mixtures of fermionic atomic species, which naturally imposes equal masses. Beyond this well-established situation, theoretical work has predicted fermionic systems with mass imbalance to favor exotic interaction regimes [32]. Mass-imbalanced systems hold particular promise [33, 153] in view of superfluid states with unconventional pairing mechanisms, most notably the elusive Fulde-Ferrell-Larkin-Ovchinnikov (FFLO) state [65, 149, 150].

A key factor for experiments on resonantly interacting Fermi gases is the collisional stability that arises from a suppression of inelastic loss processes at large scattering lengths. This effect is a result of Pauli exclusion in few-body processes at ultralow energies [79, 173]. To act efficiently in an experiment, the suppression requires a broad *s*-wave Feshbach resonance with a sufficiently large universal range [173, 201]. For the mass-balanced case, suitable resonances exist in spin mixtures of ^6Li or ^{40}K , and such systems are used in many laboratories worldwide. In a mass-imbalanced fermion system, the same suppression effect can be expected [89]. However, the only *s*-wave tunable Fermi-Fermi system realized so far is the mixture of ^6Li and ^{40}K [83, 84], for which the Feshbach resonances [73, 77, 169] are too narrow to enable strong loss suppression [78].

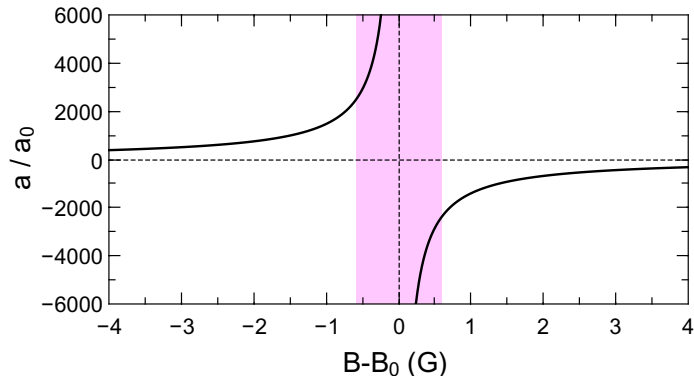


Figure 5.1: Interspecies scattering length a for ^{161}Dy - ^{40}K near the broad Feshbach resonance centered at $B_0 \approx 217$ G. The shaded region indicates the regime where a exceeds all other relevant length scales (see text).

The advent of submerged-shell lanthanide atoms in the field of ultracold quantum gases [45, 47, 100, 101] has considerably enhanced the experimental possibilities. While most of the current work focuses on interactions that result from the large magnetic dipole moment or the complex optical transition structure, the availability of additional fermionic atoms is of great interest in view of novel ultracold mixtures and strongly interacting systems [176, 180]. We have recently introduced the mixture of ^{161}Dy and ^{40}K [182, 202] as a candidate for realizing a collisionally stable, strongly interacting Fermi-Fermi mixture. Many narrow Feshbach resonances can be expected for such a system as a result of anisotropic interatomic interactions [90, 181]. However, the key question in view of future experiments has remained, whether suitable broad resonances would exist.

In this Letter, we report on a broad Feshbach resonance in the ^{161}Dy - ^{40}K mixture with its center found near 217 G. We have identified this resonance (see Fig. 5.1) as the strongest one in a scenario of three overlapping resonances 5.7, with the other two at 200 G and 253 G. Some weak (only few mG wide) interspecies resonances do also exist in the relevant region, but they can be ignored for understanding the general structure of the broad scenario. We have characterized the three resonances by interspecies thermalization measurements, as reported in detail in 5.7. Close to the center of the strongest resonance, the tunability of the interspecies s -wave scattering length can be well approximated by

$$a = -\frac{A}{B - B_0} a_0, \quad (5.1)$$

where a_0 is Bohr's radius. Our best knowledge of the pole position and the strength parameter is $B_0 = 217.27(15)$ G and $A = 1450(230)$ G 5.7.

5.2 Sample Preparation

The starting point of our experiments is a degenerate mixture of ^{161}Dy and ^{40}K , prepared in crossed-beam optical dipole trap according to the procedures described in our earlier work [202]. Evaporative cooling is performed at a low magnetic field of 225 mG. Both species are in their lowest hyperfine and Zeeman substates, which excludes two-body losses. The transfer of the system into the high-field region above 200 G is challenging, because many Dy intraspecies [48, 187] and Dy-K interspecies resonances have to be crossed in a fast ramp of the magnetic field. To minimize unwanted losses, heating, and excitations of the trapped cloud we proceed in two steps. Within a few ms, we ramp up the magnetic bias field to 219.6 G ¹, where the system is given a time of a few 10 ms to settle and establish thermal equilibrium. We then apply a very fast (2-ms) small-amplitude ramp to the target field, where the experiments are carried out. Throughout the whole sequence after evaporation, a magnetic levitation field is applied to compensate for the relative gravitational sag of both species [202]. In this way, we reach typical conditions of $N_{\text{Dy}} = 20\,000$ and $N_{\text{K}} = 8\,000$ atoms at a temperature of $T = 500\text{ nK}$ ² in a slightly elongated trap (aspect ratio ~ 2) with mean oscillation frequencies of $\bar{\omega}_{\text{Dy}}/2\pi = 120\text{ Hz}$ and $\bar{\omega}_{\text{K}}/2\pi = 430\text{ Hz}$ ³ and depths corresponding to $3.5\text{ }\mu\text{K}$ and $10\text{ }\mu\text{K}$, respectively. With Fermi temperatures of $T_F^{\text{Dy}} = 290\text{ nK}$ and $T_F^{\text{K}} = 750\text{ nK}$, our experimental conditions are near-degenerate of ($T/T_F^{\text{Dy}} = 1.7$ and $T/T_F^{\text{K}} = 0.65$).

5.3 Interaction Characterization

Interaction regimes near resonance can be discussed by comparing the scattering length with other relevant length scales. To characterize the interaction strength on resonance, where scattering is limited by unitarity [203, 204], we define a length scale corresponding to the inverse wave number of the relative motion $1/\bar{k}_{\text{rel}} = \hbar/(m_r\bar{v}_{\text{rel}})$, where $\bar{v}_{\text{rel}} = \sqrt{8k_B T/(\pi m_r)}$ is the mean relative velocity and m_r denotes the reduced mass. The typical interparticle distance sets another length scale, for which we adopt a common definition for two-component Fermi gases, $d = (3\pi^2 n_{\text{tot}})^{-1/3}$, where n_{tot} is the total number density of both species in the trap center. For our typical experimental parameters, we obtain $1/\bar{k}_{\text{rel}} \approx 2100 a_0$ and $d \approx 2500 a_0$. The scattering length exceeds $1/\bar{k}_{\text{rel}}$ in a magnetic field range of roughly $\pm 0.7\text{ G}$. In this resonant interaction regime, scattering is dominated by the unitar-

¹At 219.6 G interspecies thermalization is sufficiently fast and Dy background losses show a pronounced minimum.

²Thermometry is based on time-of-flight images taken at high magnetic fields in regions where interspecies interactions are weak.

³The ratio of the trap frequencies for K and Dy is essentially determined by the mass ratio and the polarizability ratio, which results in a $\bar{\omega}_{\text{K}}/\bar{\omega}_{\text{Dy}} = 3.60$ [182].

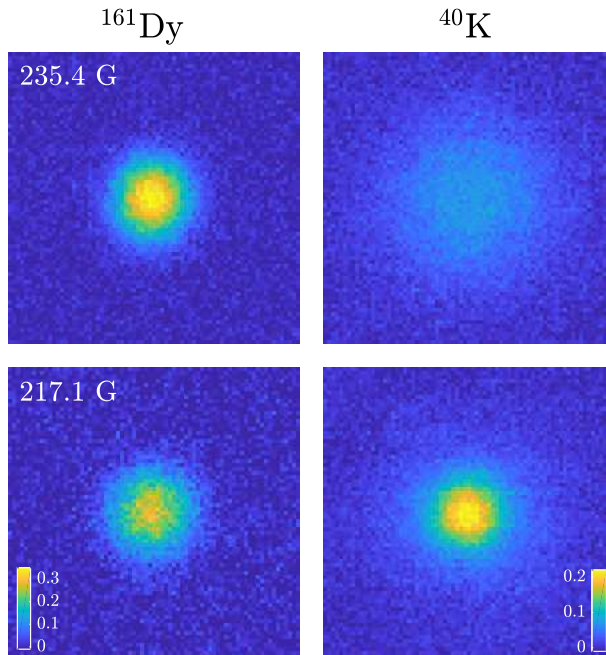


Figure 5.2: Comparison of the expansion of the mixture for weak (upper) and resonant (lower) interspecies interaction. The absorption images show the optical depth for both species (Dy left, K right) after a time of flight of 4.5 ms. The field of view of all images is $240 \mu\text{m} \times 240 \mu\text{m}$.

ity limitation. In addition to that, the values of $1/\bar{k}_{\text{rel}}$ and d are similar, which means that the system is in the crossover between weak and strong interactions. A further length scale is set by the effective range of the resonance [50]. Its value is presently unknown because of the yet undetermined magnetic moment of the molecular state underlying the resonance, but we expect the effective range 5.7 to be rather small in comparison to realistic values of the scattering length and the interparticle spacing, so that the interaction physics will be dominated by universal behavior.

5.4 Hydrodynamic Expansion

A striking effect of the resonant interspecies interaction shows up in the expansion of the mixture. In the experiments, the sample was released from the trap right after switching to the target field strength. The absorption images in the upper row of Fig. 5.2 illustrate the case of weak interactions ($a \approx -40 a_0$), realized at $B = 235.4 \text{ G}$. Here the expansion takes place in a ballistic way and, as expected from the mass ratio, the K component expands much faster than the Dy component. In contrast, in the resonant

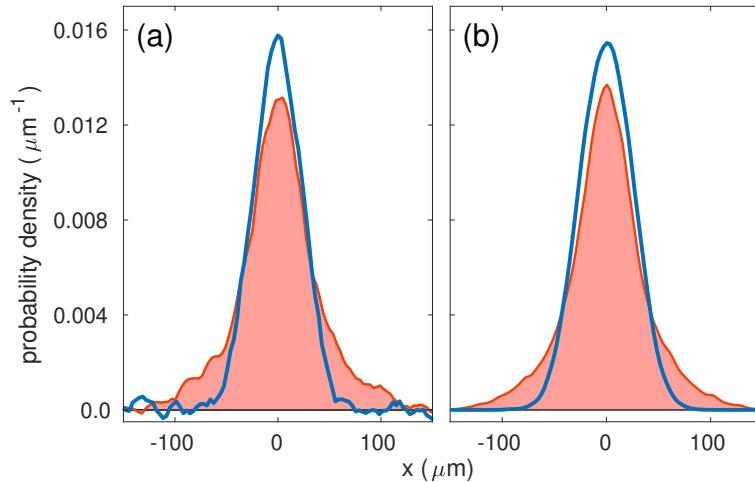


Figure 5.3: Profiles of the hydrodynamically expanding mixture for resonant interaction, (a) experimentally observed and (b) from a corresponding Monte-Carlo simulation. Shown are the probability densities of doubly-integrated profiles for both Dy (solid blue lines) and K (red curve with filling).

case (images in the lower row of Fig. 5.2) both components expand with similar sizes. Evidently, the interaction between the two species slows down the expansion of the lighter species and accelerates the expansion of the heavier species. Such a behavior requires many elastic collisions⁴ on the timescale of the expansion and thus can be interpreted as a hallmark of hydrodynamic behavior.

A closer inspection of the spatial profiles of the hydrodynamically expanding mixture reveals an interesting difference between the heavy and the light species; see profiles in Fig. 5.3. While the Dy cloud essentially keeps its near-Gaussian shape, the K cloud (initially about twice smaller than the Dy cloud) develops pronounced side wings. Apparently, the mixture forms a hydrodynamic core surrounded by a larger cloud of ballistically expanding lighter atoms.

To elucidate the origin of this surprising effect we have carried out a Monte-Carlo simulation [205], accounting for the classical motion and the quantum-mechanically resonant collisional cross section, which is only limited by the finite relative momentum of a colliding pair [203, 204]. For our near-degenerate conditions, we neglect Pauli blocking and interactions beyond

⁴We estimate the collision rate for a K atom in the center of the Dy cloud by considering the resonant elastic scattering cross section $\sigma_{\text{res}} = 4\pi/\bar{k}_{\text{rel}}^2$, the Dy peak number density \hat{n}_{Dy} , and the mean relative velocity \bar{v}_{rel} . For our typical conditions, $\hat{n}_{\text{Dy}}\sigma_{\text{res}}\bar{v}_{\text{rel}} \approx 10^4 \text{ s}^{-1}$.

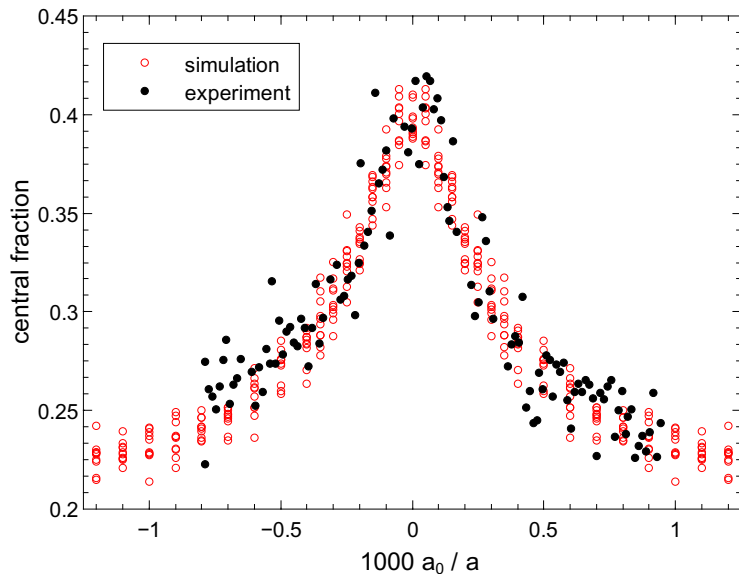


Figure 5.4: Enhancement of the central fraction of K atoms in the expanding mixture. Experimental results for the resonance behavior (filled black symbols) are shown in comparison with Monte-Carlo simulation results (red open symbols).

two-body collisions. The simulation results in Fig. 5.3(b) reproduce the experimental profiles (a) without any free parameter. The simulation confirms our interpretation in terms of a hydrodynamic core, where both species collide with each other at a large rate, surrounded by a ballistically expanding cloud of light atoms. The physical mechanism for the formation of the latter is the faster diffusion of lighter atoms, which can leak out of the core and, in the absence of the other species, begin to move ballistically. We point out that this bimodality effect is not an experimental imperfection, but a generic feature in the hydrodynamic expansion of a mass-imbalanced mixture.

To investigate the dependence of the hydrodynamic expansion on the scattering length, we recorded two-dimensional expansion profiles (such as in Fig. 5.2) for various values of B in a 2-G wide range around the resonance center. We focus our analysis on the K profiles as they reveal the hydrodynamic core, while the Dy profiles only show a slight increase in width. As a quantitative measure we define the “central fraction” as the fraction of K atoms in a circle of particular radius. For the latter we use the $\sqrt{2}\sigma$ -width of the non-interacting Dy cloud ($\sim 34\mu\text{m}$ at a 4.5-ms time of flight). We find a marked increase of the central fraction from its non-interacting background value 0.22 to a resonant peak value of about 0.40. As a function

of the magnetic detuning $B - B_0$, the central fraction shows a pronounced resonance behavior, which closely resembles a Lorentzian curve. From a fit we derive the center $B_0 = 217.04\text{G}$ and a width (half width at half maximum) of 0.37G . We finally use Eq. (5.1) with the fixed value $A = 1450\text{G}$ to convert the magnetic detuning scale into an inverse scattering length and plot the data as shown in Fig. 5.4.

For comparison, we have also employed our Monte-Carlo approach to calculate the central fraction as function of the scattering length. Figure 5.4 shows the simulation results (red open symbols) together with the experimental data (black closed symbols). We find that the simulation reproduces the experimental observations very well. This agreement between experiment and theory strongly supports our qualitative and quantitative understanding of both the resonance scenario and the expansion dynamics.

For a precise determination of the resonance center, measurements based on the hydrodynamic expansion can in general provide much sharper resonance features than simple thermalization [82]. While our expansion measurement yielded $217.04(1)\text{G}$ for the resonance center B_0 , the thermalization measurement 5.7 resulted in a value of $217.27(15)\text{G}$, somewhat higher and with a statistical uncertainty more than an order of magnitude larger. Whether the apparent deviation is a pure statistical effect (about 1.5σ), whether it is caused by magnetic-field control issues ⁵, or whether there are unknown systematic effects behind it requires further investigation. We note that anisotropic expansion effects in our nearly spherical trap remain very weak and are barely observable. The anisotropic expansion of a hydrodynamic, strongly interacting Fermi-Fermi system has been studied in our earlier work on a resonant ${}^6\text{Li}$ - ${}^{40}\text{K}$ mixture [83].

5.5 Lifetime

We now turn our attention to the lifetime of the mixture in the resonance region. In general, we find the magnetic-field dependence of losses to exhibit a very complex behavior 5.7. Both Dy-K interspecies and Dy intraspecies losses show strong fluctuations with a variation of the magnetic field. A broad loss feature appears about 0.5G below the 217-G resonance, where the scattering length is very large and positive. This feature closely resembles observations made in spin mixtures of ${}^6\text{Li}$ [175, 206, 207] and ${}^{40}\text{K}$ [82], which have been understood as signature of the formation of weakly bound dimers. In addition to this broad feature, additional narrower structures appear, which make the experiment very sensitive to the particular choice of the

⁵Day-to-day fluctuations, drifts in the calibration, and residual ramping effects may cause magnetic-field uncertainties of the order of 100mG .

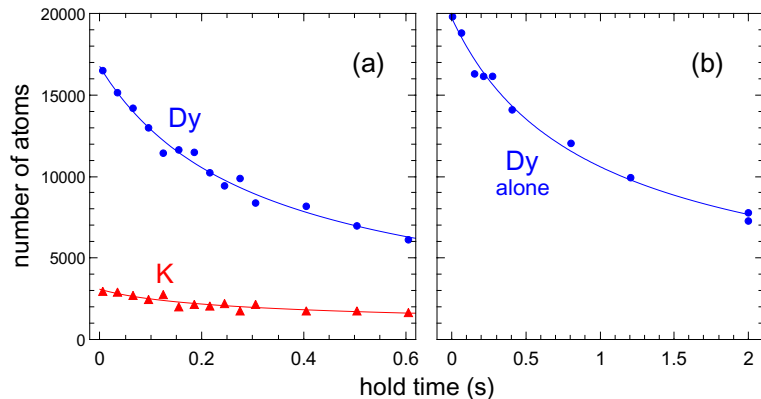


Figure 5.5: Decay of the resonant Dy-K mixture (a) in comparison with a pure Dy sample (b) at magnetic field $B = 217.5$ G, very close to the resonance pole. The solid lines show fits by a phenomenological model 5.7.

magnetic field. Nevertheless, several good regions exist close to the center of the broad Feshbach resonance under conditions, where losses are relatively weak and s -wave scattering is deep in the unitarity-limited regime.

As an example for long lifetimes attainable in the resonance region, Figure 5.5 shows a set of measurements taken at field strength of 217.5 G, for which we estimate a large negative scattering length of $-3000 a_0$ or even larger. We have fitted and analyzed the decay of the atom numbers following the procedures detailed in 5.7. For the number of K atoms, our data show an initial time constant of about 350 ms. If we attribute this decay completely to K-Dy-Dy (K-K-Dy) three-body processes, we obtain the upper limits of $4 \times 10^{-25} \text{ cm}^6/\text{s}$ ($3 \times 10^{-25} \text{ cm}^6/\text{s}$) for the event rate coefficients. These values are very small compared with other resonant three-body systems that do not involve identical fermions. In Feshbach-resonant Bose-Bose [208–210] or Bose-Fermi mixtures [211–215], event rate coefficients have been measured exceeding $10^{-23} \text{ cm}^6/\text{s}$, i.e. at least two orders of magnitude more. In preliminary experiments [216] on Bose-Fermi mixtures of Dy-K (bosonic isotope ^{162}Dy), we have also observed a dramatic increase of resonant three-body losses by orders of magnitude. We attribute the low values of the three-body rate coefficients and thus the long lifetimes in our Fermi-Fermi system to the Pauli suppression of inelastic losses [79, 89, 173].

The decay of the Dy component in the mixture, displayed in Fig. 5.5(a) by the blue data points and the corresponding fit curve, shows a peculiar behavior. Since we find that about 10 times more Dy atoms are lost as compared to K atoms, three-body interspecies collisions may only explain a small fraction of Dy losses. As Figure 5.5(b) shows, Dy alone exhibits

losses even without K being present, but much weaker. Interpreting these losses as Dy intraspecies losses, gives values for the event rate coefficient of $3.4 \times 10^{-25} \text{ cm}^6/\text{s}$ in the presence of K, but only $0.8 \times 10^{-25} \text{ cm}^6/\text{s}$ without K 5.7. These observations point to an unknown mechanism, in which K atoms somehow catalyze the decay of Dy without directly participating in the loss processes. A possible mechanism may be due to elastic collisions with K atoms causing residual evaporation. We tested this in our experiments by recompressing the trap, but did not observe significant changes in the observed loss behavior. Another hypothesis is based on a spatial contraction (density increase) of the Dy cloud caused by strong interaction effects with K atoms. Considering the zero-temperature limit, we have developed a model 5.7 for such an effect, but its applicability is questionable at the temperatures of our present experiments. The explanation of the mysterious enhancement of Dy losses induced by K remains a task for future experiments.

5.6 Discussion and Conclusion

Already our present experiments, carried out near quantum degeneracy ($T/T_F^K \approx 0.65$), demonstrate that mass imbalance can make a qualitative difference in the physical behavior of a strongly interacting fermion mixture. The bimodality observed in the hydrodynamic expansion profile of the lighter component is seemingly similar to observations in population-imbalanced spin mixtures near the superfluid phase transition [217]. However, while in the latter case bimodality signals superfluidity, the reason is a different one in our case. Detailed understanding of the expansion dynamics of a Fermi-Fermi mixture in different classical and quantum regimes is thus essential for interpreting the expansion profiles in future work aiming at superfluid regimes. For reaching lower temperatures and deeper degeneracy, work is in progress to eliminate heating in the transfer from low to high magnetic fields and to implement an additional evaporative cooling stage that takes advantage of the large elastic scattering cross section close to the resonance. The experimental challenge is to realize similar degeneracy conditions near the 217-G resonance as we have achieved at a low magnetic field [202]. With some improvements, conditions for superfluid regimes seem to be attainable. To give an example, a Lifshitz point [139, 153] in the phase diagram, where zero momentum pairs become unstable, may be expected at a temperature corresponding to about 15% of the Fermi temperature of the heavy species ⁶.

In conclusion, we have shown that the ^{161}Dy - ^{40}K mixture possesses a broad Feshbach resonance offering favorable conditions for experiments on strongly interacting fermion systems with mass imbalance. In particular, the system

⁶Note that in Ref. [153] temperatures are given in units of a reduced Fermi temperature, which at the Lifshitz point is a factor of 3.4 higher than the Fermi temperature of the heavy species.

features a substantial suppression of inelastic losses near resonance, which is a key requirement for many experiments. Novel interaction regimes, including unconventional superfluid phases, seem to be in reach.

5.7 Supplemental Material

5.7.1 Feshbach resonance scenario

To date, no theoretical model is available that would describe the scattering properties of our Dy-K mixture. Our experimental characterization in the region of interest therefore relies on a combination of various observables, like the positions of resonance poles and zero crossings, and measurements of the interspecies thermalization time. Our basic model assumption is a scenario of three partially overlapping *s*-wave Feshbach resonances.

Wide-range thermalization scan

Figure 5.6 shows a thermalization scan over the wide magnetic field range from 155 to 255 G. After evaporatively cooling the mixture at low magnetic fields down to a temperature of about $1.3\ \mu\text{K}$, a short period (60 ms) of species-selective parametric heating by trap power modulation was applied to increase the temperature of the 1.4×10^4 K atoms to about $4\ \mu\text{K}$, leaving the temperature of the 2.9×10^4 Dy atoms essentially unchanged. For carrying out the measurements in the high-field region, we then quickly (within 12 ms) ramped up the magnetic field to the variable target field, where (partial) thermalization took place. After a hold time of 50 ms, the magnetic field was quickly (within 1 ms) ramped to 235.4 G. At this field, chosen for thermometry, the interspecies interaction is very weak and the sample expands ballistically after release from the trap. Temperatures were measured by standard time-of-flight imaging.

The thermalization scan reveals a scenario dominated by three broad Feshbach resonances, at the centers of which very fast interspecies heat exchange occurs and the temperatures become nearly equal. The corresponding positions are located near 200, 217, and 253 G (see solid arrows in Fig. 5.6). While the first resonance (near 200 G) is quite strong and has considerable overlap with the 217-G resonance (second resonance), the third resonance (near 253 G) is clearly weaker and well separated from the two other ones. Further, much narrower resonances exist (dashed arrows), with negligible effect on the overall scenario. The resonance near 217 G is the strongest one and thus the feature of main interest in our present work.

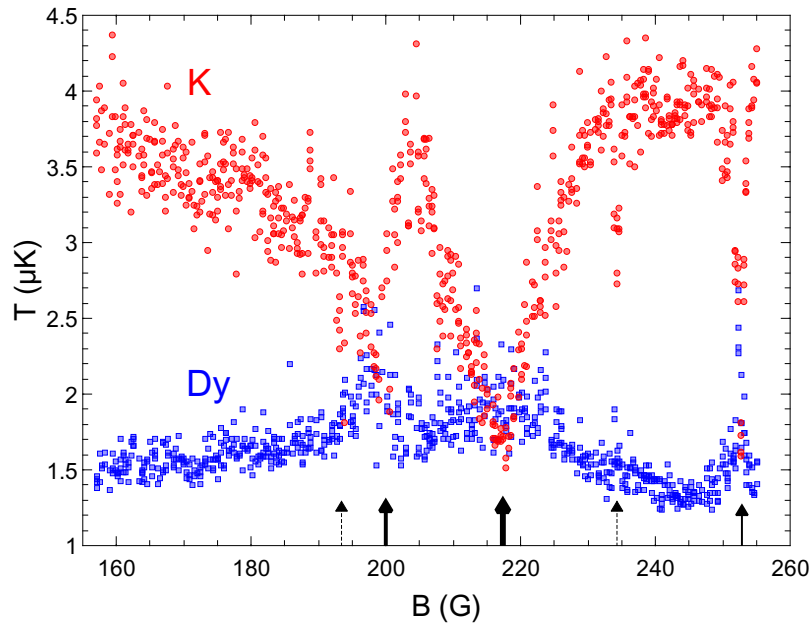


Figure 5.6: Thermalization scan revealing magnetic-field dependent resonances in interspecies elastic scattering. The mixture is initially prepared in a non-equilibrium situation, where the ^{161}Dy component ($1.3\ \mu\text{K}$) is much colder than the ^{40}K component ($4\ \mu\text{K}$). Within a short hold time of 50 ms, interspecies thermalization is observed. Fast thermalization is found to reach essentially equal temperatures at three points (solid arrows), which reveals the existence of three relatively broad Feshbach resonances. Indications of further, much narrower resonances are observed as well (two examples marked by dashed arrows). The broadest resonance, centered near 217 G is the one of main interest for the creation of strongly interacting Fermi-Fermi systems.

Model of three overlapping resonances

The magnetic-field dependence of the scattering length in a scenario of overlapping Feshbach resonances, assuming a constant background a_{bg} , can be represented by the product formula [218, 219]

$$a(B) = a_{\text{bg}} \prod_{i=1}^n \frac{B - c_i}{B - p_i}, \quad (5.2)$$

where the parameters p_i and c_i denote the positions of the poles and zero crossings, respectively. A straightforward transformation gives the equivalent sum formula [219]

$$a(B) = a_{\text{bg}} \left(1 - \sum_{i=1}^n \frac{\delta_i}{B - p_i} \right) \quad (5.3)$$

with

$$\delta_i = (c_i - p_i) \prod_{j \neq i}^n \frac{c_j - p_i}{p_j - p_i}. \quad (5.4)$$

A practical advantage of the product formula is that it explicitly contains the positions c_i of the zero crossings, which are often good observables in an experiment [220, 221]. An advantage of the sum formula is that the parameters δ_i provide a measure for the relative strengths of the different resonance contributions. In the case of a single, isolated resonance $\delta_1 = c_1 - p_1$ corresponds to the common definition [50] of the Feshbach resonance width.

Determination of poles and zero crossings

The poles (zero crossings) associated with Feshbach resonances can be identified as points of fastest (slowest) thermalization in scans like the one shown in Fig. 5.6. We have carried out further scans with higher resolution in narrower magnetic field ranges near the resonance centers, and obtained values $p_1 = 200.1(2)$ G and $p_2 = 217.27(15)$ G for the poles of the two broadest resonances. Here, because of the fast thermalization, we used short hold times of 50 ms (15 ms) for the determination of p_1 (p_2).

For the observation of zero crossings, close to which thermalization is very slow, long hold times are favorable. In a scan with a hold time of 1.2 s, we determined the position $c_1 = 203.0(2)$ G for the zero crossing between the poles p_1 and p_2 .

The third resonance (near 253 G) is found in a region where the local background scattering length is very small. This is a consequence of the near cancellation of the the global background scattering length a_{bg} by the effect

of the two broad resonances. While the pole position p_3 can be determined in a straightforward way from the point of fastest thermalization, a determination of the two zero crossings c_2 and c_3 solely based on the observation of thermalization minima turns out to be rather inaccurate. We therefore investigated thermalization in a wide range covering c_2 , p_3 , and c_3 and analyzed the resulting data based on the model introduced in Ref. [193] and applied to our mixture in [202] (see also Sec. 5.7.1).

The model is based on the assumption of thermalization described by an exponential decrease of the temperature difference with increasing hold time, with a relaxation rate being proportional to the elastic scattering cross section and thus being proportional to $a^2(B)$. The temperature difference $\Delta T = T_K - T_{Dy}$ can then be written as a function of the magnetic field strength,

$$\Delta T(B) = \Delta T_0 \exp[-Ca^2(B)], \quad (5.5)$$

where ΔT_0 is the initial temperature difference. The parameter C is proportional to the hold time and further determined by a combination of the experimental parameters, as described in Refs. [193, 202].

The measurements in Fig. 5.7 were taken in a wide range between 229 and 275 G under similar initial conditions as in Fig. 5.6, but with a much longer hold time of 1.2 s. Thermometry was performed in the same way as in Fig. 5.6. We fitted the data based on the thermalization model [Eq. (5.5)] and the product formula [Eq. (5.2)] for $a(B)$. The parameters p_1 , p_2 , and c_1 were fixed to their separately determined values (see above discussion). The fit (solid curve in Fig. 5.7) yielded the parameter values $p_3 = 252.79(8)$ G, $c_2 = 243.4(4)$ G, and $c_3 = 257.5(4)$ G.

The complete set of resonance parameters p_i and c_i for our three-resonance model is summarized in Table 5.1. Based on Eq. (5.4), we also calculated the parameters δ_i , which characterize the strengths of the resonances. The resulting values (last column) confirm that the second resonance is the strongest one. The first resonance is about three times weaker, and the third resonance is about 20 times weaker than the strongest one.

Background scattering length

Having determined the poles and zero crossings describing our three-resonance scenario, the remaining task is to determine the background scattering length a_{bg} , which is left as the only unknown quantity in Eqs. (5.2) and (5.3). For this purpose, we carried out thermalization measurements in a similar way as described in Ref. [202]. We selected magnetic field regions, where thermalization takes place on experimentally convenient timescales

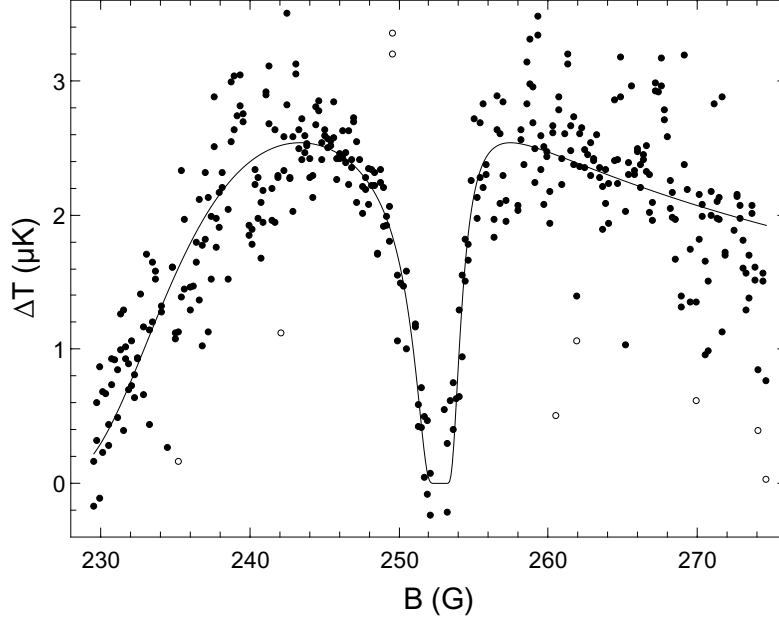


Figure 5.7: Thermalization scan in the region of the third resonance. The temperature difference ΔT was measured for a long hold time of 1.2 s. The solid line represents a fit based on the thermalization model described in the text, from which we obtain the pole position (minimum of ΔT) and the positions of the two neighboring zero crossings (maxima). Note that we have applied a rejection algorithm based on repeated application of Chauvenet’s criterion [222] to reduce the effect of outliers and barely resolved narrow Feshbach on the fit. This removed 17 data points (open symbols) of in total 393 data points and resulted in a very robust parameter values.

Table 5.1: Parameters characterizing the scenario of three overlapping resonances. The given 1σ uncertainties include the fit errors and estimates for model-dependent errors. Additional magnetic-field uncertainties from the calibration and from day-to-day fluctuations are estimated on the order of 0.1 G.

i	p_i (G)	c_i (G)	δ_i (G)
1	200.1(2)	203.0(2)	7.9(7)
2	217.27(15)	243.4(4)	24.6(6)
3	252.79(8)	257.5(4)	1.2(1)

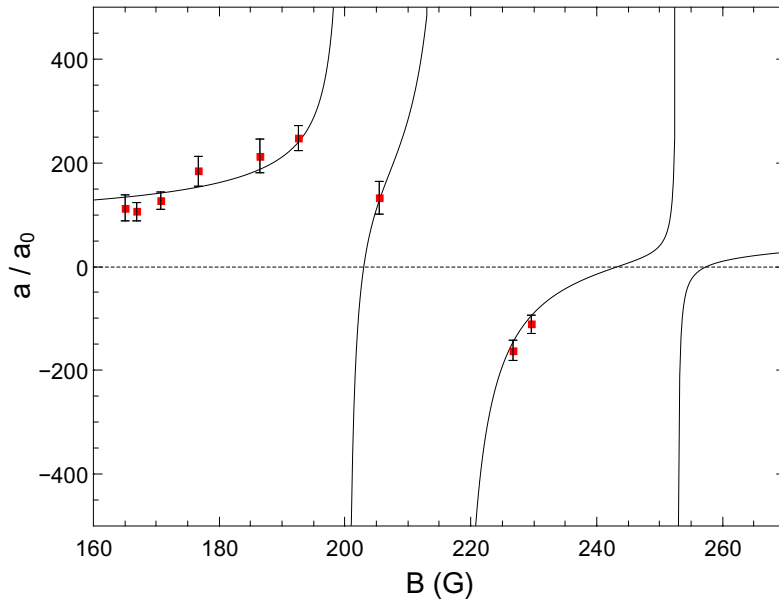


Figure 5.8: Magnetic-field dependence of the scattering length in the range of interest. The solid lines represent our model of three overlapping Feshbach resonances, with all parameters being determined experimentally. The experimental data points result from measurements of the scattering cross section by interspecies thermalization.

and which are free of narrow Feshbach resonances, and determined the absolute values $|a(B)|$ of the scattering length for nine different values of the magnetic field strength. The corresponding signs uniquely follow from our three-resonance model. In this way, we obtained the nine measured values shown in Fig. 5.8. We finally fitted Eq. (5.2) to these data points with a_{bg} being the only free parameter. This yields the value of $a_{\text{bg}} = +59(3) a_0$, where the given uncertainty includes the fit error and the effect of the uncertainties in the resonance parameters p_i and c_i .

We estimate that systematic uncertainties in the experimental parameters (mainly uncertainties in the atom numbers and trap frequencies) and model-dependent errors result in an additional relative uncertainty of 15%, which dominates the error budget. Therefore, our final result for the background scattering length in the 200-G region is $a_{\text{bg}} = +59(9) a_0$. It is interesting to note that our previous measurement [202], which was carried out at a low magnetic field of 430 mG, gave essentially the same value ($|a_{\text{bg}}| \approx 60 a_0$), although the background scattering length may slowly vary with the magnetic field.

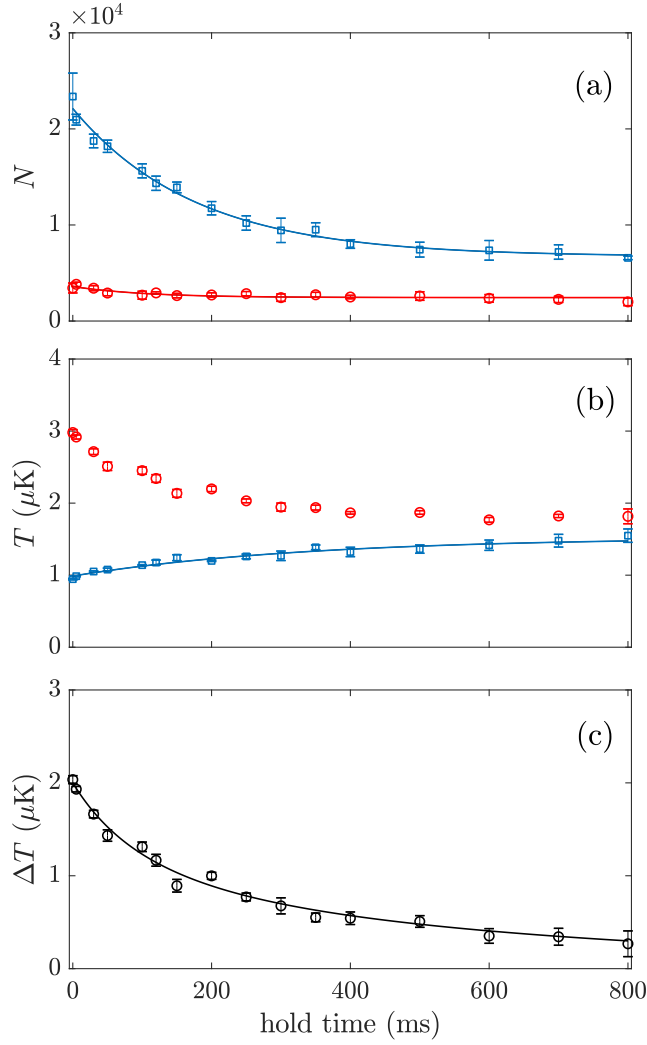


Figure 5.9: Example for cross-species thermalization ($B = 229.5 \text{ G}$) and the fit analysis to extract a value for $|a|$. (a) Observed time evolution of the atom numbers N_{Dy} (blue open squares) and N_{K} (red open circles) together with fits by simple exponential functions with a constant offset. (b) Time evolution of the temperatures T_{Dy} and T_{K} ; the increasing Dy temperature is again fitted by a simple heuristic model function. (c) Evolution of the temperature difference $\Delta T = T_{\text{K}} - T_{\text{Dy}}$ with a numerical fit based on Eq. (5.6).

Analysis of thermalization measurements

The basic idea of our cross-species thermalization measurements to determine the Dy-K elastic scattering cross section (see example in Fig. 5.9) is the same as reported in [202], but here we have to deal with the additional complication that strong Dy losses occur during the thermalization process.

Our model was originally introduced in [193] and can be expressed in terms of a differential equation for the temperature difference $\Delta T = T_K - T_{\text{Dy}}$,

$$\frac{d}{dt}\Delta T = -\sigma_{\text{el}}^2 \frac{\xi q}{3\pi^2} \frac{m_{\text{Dy}}\bar{\omega}_{\text{Dy}}^3}{k_{\text{B}}T_{\text{Dy}}}(N_{\text{Dy}} + N_{\text{K}})\Delta T, \quad (5.6)$$

where $\sigma_{\text{el}} = 4\pi a^2$ is the cross section for elastic Dy-K collisions and $\xi = 4m_{\text{Dy}}m_{\text{K}}/(m_{\text{Dy}} + m_{\text{K}})^2$ accounts for the effect of mass imbalance in the collisional energy transfer. The factor q depends on the ratio of polarizabilities, masses, and temperatures [202]. Under our experimental conditions, this factor can be well approximated by a constant $q = 1.45$.

A typical data set for the time evolution of the atom numbers N_{Dy} , N_{K} and the temperatures T_{Dy} , T_{K} is shown in Fig. 5.9(a) and (b). As a first step in the analysis, we independently fit the observed decay of N_{Dy} , the slow decrease of N_{K} , and the increase in T_{Dy} with simple exponential model functions, which we generally find to describe the data well. As a second step, we fit a numerical solution of Eq. (5.6) to the decreasing temperature difference ΔT , with the evolution of T_{Dy} and $N_{\text{Dy}} + N_{\text{K}}$ described by the fit functions obtained before. Figure 5.9(c) illustrates that the fit with the two free parameters σ_{el} and ΔT_0 matches the experimental data very well. For our specific example ($B = 229.5$ G, $\bar{\omega}_{\text{Dy}}/2\pi = 180$ Hz), we obtain a best estimate for σ_{el} corresponding to $|a| = 87 a_0$.

217-G resonance: Strength and universal range

For the experiments described in the main text, we are mainly interested in the interspecies scattering length near the pole of the 217-G resonance. Here, the scattering length can be well approximated by

$$a(B) = -\frac{A}{B - B_0} a_0, \quad (5.7)$$

where $B_0 = p_2 = 217.27(15)$ G and $A = \delta_2 a_{\text{bg}}/a_0 = +1450(230)$ G.

For discussing the character of this Feshbach resonance in terms of entrance-channel or closed-channel dominated behavior [50], it is useful to introduce

a characteristic length as defined by the range parameter [223]

$$R^* = \frac{\hbar^2}{2m_r a_0 \delta\mu A}. \quad (5.8)$$

Here $m_r = 32.04$ a.m.u. is the reduced mass and $\delta\mu$ the (unknown) differential magnetic moment. The universal range of a Feshbach resonance is reached if $|a| \gg R^*$, which also represents a necessary condition for a strong Pauli suppression of few-body losses [78].

The properties of the molecular states underlying our Feshbach resonances are currently unknown and require further in-depth investigation. For now, to get an idea of the universal range, we use a conservative guess for the differential magnetic moment $\delta\mu = 0.1 \mu_B$, where μ_B is Bohr's magneton. This yields $R^* \approx 300 a_0$ as a conservative estimate for the range parameter. We thus conclude that the universality condition $|a| \gg R^*$ is rather easy to fulfill near the pole of our 217-G Feshbach resonance. We note that also the many-body condition $k_F R^* \ll 1$ for universality in a fermionic system (Fermi wave number k_F) is well fulfilled under realistic conditions.

5.7.2 Decay

Overview of losses in the resonance region

The loss scan in Fig. 5.10 presents an overview of the complex magnetic-field dependence of losses in the region of the 217-G resonance. Here the number of Dy and K atoms was recorded after a hold time of 150 ms in the trap at a constant magnetic field. Interspecies losses show up as correlated features in the loss spectra of both species.

A broad loss feature appears for both species about 0.5 G below the resonance center, where we estimate a scattering length of roughly $+3000 a_0$. This feature resembles observations made in spin mixtures of ${}^6\text{Li}$ [175, 206, 207] and ${}^{40}\text{K}$ [82] and indicates the formation of weakly bound dimers, which after secondary collisions decay to deeply bound molecular states. The fact that such losses appear not at the center of the resonance, but on the side with large positive scattering length, is intrinsic to two-component fermion systems near broad Feshbach resonances with strong Pauli suppression of inelastic few-body processes.

The loss spectrum also reveals several narrow interspecies features. Some of them appear as resolved resonances, but other structures rather resemble a fluctuating background. In between features of increased losses, good regions can be identified where the lifetime exceeds 100 ms. Besides interspecies losses, we have observed intraspecies losses for Dy. This can be seen from

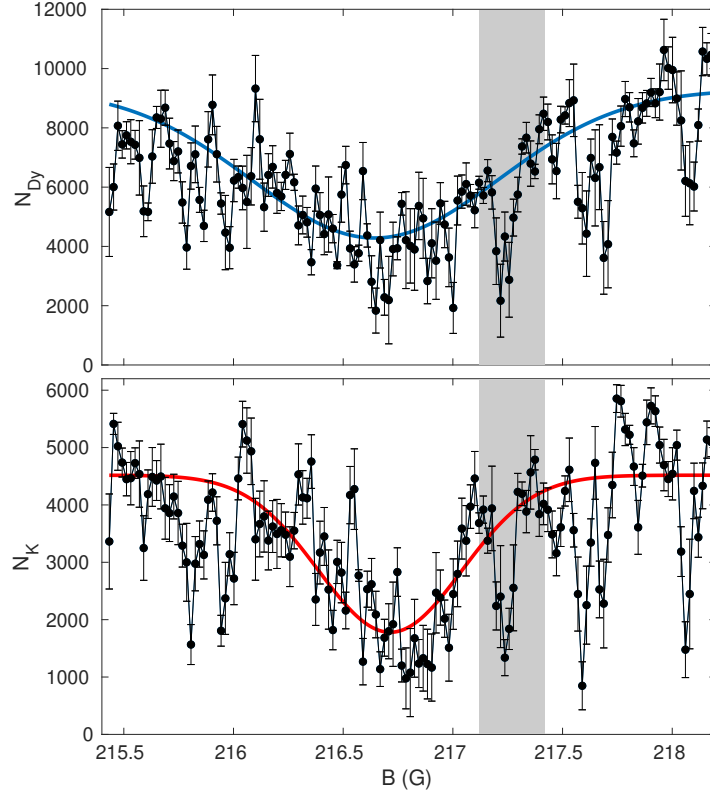


Figure 5.10: Loss scan in the resonance region. The plots show the number of Dy atoms (upper panel) and K atoms (lower panel) left in the trap ($\bar{\omega}_{\text{Dy}} = 2\pi \times 130 \text{ Hz}$) after a hold time of 150 ms at a fixed magnetic field. The initial atom numbers are $N_{\text{Dy}} = 24000$ and $N_{\text{K}} = 6000$, and the initial temperature is $T = 500 \text{ nK}$. The solid lines are Gaussian fits to the broad loss feature, excluding narrow loss features. The shaded region indicates the 1σ -uncertainty in our knowledge of the pole position of the strong 217-G resonance.

the background atom number ($N_{\text{Dy}} \approx 9500$) in Fig. 5.10, which is a factor of 2.5 below the initial atom number. These Dy losses generally show a fluctuating background behavior, as observed in [48].

From the timescale of losses (on the order of 100 ms), we conclude that recombination processes are no problem for experiments on short time scales (typically below 10 ms), such as the hydrodynamic expansion studied in the main text. For experiments on longer timescales, however, it may be important to choose good spots, where both intraspecies and Dy interspecies losses are minimized. The data of Fig. 5 in the main text were recorded on such a spot at 217.5 G.

Model for fitting decay curves

For extracting three-body rate coefficients from atom number decay curves, one has to take into account the heating of the sample [224]. Our simple model to avoid this complication is based on the initial behavior near $t = 0$, which can be characterized by the initial number $N_0 = N(t = 0)$ and the initial decay rate $1/\tau = -\dot{N}(0)/N(0)$. To extract optimum values for these parameters from a fit to the observed decay, we follow a heuristic approach based on the differential equation

$$\frac{\dot{N}}{N_0} = -\frac{1}{\tau} \left(\frac{N}{N_0} \right)^\alpha, \quad (5.9)$$

where the phenomenological exponent α is a fit parameter, which absorbs possible heating and other effects. We find that the solution

$$N(t) = \frac{N_0}{\alpha^{-1}\sqrt{1 + (\alpha - 1)t/\tau}} \quad (5.10)$$

fits our loss curves for all single- and mixed-species cases very well and is thus applied to all cases discussed in the present work. The calculation of rate coefficients is then based on the values for the fit parameters N_0 and τ .

Decay of K in the mixture

Here we analyze losses of K observed in the Dy-K mixture in terms of three-body processes and extract upper limits for the corresponding rate coefficients. Three-body decay of K alone is known to be very weak and can be neglected here.

We first assume that losses are caused by processes involving one K and two Dy atoms. This leads to the loss equation

$$\dot{N}_{\text{K}} = -K' \int d^3r n_{\text{K}} n_{\text{Dy}}^2. \quad (5.11)$$

We approximate the number density distributions n_i ($i = \text{K}, \text{Dy}$) in the harmonic trap (mean frequencies $\bar{\omega}_i$) by thermal Gaussian distributions with spatial widths $\sigma_i = \bar{\omega}_i^{-1} \sqrt{k_B T / m_i}$. After integration we obtain

$$\frac{\dot{N}_{\text{K}}}{N_{\text{K}}} = -K' N_{\text{Dy}}^2 \left(\frac{\sigma'}{2\pi\sigma_{\text{K}}\sigma_{\text{Dy}}^2} \right)^3, \quad (5.12)$$

where $\sigma' = (\sigma_{\text{K}}^{-2} + 2\sigma_{\text{Dy}}^{-2})^{-1/2}$.

In an analogous way, we now assume that losses are caused by processes involving two K atoms and one Dy atom (two K atoms lost per event). This leads to the loss equation

$$\dot{N}_{\text{K}} = -2K'' \int d^3r n_{\text{K}}^2 n_{\text{Dy}}, \quad (5.13)$$

which after integration simplifies to

$$\frac{\dot{N}_{\text{K}}}{N_{\text{K}}} = -K'' N_{\text{K}} N_{\text{Dy}} \left(\frac{\sigma''}{2\pi\sigma_{\text{K}}^2\sigma_{\text{Dy}}} \right)^3, \quad (5.14)$$

where $\sigma'' = (2\sigma_{\text{K}}^{-2} + \sigma_{\text{Dy}}^{-2})^{-1/2}$.

To obtain values (upper limits) for the event rate coefficients, we analyze the decay curves displayed in Fig. 5(a) in the main text. By using the above fit model, we extract values for the initial K decay time $\tau = -N_{\text{K}}/\dot{N}_{\text{K}} = 350(150)$ ms, the initial K atom number $N_{\text{K}} = 3100(200)$, and the initial Dy atom number $N_{\text{Dy}} = 16\,700(400)$. From Eqs. (5.12) and (5.14) and the experimental parameters ($\omega_{\text{Dy}} = \omega_{\text{K}}/3.6 = 2\pi \times 130$ Hz, $T = 540$ nK) we finally obtain

$$\begin{aligned} K' &\approx 4 \times 10^{-25} \text{ cm}^6/\text{s} \\ K'' &\approx 3 \times 10^{-25} \text{ cm}^6/\text{s} \end{aligned} \quad (5.15)$$

as upper limits for the interspecies three-body event rate coefficients.

Decay of Dy

Here we analyze the observed Dy decay (data shown in Fig. 5 of the main text) under the assumption that these losses are caused by collisions of three Dy atoms. The corresponding loss equation reads

$$\dot{N}_{\text{Dy}} = -3K_3 \int d^3r n_{\text{Dy}}^3, \quad (5.16)$$

which after integration simplifies to

$$\frac{\dot{N}_{\text{Dy}}}{N_{\text{Dy}}} = -3K_3 N_{\text{Dy}}^2 \left(\frac{1}{2\pi\sqrt{3}\sigma_{\text{Dy}}^2} \right)^3. \quad (5.17)$$

From the fit to the Dy decay shown in Fig. 5(a) of the main text, we extract $\tau = 320(50)$ ms and $N_{\text{Dy}} = 16\,700(400)$ and obtain the value

$$K_3 = 3.4(5) \times 10^{-25} \text{ cm}^6/\text{s}$$

for the event rate coefficient. Analyzing the data in Fig. 5(b) of the main text in the same way, with the fit yielding $\tau = 1000(150)$ ms and $N_{\text{Dy}} = 19\,700(400)$, we obtain the value

$$K_3 = 8.1(1.2) \times 10^{-26} \text{ cm}^6/\text{s}.$$

The fact that the former value (with K present) is about four times larger cannot be explained by three-body loss events involving K atoms, as their contribution is too weak. However, our data show that K atoms somehow catalyze Dy losses. The underlying mechanism is currently not understood.

5.7.3 Interaction-induced contraction

Here we introduce a model that describes the contraction of the mixture induced by the resonant interaction in the unitarity limit under the assumption of zero temperature. The results point to a possible mechanism how the presence of K atoms can enhance three-body losses in the Dy component.

Theoretical model

We calculate the number density distributions $n_{\text{Dy}}(r)$ and $n_{\text{K}}(r)$ of the trapped interacting species in the Thomas-Fermi limit, in which kinetic energy terms related to density variations can be neglected and the local density approximation can be applied. This also allows us to reduce the situation to a spherical trap; the solutions can then be scaled to the real, anisotropic trap.

The functional for the total energy can be written as

$$E = \int d^3r (U_{\text{Dy}}n_{\text{Dy}} + U_{\text{K}}n_{\text{K}} + \epsilon_{\text{Dy}} + \epsilon_{\text{K}} + \epsilon_{\text{int}}), \quad (5.18)$$

where $U_{\text{Dy}}(r) = \frac{1}{2}m_{\text{Dy}}\bar{\omega}_{\text{Dy}}^2r^2$ represents the Dy trap potential and

$$\epsilon_{\text{Dy}} = \frac{3}{10}(6\pi^2)^{2/3}\frac{\hbar^2}{m_{\text{Dy}}}n_{\text{Dy}}^{5/3} \quad (5.19)$$

denotes the kinetic energy density of Dy without interaction. For the K component, U_{K} and ϵ_{K} are defined analogously.

For the interaction energy density we use the approximation

$$\epsilon_{\text{int}} = -b \times \frac{3}{10} (6\pi^2)^{2/3} \frac{\hbar^2}{2m_r} \frac{n_{\text{Dy}} n_{\text{K}}}{(n_{\text{Dy}}^2 + n_{\text{K}}^2)^{1/6}}. \quad (5.20)$$

This expression was introduced in [32] to fit the equation of state of a non-superfluid mass-balanced system [225]. Remarkably, we noticed that the same expression also provides a very good fit to the equation of state for the imbalanced mixture with mass ratio 40/6, which was published in [138]. The only difference seems to be a slight difference in the optimum value of the prefactor b . While $b = 1.01$ provides an optimum fit for the mass-balanced case [32], we found the slightly higher value $b = 1.04$ for the mass-imbalanced (40/6) case. In the representation of Eq. (5.20), the interaction term seems to be nearly independent of the mass ratio. Therefore, we are confident that it can be readily applied also to our mass ratio of 161/40.

The number density distributions $n_{\text{Dy}}(r)$ and $n_{\text{K}}(r)$ are found by minimizing the energy functional. This is done by varying the densities with the gradient descent method under the constraint that the atom numbers N_{Dy} and N_{K} are fixed. We represent the densities on a spatial grid, of which the step size is below 10^{-3} of the typical Thomas-Fermi radius of the clouds. The number of iterations in the minimization algorithm guarantees a relative precision of 10^{-4} for number densities and derived quantities.

Density increase and loss enhancement

Figure 5.11 shows the effect of interaction for $N_{\text{K}}/N_{\text{Dy}} = 0.12$, which has been chosen to demonstrate that even a small fraction of K atoms can have a considerable effect. The interaction-induced contraction is clearly seen in profiles. The central Dy (K) density is increased by a factor of 1.64 (1.70). To quantify the total enhancement of three-body decay of Dy and K within the whole trap, we relate the total three-body decay rate to the case without interspecies interaction (Thomas-Fermi profile n_{TF}), and define the corresponding factors

$$\beta_i \equiv \frac{\int d^3r n_i^3(\mathbf{r})}{\int d^3r n_{\text{TF},i}^3(\mathbf{r})}, \quad (5.21)$$

where $i = \text{Dy}, \text{K}$. These factors can describe both the effect of attractive ($\beta > 1$) or repulsive ($\beta < 1$) interaction in the mixture, but here we focus on the case of the strong attraction on resonance. By numerical integration of the cubed density profiles of the two species we obtain $\beta_{\text{Dy}} = 2.07$ and $\beta_{\text{K}} = 2.85$. It is remarkable that the presence of a relatively small minority component of K can have such a large effect on the profile and thus three-body recombination rate of the majority component of Dy.

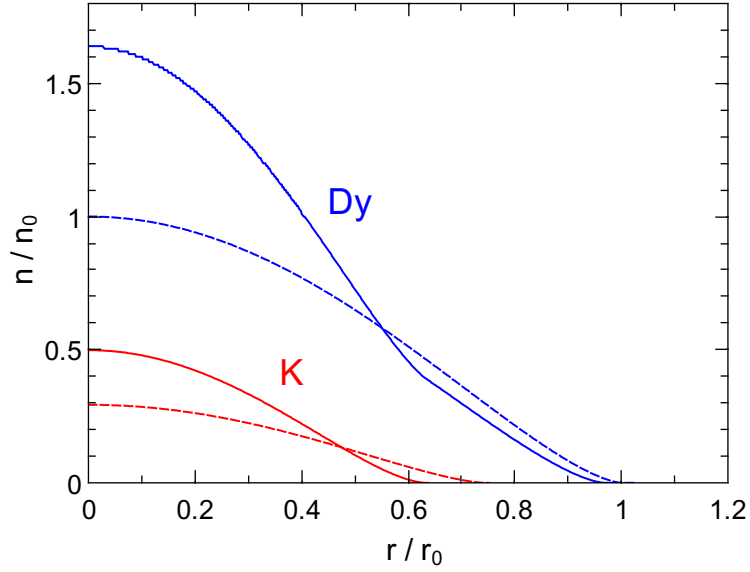


Figure 5.11: Radial density distributions for the Dy and K components, with (solid lines) and without (dashed lines) interaction for a number ratio $N_K/N_{\text{Dy}} = 0.12$. All profiles are normalized to the quantities r_0 and n_0 , which represent the Thomas-Fermi radius and the central density of the non-interacting Dy component, respectively.

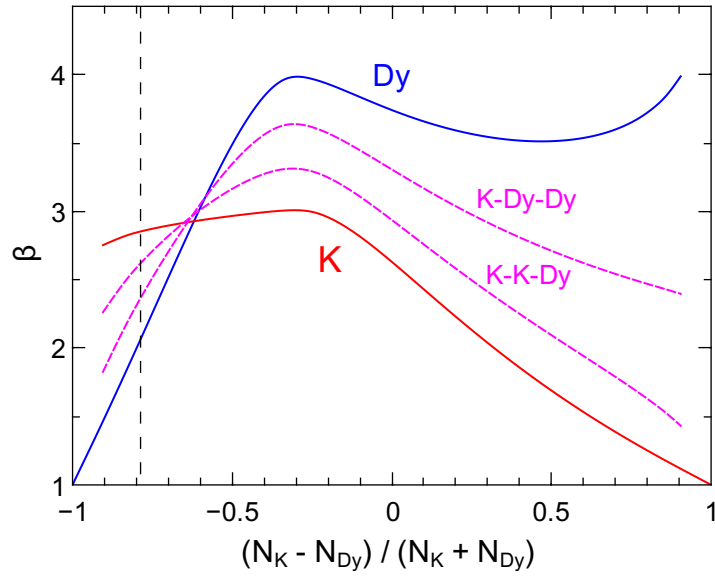


Figure 5.12: Enhancement factors for three-body recombination as a function of the global polarization. The solid curves refer to intraspecies three-body collisions of Dy and K, while the dashed curves refer to interspecies processes involving both atoms. The vertical dashed line corresponds to the situation shown in Fig. 5.11.

Within the assumptions of our model, the enhancement factor depends only on the atom number ratio N_K/N_{Dy} and the trap frequency ratio $\bar{\omega}_K/\bar{\omega}_{\text{Dy}}$. Since, in our experiments, the latter is fixed to a value of 3.6, we can draw universal curves for β_{Dy} and β_K as a function of the global polarization $(N_K - N_{\text{Dy}})/(N_K + N_{\text{Dy}})$; see Fig. 5.12. The solid line that represents the Dy case shows a maximum value of about $\beta_{\text{Dy}} = 4$ for a polarization of -0.7 ($N_K/N_{\text{Dy}} = 0.54$), which highlights the possible strength of the effect.

Appendix A

Experimental Setup

This Appendix describes the experimental setup used for the production of ultracold mixtures of Dy and K atoms. The Appendix is divided up into the following parts: Section A.1 gives a general overview of the design considerations for the DyK experiment. The next section A.2 covers the general vacuum chamber design philosophy, and details the individual chambers and the atomic sources. The initial cooling stages are explained in section A.3 to A.5. Sections A.6 to A.9 describe the numerous laser setups, section A.10 contains the coil assembly, and section A.11 explains the imaging and data analysis scheme.

A.1 Design Considerations

The design of a new ultracold atomic experiment does not only involve the immediate requirements, but also the tailoring for all future possible experiments and additions. This makes the initial planning phase a challenging task because one has to simultaneously take care to efficiently use the available space, create optimal optical access and isolate unwanted sources of heat, noise and electro-magnetic fields. This involves a lot of balancing between creating the most general setup without losing the necessary focus on specific goals. One has to decide on key parts of the setup that can be improved upon as compared to other experiments, while parts that have proven to work adequately can be directly implemented. Our decisions on which parts should be improved upon were taken by comparing the performance of existing technologies to the following list of requirements:

1. A two-species experiment where the main chamber has a size and geometry that is comparable to a single species setup, both from a

vacuum and an optics point of view.

2. Single species loading performance should be on-par with state-of-the-art setups.
3. The magnetic response of all materials should be as low as possible, especially close to the main chamber.
4. All laser setups and frequency locks should be easy to operate, and highly reliable.
5. The Feshbach coil has to be able to produce homogeneous magnetic fields up to a strength of about 300 G.

Requirement 1 and 2 are essential when building an experiment that can also be successful when operating in a single-species mode. Number 3 is very important if one wants to work with the fermionic isotope of Dy. Because of the extreme density of Feshbach resonances it is very beneficial to have a setup that creates a passively stable background magnetic field. Requirement number 4 ensures reliable continuous operation of a double-species experiment, because adding a second species usually means doubling the number of lasers in the experiment, and all these have to be working at the same time. Requirement 5 is chosen to have a good chance of finding a suitable inter-species Feshbach resonance, based on the typical Feshbach resonance density[50] for alkali-metals (1 strong resonance per 1000 G) and a simple reduced mass scaling.

A.2 Vacuum Chambers

In cold-atom experiments the particles are cooled down by many orders of magnitude as compared to the surrounding room temperature walls. This is only possible if the cloud is sufficiently well isolated from the environment, in our case by an ultra-high vacuum (UHV). Achieving UHV involves a careful design of the vacuum vessel, rigorous leak testing and finally a thorough bake-out. The vacuum setup, shown in Fig. A.1, comprises three chambers separated from each other by gate valves and differential pumping tubes, there is a main chamber and two oven chambers. All steel parts utilize 316 series steel, to have an as low as possible magnetic permeability (μ_r). All other parts were either chosen to have an out-of-the-box low μ_r or got custom modifications by the manufacturers. All valves are of an all-metal design, allowing prolonged high-temperature bake-outs. The full setup is shown in Fig. A.1, where the three separate chambers all have a different color.

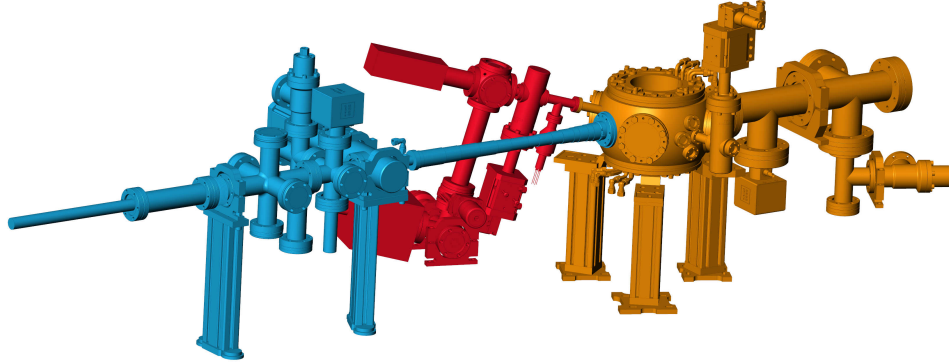


Figure A.1: CAD (computer aided design) rendering of the vacuum setup, with in blue the dysprosium oven chamber and Zeeman slower (ZS), in red the potassium 2D-MOT (2-dimensional magneto-optic trap) and in orange the main chamber.

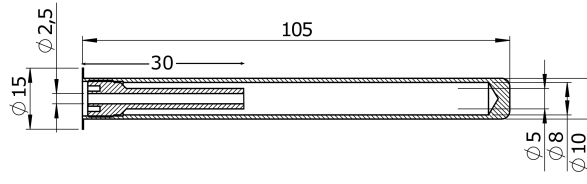


Figure A.2: Engineering drawing of the custom-designed crucible made out of tantalum used to create a collimated Dy beam. The front part, on the left hand side, can be heated independently to a higher temperature to prevent Dy accumulating in the collimation tube.

A.2.1 Dy Oven Chamber

Bulk dysprosium has a very high melting point of 1407°C , and therefore a highly specialized oven has to be used. Fortunately, commercial options are available in the form of effusion ovens used for molecular beam epitaxy. The implementation of these ovens to produce an atomic beam suitable for laser cooling is straightforward, and only involves a custom crucible to collimate the atomic beam as much as possible. We use a high-temperature effusion oven with an independent hot lip temperature control, an integrated shutter and water cooling¹. The crucible can contain about 15 g of Dy and has a collimation tube with a diameter of 2.5 mm and a length of 30 mm, as shown in Fig A.2. The dual lip control of the oven means we can have a higher temperature at collimation the end of the crucible, this helps to avoid the

¹WEZ 40-10-22-K-HL-C-0-LxxxD36 from MBE-Komponenten

clogging up of the collimation tube with source material. The whole oven is placed in a CF40 (ConFlat) tube with a flexible bellow that connects it to a CF40 6-way cross where we perform transverse cooling. After the transverse cooling cross, the atomic beam passes through an 10 mm diameter aperture that protects both the vacuum pump and gate valve, that are situated on the other side, from being coated with Dy. The vacuum pump is a combination of a non-evaporative getter (NEG) and a small ion pump², where the NEG has a pumping speed of 100 l/s for hydrogen and the ion pump 6 l/s (for Argon), and we typically have a pressure in the high 10^{-11} mbar range during oven operation. The pumping section of the chamber attaches to the Zeeman slower tube via a custom low-magnetic CF40 all-metal gate valve³. The Zeeman slower features a differential pumping tube with a 5 mm diameter and a length of 70 mm, to isolate the vacuum in the main chamber and the Dy oven chamber. In addition to the vacuum pump there is also a UHV pressure gauge⁴, a set of viewports and an all-metal angle valve⁵ attached to this part of the vacuum chamber.

A.2.2 K 2D-MOT Chamber

The very low natural abundance of potassium-40 imposes the need to use enriched samples as a source material. Two different methods exist to create a sufficiently large flux of atoms even in a room temperature environment, one is to use a heated reservoir, and the other is to use a so-called dispenser where a current controls the temperature of a thermally activated chemical reaction between potassium-chloride and pure calcium leading to potassium atoms and calcium-chloride. Dispensers have the advantage that they are more flexible, as one can have multiple different enrichment grades in different dispensers, and it is faster to adjust the atomic flux via a current instead of heating up the vacuum setup. For these reasons we chose to use enriched dispensers in our experiment. The setup contains three dispensers, each placed in one of the corners of a large ($58 \times 58 \times 158$ mm) anti-reflection coated glass cell⁶. The chamber, as shown in Fig. A.3, has a 20 l/s ion pump⁷, which is more suitable for the higher gas loads in an alkali-metal oven chamber. There is a gate valve in between the pump and the glass cell to be able to either bake or exchange the ion pump once too much potassium has been deposited inside the pump.

²SAES NEXTOrr D 100-5

³VAT 48132-CE44-X

⁴Agilent UHV-24P

⁵VAT 57132-GE02-0005

⁶JapanCell

⁷Agilent Star Cell

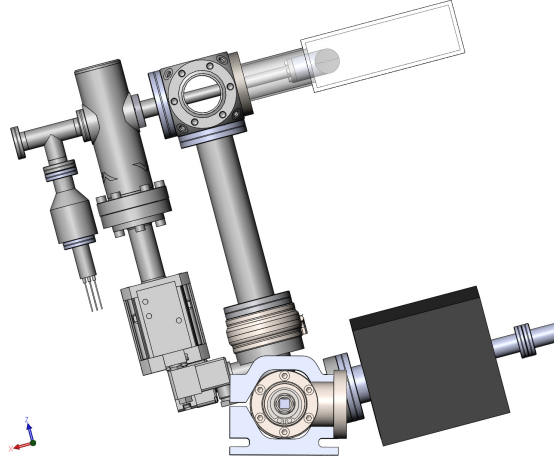


Figure A.3: CAD rendering of the 2D MOT vacuum chamber, shown are the glass cell in the top right corner, the ion pump on the bottom right and the differential pumping tube connecting this chamber to the main chamber.

A.2.3 Main Chamber

When starting a new experiment one has to make the crucial decision what type of main chamber to use. The two options are either a glass cell or a metallic chamber. The advantages of a glass cell are numerous, being that it has better optical access, is non-conducting and non-magnetic, and does not outgas hydrogen. Metallic chambers on the other hand are much more flexible in the number of ports connected to them and the type of windows and coatings. Metallic chambers do suffer from eddy currents when performing magnetic field changes. And depending on the type of metal used, could show some remanent magnetization response. Because our experiment, being a mixture, requires at least three flanges connected to the main chamber, mounting a glass cell would have been a very demanding task, especially with the very large temperature range involved while baking a vacuum apparatus. We therefore decided that we would use a metallic vessel as the main experimental vacuum chamber. Many metals and alloys are suitable construction materials for ultra-high vacuum vessels, but three are the most common: steel, titanium and recently aluminium became available. For our experiment we want to be able to have fast magnetic field changes, and ideally have a non-magnetic material. While both titanium and aluminium are non-magnetic they both have a higher conductivity than steel. Some special types of steel are made to be non-magnetic in their original casting (for example 304 types), and are even able to withstand machining and welding without turning ferromagnetic (like 316 types). These types of

steel are ubiquitous for vacuum technologies and a wide variety of companies offer an extremely versatile range of vacuum equipment. In Fig. A.4 the full vacuum setup including the main chamber is shown. The main chamber is a modified version of a standard spherical octagon⁸. The modifications are a CF63 nipple on one side to increase the effective pumping speed inside the main chamber, a CF16 nipple to connect to the 2D MOT chamber and one CF40 nipple for a larger clear aperture viewport. The standard remaining ports are: two CF160 on the top and bottom, 4 CF63, 1 CF40 and 7 CF16. The only pump in the main chamber is also a combination between a small ion pump and a NEG⁹, but here the NEG has a 5 times larger pumping speed. The pressure is monitored rather far away from the main chamber by an ion-gauge¹⁰. At the far end of this chamber we mounted an aluminium mirror inside a CF63 tee to reflect the Zeeman slower light (see Sec. A.4) into the Dy oven chamber without the risk of coating a viewport with dysprosium. There is a CF16 gate valve attached to one side of the main chamber that can be used to attach a science cell in the future, but features a viewport for now.

A.2.4 Viewports

Connected to the main chamber are a large number of anti-reflection (AR) coated viewports, that allow all the different wavelengths to reach the atoms without disturbing reflections and with a high transmission. All viewports are custom made to fit the multi-CF standard of our main chamber, which has a larger inner-diameter and smaller outer-diameter as compared to the standard CF sizes, and are manufactured by the special techniques group from the Culham Centre for Fusion Energy. All viewports are non-magnetic and allow for large bake-out temperatures, only limited to 250°C by the coatings. The two inverted CF160 viewports re-enter the chamber by 34 mm and feature a 64 mm diameter window, that is AR coated for 421, 532, 600-800 and 1064 nm. The four large CF63 viewports, plus the four CF16 viewports out of the horizontal plane, and the CF63 ZS viewport are all anti-reflection coated for 421 nm and 600-800 nm. The three CF16 and the CF40 viewports are coated for 532 nm, 1064 nm and 1550 nm, and the window is made out of sapphire in a titanium flange. Sapphire and titanium have a similar thermal expansion coefficient and therefore the clear aperture can be much larger as compared to our other viewports made out of steel and fused-silica. Larger clear apertures make the CF16 viewports much more versatile, and allow for tightly focused beams in the main chamber. All substrates and coatings are made by Laseroptik.

⁸Kimball physics MCF800-G2E5C2A8

⁹SAES NEXTorr D 500-5

¹⁰Agilent UHV-24P

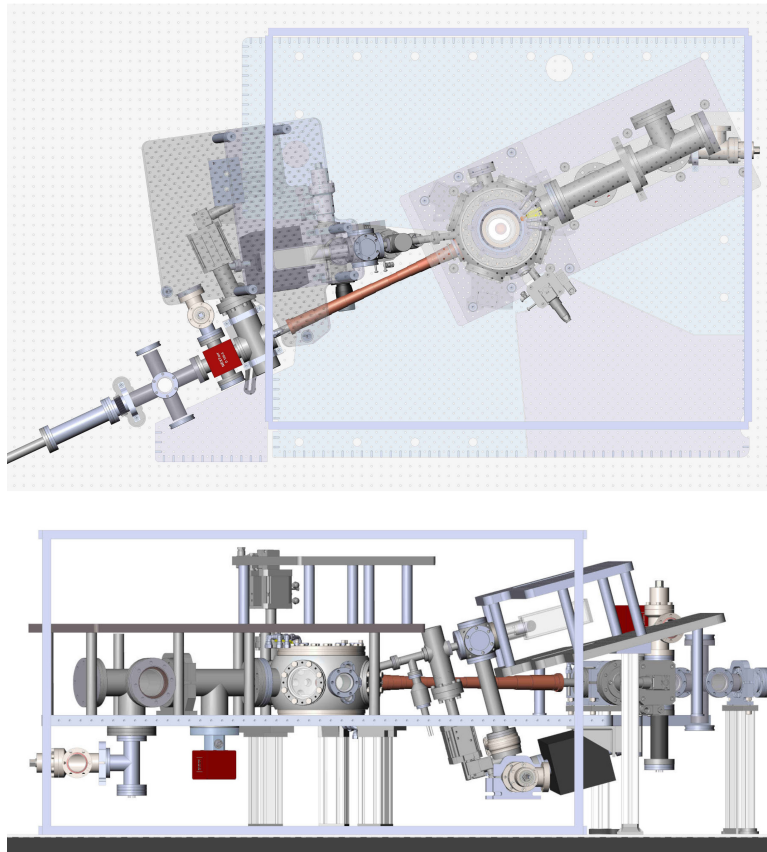


Figure A.4: Two different CAD renderings of the vacuum apparatus, one from above (top), and one from the side (lower). The rendering includes all breadboards and coils.

A.3 Dy Transverse Cooling

For species with a high melting temperature it is difficult to create a well-collimated atomic beam. Transverse cooling can aid the collimation significantly when performed close to the oven aperture, this also limits the divergence of the atomic beam in the final stage of the axial cooling. The result is a high-brightness beam cold beam in the 3D MOT capture volume. Our transverse cooling setup contains two retro-reflected highly elongated beams detuned by $\Gamma/2$ to the red side of the strong 421 nm transition of dysprosium. The non-gaussian beams are created by so-called laser-line generators that turn an incoming gaussian beam into a 1D outfanning beam with a fixed angle and a flat intensity profile along the fanning direction. This beam is then collimated using a cylindrical lens to get a size of 26 mm along the atomic beam and a waist of 2 mm in the other direction. The beams enter the vacuum directly after the effusion oven through AR coated CF40 viewports on a six-way cross. The polarization of the light is linear and we have a power of about 25 mW per beam.

A.4 Dy Zeeman Slower

To reach quantum degeneracy with cold atoms it is essential to have good vacuum conditions and high atom numbers. This usually excludes loading the MOT from a background gas, and therefore a pre-cooling stage is needed. Two different proven pre-cooling methods exist, and we utilize both in our experiment, one for each species. The so-called Zeeman slower (ZS) is a very good pre-cooling method for Dy and other high-melting point metals. A high-melting point makes it impossible to remove Dy atoms from any surface, like it is usually required for other MOT loading methods. The working principle of a ZS is as follows, a counter-propagating laser is used to cool the atoms down, but because it only contains a single frequency the light would quickly become off-resonant. The continuous slowing and cooling of the atoms is achieved by tuning the magnetic field orientated along the atomic beam axis in such a way that the induced Zeeman shift continuously compensates the decreasing Doppler shift. If the magnetic field profile follows a spatial square-root with an offset the atoms experience a constant deceleration (a_{ZS}), and depending on the choice of the detuning of the light the slower is either called an increasing, decreasing or spin-flip ZS.

Our ZS is based on the design for the Er experiment in Innsbruck [226], with a few minor adjustments. It consists out of four independent coils, an initial coil, profile coil, end coil and offset coil. This makes the slower flexible in its day-to-day use and enables adjustments to its performance.

The total combined length of the coils are 0.45 m, and the maximum capture velocity is set to $v_{\text{capt}} = 450$ m/s while the final velocity is designed to be $v_{\text{final}} = 7$ m/s. The first coil mainly defines the capture velocity, and the end coil can be used to adjust the exit velocity of the atoms. The layers of the profile coil can be addressed independently, but we did not implement this in our experiment because the measured field matched the simulated field almost exactly and therefore no adjustments of the individual currents were needed. The detuning of the slowing light, $\Delta = (\omega_{\text{light}} - \omega_0)$, is set to $-20\Gamma_{421}$, which is a nice middle ground between having the lowest influence on the narrow-line MOT and realistic shifting inefficiencies of AOMs. The combination of these choices already fully defines the required magnetic field given by

$$B(z) = B_{\text{offset}} + B_0 \sqrt{1 - \frac{z}{z_{\text{max}}}}, \quad (\text{A.1})$$

where $B_{\text{offset}} = 2\pi\hbar\delta/\mu_{\text{eff}}$ is the magnetic offset field with μ_{eff} being the differential magnetic moment between the excited state and the ground state ($\mu_{\text{eff}} = \mu_e - \mu_g \approx -1.06\mu_B$ for the Dy 421 nm transition), $B_0 = \hbar k_{421} v_{\text{capt}}/\mu_{\text{eff}}$ is the initial field strength, and z_{max} is the ZS length and is given by $(v_{\text{capt}}^2 - v_{\text{final}}^2)/(2a_{\text{ZS}})$. Making a ZS is therefore all about creating a coil design that matches this ideal field as closely as possible. Especially large gradients should be avoided, because they can lead to atom loss if the magnetic field gradient is larger than the corresponding maximum deceleration force. The ratio of the deceleration (a_{ZS}) over the maximum deceleration (a_{max}) is usually quantified by the safety parameter

$$\eta(z) = \frac{(v_{\text{capt}}^2 - v_{\text{final}}^2)}{2a_{\text{ZS}}(z)} = \frac{\mu_{\text{eff}}^2 m_{\text{Dy}}^2}{\Gamma_{421} k_{421}^3 \hbar^3} (B_z(z) - B_0) \frac{\partial B_z(z)}{\partial z}. \quad (\text{A.2})$$

The overall η for our ZS is 0.38. The maximum possible η is given by saturation parameter, $s_0 = I/I_S$, of the slowing beam, $\eta_{\text{max}} = s_0/(1 + s_0)$. In order to have some safety margin in the lower intensity part of the beam and to account for slight variations in the coil winding position, η is typically chosen to be below 2/3. If η is chosen too small the atoms will diffuse too far out of the central region of the ZS during the slowing process and eventually will hit the walls of the ZS.

The coil is wound using rectangular double enameled copper wire¹¹ with a dimension of 2.5 by 0.8 mm, it is able to withstand a long bake-out at temperatures above 200 °C. The different layers of the coil are held together using a pre-pregnated glassfibre tape that hardens during bake-out. We use a matlab script based on a finite element method and Biot-Savart's law to optimize the coil geometry. The resulting magnetic field on the central axis is shown in Fig. A.5. The heat generated by the ZS is dissipated from

¹¹Isodraht Damid 200

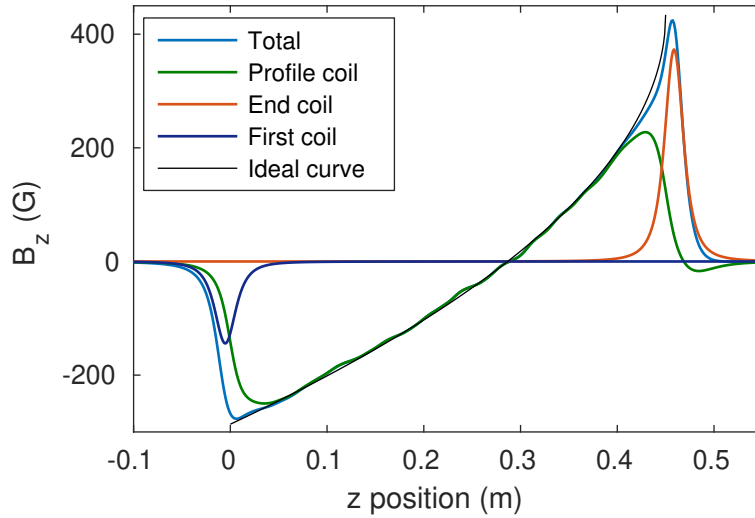


Figure A.5: Simulated magnetic field strength on the central axis of the ZS, with the Dy oven located on the left and the central MOT chamber on the right. Shown are the fields of the individual coils and of the field of the full ZS.

the inside by a water cooling loop consisting out a double walled tube with two barriers, one at 3 and one at 9 hours along almost the full length of the tube as is depicted in Fig. A.6. The inside tube has a conical expanding end connecting with the outer tube, and the barriers stop before the two tubes meet. This leaves a gap for the water to flow from the lower half of the tube to the upper half creating a water cooling path that has both the exit and entrance at the oven side of the ZS, as is shown in Fig. A.7. This design allows ZS coils to be placed much closer to the main chamber as would have been possible otherwise, which is highly desirable because the low final velocity of the ZS leads to a very large divergence of the atomic beam. The conical shape and the path of the water have a negative effect



Figure A.6: Photograph of the double walled structure of the ZS with the inner vacuum tube and the two barriers.

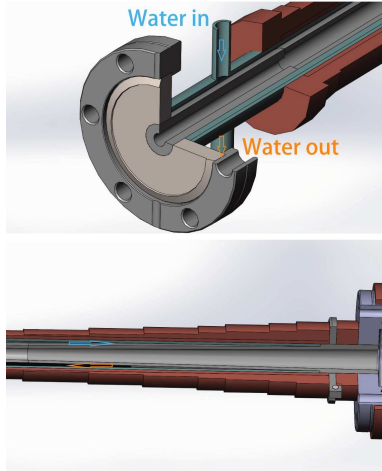


Figure A.7: CAD drawing of the ZS showing the water flow through the double walled pipe, and also the differential pumping tube at the input and the conical shape of the vacuum tube at the exit.

on the cooling capabilities at the main chamber side of the ZS. The final coil however, produces the the highest thermal load. This coil is not directly water cooled in our design, but instead has a good thermal contact with the profile coil via an aluminium spacer and thermal paste. All these measures combined enabled us to design a ZS where the final coil is in contact with the ZS flange while the outer diameter of the coil is sufficiently small to still be able to position and tighten the screws used to attach the ZS to the main chamber.

A.5 Potassium 2D MOT

This section briefly describes the pre-cooling setup for potassium, a more in-depth description can be found in Ref. [227]. The DyK experiment uses a two-dimensional magneto-optic trap (2D MOT) as a pre-cooling stage for potassium. This is both necessary to bridge the gap between the average velocity of thermal atoms and the capture velocity of the 3D MOT, and to ensure UHV conditions in the main chamber without a high potassium vapor pressure. A 2D MOT has two [228], for our experiment interesting, advantages over a Zeeman slower. The first one is the much more economic use of the source material since no atomic beam directed into the main chamber is required. The second advantage is that a full 2D MOT setup can be realized in a much more compact setup. The first point is indeed very advantageous when working with expensive enriched potassium-40 samples [166].

The working principle of a 2D MOT is comparable to a 3D MOT, the former

however can be fully optimized to achieve a high atomic flux output. Two pairs of coils create a quadrupole field in the transverse directions and as little as possible magnetic field in the axial direction. Two retro-reflected elliptical beams complete the setup in the transverse direction. As the name suggest cooling and trapping only happen in two directions, while atoms can travel freely in the third. We aid the creation of a directional cold atomic beam by using a so-called push beam, a single beam which pushes the atoms out of the 2D MOT in the direction of the main chamber. The two cooling beams are created with a pair of cylindrical lenses (50 and 200 mm) and a single short focal length negative lens (-9 mm). This creates very large elliptical beams with a $1/e^2$ size of 90 mm \times 22.5 mm, that then create a large capture volume and velocity. The beams are retro-reflected onto themselves with two pairs of metallic mirrors, to maintain the correct polarization of the light, placed at a right angle relative to each other to make a 1D corner cube reflector. The high-power laser light needed by these large beams is delivered to the setup by two polarization maintaining photonic crystal fibers¹², and the push-beam power is actively stabilized.

¹²NKT LMA-PM-15

The 2D quadrupole field is created by two pairs of coils. Each coil has 40 windings and all of them are placed in a home-made aluminium cage that surrounds the glass-cell but is mounted to the breadboard. We drive the coils with three independent powersupplies: a single x and y coil are linked together and the other two have their own powersupply. It is therefore possible to both tune the strength of the gradient and the location of the zero of the magnetic field. The coils produce a gradient of about 2.57 G/(A cm).

A.6 Dysprosium Laser Setup

Dysprosium, with its complicated electronic structure, exhibits many optical transitions [91]. This enables a very effective laser cooling and trapping scheme based on two different transitions, a broad one for slowing and a narrow transition for trapping. This combination enables a fast loading rate with a very low Doppler-temperature, and after pioneering experiments with ytterbium [229] and erbium [230] it is now very common for dysprosium experiments [105, 122].

A.6.1 Dy 421 nm Setup

The broadest Dy transitions has a wavelength of 421 nm and excites one of the S-shell electrons from 6S to 6P. This transition is nearly closed and it is very suitable for short periods of efficient laser cooling, first because of the broad natural linewidth of 32 MHz, and secondly because of the larger recoil of a blue photon. This transition is therefore ideally suited for transversal cooling, Zeeman slowing and absorption imaging, but less suited for a 3D MOT due to the very high Doppler temperature of about 770 μ K.

The implementation of this wavelength in our setup is designed to be highly flexible, allowing a free choice of the overall detuning of the laser, and therefore accessing all possible Dy isotopes. We achieve this freedom by frequency offset locking the main cooling laser to another reference laser. The reference laser then in turn is directly locked to the atomic transition of the most abundant boson, being dysprosium-164. The frequency shifting capabilities of this setup are not only used to switch between isotopes but also to generate resonant light at any desired magnetic field in order to perform absorption imaging.

The main laser is a commercial frequency doubled semiconductor laser¹³, where the infrared light is generated in a external-cavity diode laser (ECDL) and amplified by a tapered amplifier (TA) before it is frequency doubled in a bowtie cavity. The system can deliver up to 1.2 W of blue light, but in

¹³Toptica TA-SHG pro

our setup we run the laser at 600 mW output power.

The reference laser light is produced by a blue laser diode in an ECDL¹⁴, running at about 18 mW output power, which is enough to both perform spectroscopy and provide reference light for the main laser. The spectroscopy generates an error signal to which we lock the laser through frequency modulation transfer spectroscopy (FMTS), which provides a background free error signal with a large slope. The atomic gas used in the spectroscopy is generated in a custom see-through hollow cathode lamp (HCL) filled with 4 mBar of argon as a buffer gas. We found that the usual helium-neon buffer gas used in these lamps for dysprosium almost completely extinguishes the absorption signal on the 421 nm transition. We mix a small portion of both the reference and main laser on a 50/50 beamsplitter and detect the difference frequency, also called beat note, on a fast photodiode with a bandwidth of 7 GHz¹⁵. This difference frequency can now be used to create an offset lock by comparing it to an electronic reference frequency, we use a commercial solution to generate the error signal for the main laser lock¹⁶ which automatically switches between a frequency lock mode, for a large capture range, and phase lock mode, for a steep error signal.

In Fig.A.8 the distribution and frequency shifting of the blue laser setup is shown. The detuning of the main laser during the Dy MOT loading is at around 10Γ , which is in between resonance and our ZS light detuning. We generate both the TC and ZS light with single pass acousto-optic modulators (AOMs), therefore the relative detuning between the two cannot be changed but we are able to have much higher diffraction efficiencies when they are in a single pass configuration.

A.6.2 Dy 626 nm Setup

Dysprosium also has a fully closed transition with a natural linewidth of 136 kHz at 626 nm, this transition has a number of advantages over the broad 421 nm transition for a 3D MOT operation. Apart from the low Doppler temperature of about $3.2 \mu\text{K}$, a second advantage is that the sample is spin polarized after compressing the MOT [226], a feature that is especially appealing for magnetic lanthanide atoms because of dipolar relaxation.

We generate 626 nm light with a method pioneered for Be^+ in the Wineland group[231], we combine two commercial telecom wavelength lasers, one at 1050 nm and one at 1550 nm, through sum frequency generation (SFG) to

¹⁴Toptica DL pro

¹⁵Alphas UPD-50-SP

¹⁶Vescent D2-135

get a high-power and narrow linewidth output. SFG is performed in a single pass periodically poled lithium niobate (PPLN) crystal¹⁷, this setup is very robust and has a low complexity, as compared to for example a bi-chromatic cavity. Both infrared lasers are a combination between a pre-amplified seed laser and a fiber amplifier¹⁸, each delivering 5 W. The 1550 nm seed laser has a specified linewidth below 1 kHz, while the 1050 nm seed is below 10 kHz, both are already well below the natural linewidth of the intended transition without fast feedback schemes. This setup generates up to 1.8 W of 626 nm light.

Even though the transition is still detectable in the HCL, it is not strong enough to reliably lock the laser to. We therefore have an optical cavity acting as a frequency reference to which we lock the laser. The cavity is commercial¹⁹ and consists out of two mirrors separated by a 10 cm long spacer, which are all optically contacted and all are made out of ultra-low expansion (ULE) glass. The cavity is placed in three layers of thermally isolated and temperature stabilized enclosures. The inner most enclosure is under vacuum for added temperature, pressure and vibration isolation. ULE glass has the special property that it has a zero-crossing of the thermal expansion coefficient near room temperature, and therefore if one operates the cavity at this zero-crossing the length of the cavity is, to first order, decoupled to temperature fluctuations. The zero-crossing of our cavity has been measured by slowly heating it up and comparing two cavity modes to the atomic reference measured on the HCL. We obtained a zero-crossing temperature of 27.74(3) °C. We frequency shift the light used to lock the laser on one of the cavity modes with a fibered electro-optic modulator (EOM) by driving it with a sine-wave that has been turned into a sawtooth via a passive delay line called a non-linear transmission line (NLTL). This fully shifts the carrier to one of the sideband frequencies. We also use this EOM to modulate small sidebands at 25 MHz onto the carrier which are then used to create an error signal via a Pound-Drever-Hall scheme. We then close the feedback loop by acting back onto the piezo in the 1550 nm seed laser while the 1050 nm seed remains free running.

A.7 Potassium Laser Setup

A.7.1 K D2 setup

Potassium features, like all alkali-metals, a closed transition on the so-called D2 transition, which is for potassium from $4^2S_{1/2}$ to $4^2P_{3/2}$, and it has a wavelength of 766.7 nm. Even though this transition is fully closed, due

¹⁷Covesion

¹⁸NKT Photonics Koheras Boostik

¹⁹Stable Laser Systems

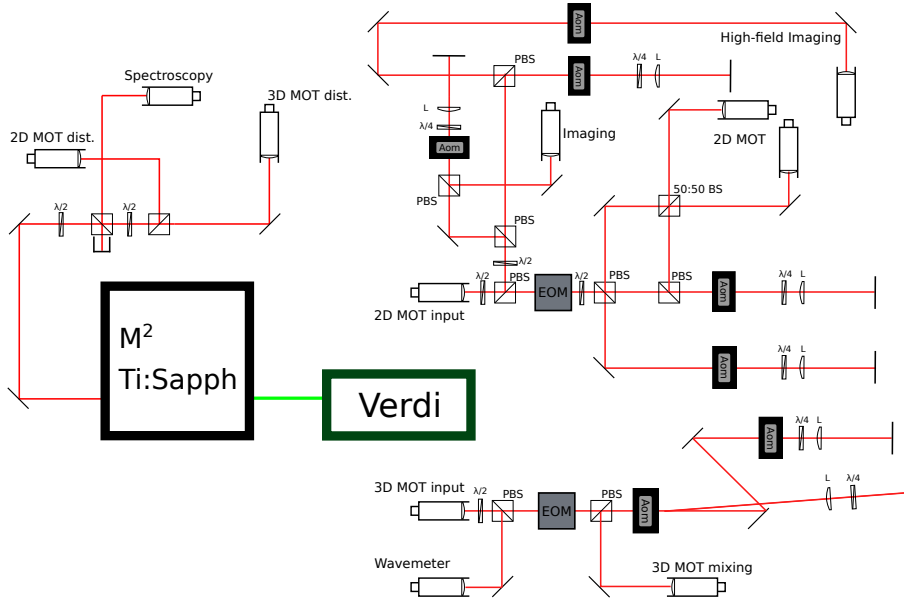


Figure A.9: Schematic drawing of the potassium D2 laser setup.

to the relative closely spaced excited state manifold, off-resonant excitation to a different hyperfine state is possible, and therefore a repumping beam is required returning the off-resonantly excited atoms back into the cooling cycle. For the fermionic isotope, ^{40}K , the difference between the pump and repump is rather large at a frequency of around 1.2 GHz, but most experiments still use a frequency shifting method to create the repumper frequency instead of building a second laser system. In our setup we use a free-space EOM to create sidebands on the carrier, one of which is used as a repumper since only very little repumper intensity is required. Up to 6.2 W of light at 766.7 nm is created with a Ti:Sapphire laser²⁰, optically pumped by an 18 W Diode-Pumped Solid State laser at 532 nm²¹, as can be seen in Fig. A.9. Unfortunately molecular oxygen features a transition close to this wavelength, and therefore we are required to purge the sealed Ti:Sapphire laser cavity about once a week with pure nitrogen. Most of the laser light is used for the 2D MOT because of our large glass cell, as explained in Sec.A.5, with around 1 W per fiber on the output. While for the 3D MOT we have around 250 mW on the atoms. We frequency stabilize the Ti:Sapphire laser via spectroscopy of the ^{39}K ground state cross-over to excited state $F'=2$ transition in a heated glass cell. The error signal is, like for the Dy blue setup, created by FMTS, and a double feedback loop is acting on a slow (cutoff at 50 Hz), and a fast (100 kHz) piezo.

²⁰M² lasers SolsTiS

²¹Coherent Verdi V18

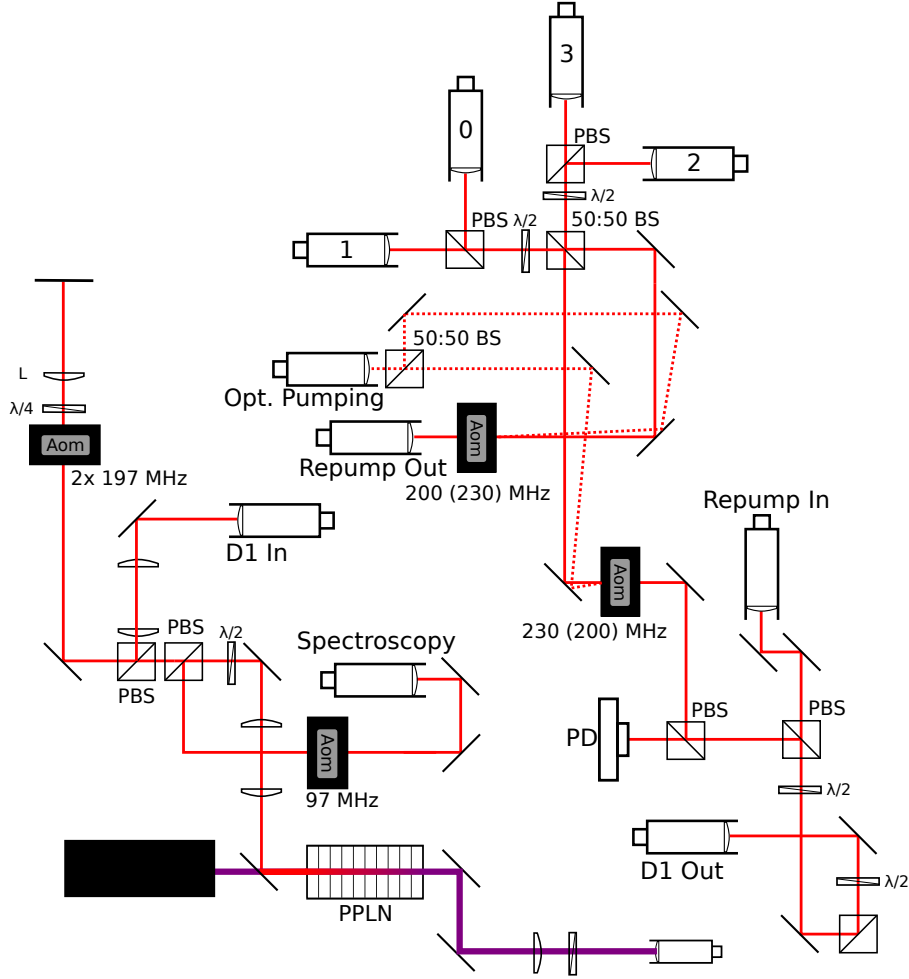


Figure A.10: Schematic drawing of the potassium D1 laser setup.

A.7.2 K D1 Setup

Potassium features a not very well resolved splitting inside the $4^2P_{3/2}$ manifold, and therefore the performance of various sub-Doppler cooling schemes can be limited. An excellent alternative has been well documented by the Li-K mixture experiment in Paris [123, 232], they perform grey-molasses cooling on the D1, $4^2S_{1/2}$ to $4^2P_{1/2}$, transition with a wavelength of 770 nm. Sub-Doppler cooling schemes are vital for alkali-metal based cold atom experiments because they dramatically increase the phase-space density, and therefore create much more favorable starting conditions for evaporative cooling. Our D1 laser (Fig. A.10) is based on a frequency doubled 1540 nm infrared fiber laser, and the setup is similar to the Dy 626 nm setup (Sec. A.6.2). A

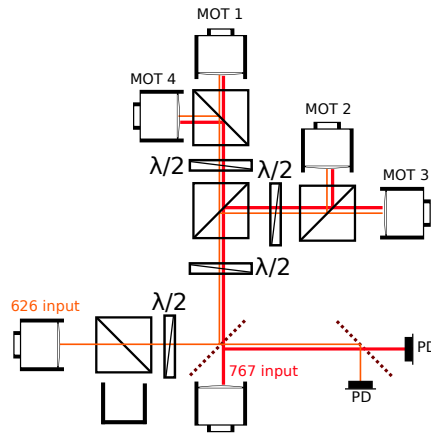


Figure A.11: Schematic drawing of the beam paths for the Dy (626 nm) and K (767 nm) MOT light. The two wavelengths are combined on a dichroic mirror and then divided over 4 fibers. The power is monitored on two photodiodes (PD).

narrow linewidth seed laser²² is amplified by a 10 W fiber amplifier²³ and we then perform second-harmonic generation in a single-pass PPLN crystal²⁴. The repumper however, is created in a different matter as compared to the D2 setup, because we require a pure repumper beam for optical pumping to create an atomic sample in either of the stretched states. Like we use for the reference light at 626 nm, we create a broadband frequency shifter by driving a fiber EOM²⁵ with a strong saw-tooth rf signal. In this way we can create single frequency, pure repumper light with a shifting efficiency of up to 85%, the input power in the EOM is limited, however, to about 25 mW. We combine the pump and repump light with the same polarization on a 50/50 beam-splitter and then couple it into 4 fibers, which deliver the light to the main experimental table.

A.8 MOT Optics

The 3D MOT light for K and Dy is mixed on a dichroic mirror and distributed over the 4 delivery fibers on a miniature stainless-steel optical setup (150x114 mm)²⁶, as is shown in Fig. A.11. This creates a much simpler and compact setup to create the desired MOT beam sizes on the main table, because there is no more mixing required. All the optics however as a con-

²²NKT Photonics Koheras Adjustik

²³Quantel Eylsa

²⁴Covesion

²⁵Photline NIR-MPX800-LN-10

²⁶Thorlabs FiberBench

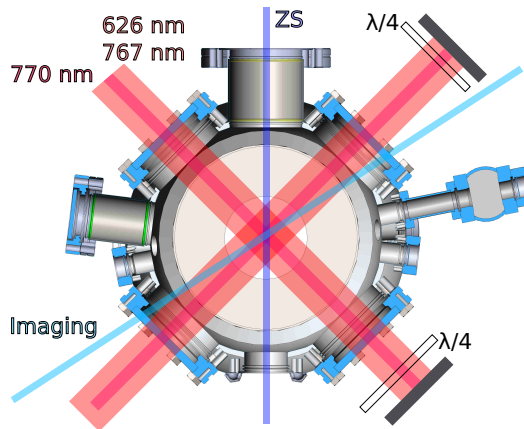


Figure A.12: MOT, D1, ZS and imaging beam geometries in the horizontal plane of the main chamber.

sequence will have to be achromatic, including the waveplates. The dual-wavelength MOT light on the main table is combined with the D1 light via a PBS, so they have an opposite polarization as is shown in Fig. A.12. The beams then pass through a telescope to increase the beam size to 28 mm diameter for the 3D MOT and 15 mm for the D1 light. We use achromatic zero-order waveplates with a diameter of 60 mm²⁷ for the retro-reflected beams and a 25 mm diameter for the incoming beams.

A.9 Optical Dipole Traps

The experiment uses two different far off-resonant dipole trap (ODT) geometries. The reservoir trap (rODT) is a large volume ODT with a good overlap with the compressed clouds leading to a large loading efficiency. The science trap beams (sODT) on the other hand are much more tightly focused, which is beneficial during the evaporation sequence because the higher trap frequency gives a larger scattering and thermalisation rate. The full geometry is shown in Fig.A.13.

A.9.1 Reservoir Dipole Trap

The reservoir trap is constructed by crossing two elliptical beams in the horizontal plane with a 18° angle, where both are focues to a waist of $85 \mu\text{m}$ vertically and $160 \mu\text{m}$ horizontally. The light is coming from a 100 W multimode fiber laser²⁸ with a 1070 nm wavelength and stabilize the intensity

²⁷Astropribor

²⁸IPG YLR-100-LP

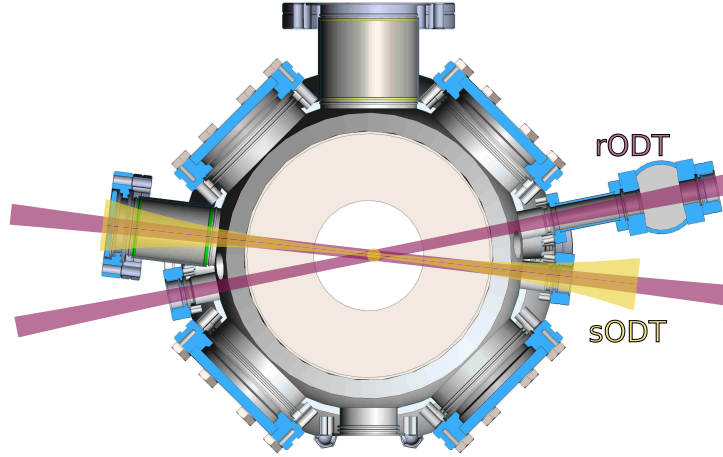


Figure A.13: Horizontal cut through the main chamber with a depiction of the crossed rODT, in red, and sODT, in yellow. The rODT crosses under a 18° angle, while the sODT has a tightly focussed beam in the horizontal plane and the second beam in the vertical.

by controlling the rf power of a high-power quartz AOM²⁹. This AOM is crucial in our experiment because it eliminates almost all thermal lensing we experienced with the more conventional Tellurium dioxide AOM we tried before. The two trapping beams propagate in the same direction and have an opposite polarization to minimize interference.

A.9.2 Science Dipole Trap

Some previous Dy experiments state that their atom lifetimes are strongly reduced if they use multimode ODT lasers[113, 233]. So we use a different laser to create our tightly focused science trap: a narrow-linewidth, low intensity noise, Master-Oscillator Power Amplifier (MOPA)³⁰ with an output of 18 W and a wavelength of 1064 nm. We create the nearly spherical science trap by crossing a $26 \mu\text{m}$ waist beam in the horizontal direction with a nearly vertical beam ($60 \mu\text{m}$ waist). Both beams are fiber coupled for increased pointing stability, and feature independent AOMs to power stabilize and create a frequency difference between them.

²⁹AA Opto-Electronic

³⁰Innolight Mephisto MOPA 18NE

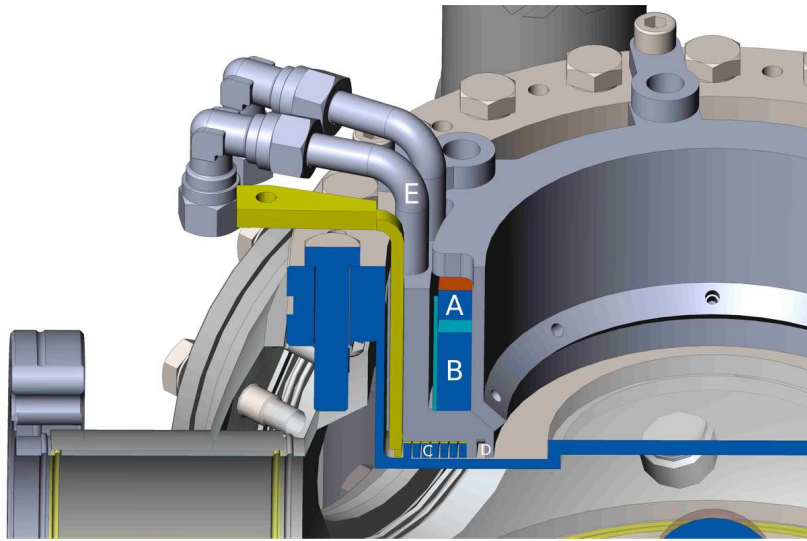


Figure A.14: Vertical cut through the coil stack with the curvature (A), gradient (B), Feshbach coil (C) with in yellow the terminal lead, jump coil (D) and water cooling (E) all fitted inside the inverted viewports on the main chamber.

A.10 Magnetic Coils

This section covers the different coils in the Dy-K mixture experiment and their use cases. We can generate three different types of fields: a gradient, offset and curvature field. All the high-field generating coils are located close to the atoms inside the inverted viewports. The large electrical powers in a small volume require water-cooling to control the temperatures and especially the heat-load on the experiment. A cut through of the coil stack inside the water-cooled holder is shown in Fig.A.14. The coil holder itself is made out of brass and features a slit to limit eddy currents. The watercooling loop is located in-between part B and C in Fig.A.14 and it has two loops (with opposite flow direction), each with 8 mm waterpipes.

A.10.1 Gradient Coil

Gradients have three main use cases during the sequence, first they are a key ingredient to make a MOT, and secondly we can use a gradient to levitate the atoms, for example to compensate for gravity or to ensure good overlap between the two species, and finally they can separate different spin-states (so-called Stern-Gerlach separation). The magnetic field gradient is created in a pair of coils positioned in an anti-Helmholtz configuration, and they are designed to minimize the amount of curvature to make the gradient as linear as possible. This eliminates additional (anti)trapping during their op-

eration and therefore decouples all task between the different coils and ODT beams. Each coil contains 68 windings and the pair produces a gradient of about 1.37 G/cm/A in the vertical direction, and about half of that in the horizontal plane. The coil is labeled by B in Fig. A.14. The current is provided by a powersupply with a maximum voltage of 80 V and a maximum current of 60 A, the maximum current is only needed for fast Stern-Gerlach separation or magnetic trapping. The direction of the gradient can be reversed by changing the current direction via an H-bridge, made out of four, high-power, metal-oxide semiconductor field-effect transistors (MOSFETS). The current is actively stabilized using a precision current transducer and a PID circuit acting on a separate high-power MOSFET.

A.10.2 Feshbach Coil

Large offset fields up to about 300 G can be created by the so-called Feshbach coils. This pair of coils is positioned in a Helmholtz configuration which exactly cancels the field gradient and curvature (up to second order) in the central region. It is beneficial to be able to quickly switch the field magnitude, which requires an as low as possible inductance. The only remaining degree of freedom to change the impedance for a coil in a given geometry is the amount of windings, which has to be balanced with the given maximum current of the used powersupply (200 A). This leads in our case to a coil that has 14 windings, and the switching speed of our setup is not limited by the coils but by the induced eddy-currents in the vacuum chamber.

Different design philosophies exist for the construction of Feshbach coils: usually the space constraints given by the experimental setup lead to a slight deviation from the ideal Helmholtz configuration, and the resulting curvature can be compensated by additional coils. This compensation is never ideal however, since ideally the two currents should be perfectly synchronized for the curvature to cancel during field ramps, while usually it is impossible to cancel the curvature in all directions at the same time. Because D_y is strongly magnetic we designed our coils to be with as little curvature as possible. This can be achieved, even in the tightly confided region inside the inverted viewport by making a very flat coil, in our case it has only two layers with each 7 windings. Conventional wiring, like the ones used for the ZS and gradient coils, has a rather thick layer of isolation around the copper core (on the order of 0.2 mm), which leads to a low copper filling factor, $\eta = V_{copper}/V_{total}$, and bad thermal conductivity. A high filling factor is beneficial because it at the same time lowers the resistivity, while increasing the current density homogeneity. Higher filling factors can be achieved by changing from a more traditional wound coil, to a machined coil. One example of this type, and the inspiration for our design, is the so-called Bitter type coil [234, 235]. Bitter type coils are ideally suited to generate

extremely high magnetic fields, but are generally very tall and thin. Which is exactly the opposite geometry we want to realize. The construction of a Bitter type coil is as follows: one alternates between circular copper plates with a small cut out filled with an isolating material and isolation layers with a small cut out filled with a copper plate. By stacking all these layers in a slightly rotating fashion one is able to create a coil with a single winding per layer. Our design is based on this idea, but only takes two copper layers, each 2 mm thick, and we wire erode 7 windings in a single layer. We then isolate the two layers from each other and from the brass mount with a special 25 μm Kapton foil featuring a 25 μm thick B-staged acrylic adhesive on both sides ³¹. The windings within a single layer are isolated from each other with a flat Teflon ribbon. By baking and pressing the whole structure we were able to bond all the different components together, resulting in a very strong coil, with a very high filling factor and good thermal conductivity towards the watercooled holder. A brazed connection between the last winding of the lowest layer and the first of the upper layer establishes a durable link to close the circuit, and the same technique is used to connect vertical bars as input and output terminals. Part of the coil with a single terminal are shown in Fig. A.14, labeled by C.

The current in the coil has a similar active stabilization as the gradient coil with a precision current transducer and a PID circuit, but instead of a single high-power MOSFET the Feshbach loop features 5 parallel MOSFETs that were selected from a large batch to achieve similar threshold voltages across all 5. Driving the coil is a switching powersupply able to deliver 16 V and up to 200 A ³².

A.10.3 Curvature Coil

One level further away (Coil A in Fig. A.14) from the atoms as compared to the gradient coil is another pair of coils, these can be used to create a strong curvature of the magnetic field. This curvature can be used for trapping. It is also possible to reverse the current direction in one of the coils to create an additional gradient coil. Each coil has 22 windings.

A.10.4 Jump Coil

On the inner side of the coil holder, labeled D in Fig.A.14, a small slit houses a coil that consists out of only two windings. The smaller diameter combined with a low number of windings gives a very low inductance and this coil is therefore suitable to create fast magnetic field changes. This is

³¹DuPont Pyralux LF0111 Bondply

³²Delta Elektronika SM15-200D

the so-called jump coil, and it could also be used to create fast oscillating fields, for example to perform magnetic field modulation spectroscopy.

A.10.5 Offset Coil

All the coils discussed so-far were located inside the inverted viewports, however, surrounding the entire vacuum setup we also have three large pairs of coils to compensate earth's magnetic field and to apply small fields in any desired direction. These form a large cage (1.2 m length, 1 m width and 0.7 m height, as depicted in Fig. A.4), and their fields are very homogeneous but can only reach about 1 G in the horizontal directions and 2 G in the vertical direction. The large size of the coils has a number of advantages: they do not interfere with any of the optics and they can also be used to compensate fields during transport into a future science glass cell. We drive the coils with home-made bipolar current-sources (± 10 A) with active feedback, where the current is measured through high-precision resistors. In the vertical direction the coils generate 0.162(1) G/A, while in the y-direction it is 0.080(1) G/A and in the x-direction 0.101(1) G/A.

A.11 Imaging and Data Analysis

The final stage of every experimental run is the imaging stage. The DyK experiment has two cameras, one scientific Complementary Metal-Oxide-Semiconductor(sCMOS)³³ camera to image both species in the horizontal direction, and an Electron Multiplying Charge-Coupled Device (EMCCD)³⁴ to image Dy in the vertical direction.

A.11.1 Horizontal Imaging

sCMOS cameras are a relatively new development which achieved to combine the existing advantages of CMOS technology, like large pixel count and fast read-out, with new improvements focusing on low read noise, high dynamic range and high quantum efficiency. We use this camera to perform absorption imaging, and we use the extremely fast read-out to image both species with minimum delay. The much larger number of pixels (2560x2160) as compared to conventional CCD chips means we have a very large field of view, and therefore can image both small objects like an expanding Bose-Einstein condensate, or large like a MOT, without changing the magnification of the setup. A large field of view for a sideview camera is also very advantageous because one can perform large expansion times without the cloud falling past the sensor's field of view. Every pixel in a CMOS camera has its own analog to digital converter (ADC), and in our case we use the

³³Andor NEO 5.5

³⁴Andor iXon DU897

ADC to temporarily store a full image while the next one is being exposed. This trick allows to take two images in extremely close succession of about 200-500 ns, and enables dual species absorption imaging on a single camera with an almost identical time-of-flight (ToF). To image the cloud onto the chip we use a two lens setup, both are 1" achromatic lenses, the first one with a focal-length of 225 mm and the second of 500 mm, which gives a measured magnification of 2.27x. On the other side of the chamber we mix the 421 nm and 767 nm imaging lights on a dichroic mirror.

A.11.2 Vertical Imaging

Adding an imaging system in the vertical direction is more difficult to accomplish in our case because every wavelength we use passes through this pair of viewports, and most of them have to be aligned with gravity. We can only image Dy in the vertical direction, because for K we the same wavelength for imaging as for the 3D MOT it is not possible to separate them on a dichroic mirror like we do for Dy. And we already use the opposite polarization for our D1 cooling scheme. We both combine and separate the blue imaging light on custom 3" wedged dichroic mirrors. The atoms are imaged through a high NA aspheric lens positioned directly beneath the glass of the lower viewport, with a resolution of about 1 μm . This lens is AR coated for all the wavelengths we use in the experiments, ranging from 421 nm to 1064 nm, and it is large enough to allow for the desired MOT beam size. After separating the blue and infrared light on the first dichroic mirror from the visible MOT wavelengths, we separate the blue from the infrared with a second dichroic, where the imaging light is always takes the reflected path. Finally the image is created by the EMCCD camera with a resolution of 512x512 pixels.

A.11.3 Data Analysis

The DyK experiment can run fully automated experimental scans while performing real time data analysis and plotting. All these task are split up among different programs and computers and the structure is as follows. The sequence is generated on a Windows 7 computer by an open-source c++ program called Control³⁵ with a PCIe DAC card³⁶. The DAC generates a bus system (16 bit data with 4x 8 bit addresses) with a 2 MHz clock speed. The cameras are operated by another computer running Scientific Linux 7. The camera interface is written in c++ and uses the qt-framework and the software development kit (SDK) provided by the camera manufacturer. The camera interface program hands over the pictures to Matlab for image analysis and fitting. Matlab also combines the sequence parameters with

³⁵strontiumbec.com

³⁶National Instruments NI6534

the image analysis results into a single measurement file, which is then put into a MariaDB database. The contents of the database are then read out and plotted by an open-source python program called sqldataplot³⁷, which updates in real time.

³⁷<https://github.com/wakalixes/sqldataplot>

Bibliography

- [1] J. Bardeen, L. N. Cooper, and J. R. Schrieffer, Microscopic Theory of Superconductivity, *Phys. Rev.* **106**, 162 (1957).
- [2] K. von Klitzing, The quantized Hall effect, *Rev. Mod. Phys.* **58**, 519 (1986).
- [3] A. H. Castro Neto, F. Guinea, N. M. R. Peres, K. S. Novoselov, and A. K. Geim, The electronic properties of graphene, *Rev. Mod. Phys.* **81**, 109 (2009).
- [4] D. M. Ginsberg, *Physical properties of high temperature superconductors III*, Vol. 3 (World Scientific, 1992).
- [5] M. N. Baibich, J. M. Broto, A. Fert, F. N. Van Dau, F. Petroff, P. Etienne, G. Creuzet, A. Friederich, and J. Chazelas, Giant Magnetoresistance of (001)Fe/(001)Cr Magnetic Superlattices, *Phys. Rev. Lett.* **61**, 2472 (1988).
- [6] R. Feynman, Simulating Physics with Computers, *Int. J. Theor. Phys.* **21**, 467 (1982).
- [7] M. H. Anderson, J. R. Ensher, M. R. Matthews, C. E. Wieman, and E. A. Cornell, Observation of Bose-Einstein condensation in dilute atomic vapor, *Science* **269**, 198 (1995).
- [8] K. B. Davis, M. O. Mewes, M. R. Andrews, N. J. van Druten, D. S. Durfee, D. M. Kurn, and W. Ketterle, Bose-Einstein condensation in a gas of sodium atoms, *Phys. Rev. Lett.* **75**, 3969 (1995).
- [9] C. C. Bradley, C. A. Sackett, J. J. Tollett, and R. G. Hulet, Evidence of Bose-Einstein condensation in an atomic gas with attractive interactions, *Phys. Rev. Lett.* **75**, 1687 (1995).
- [10] S. Jochim, M. Bartenstein, A. Altmeyer, G. Hendl, S. Riedl, C. Chin, J. Hecker Denschlag, and R. Grimm, Bose-Einstein Condensation of Molecules, *Science* **302**, 2101 (2003).

- [11] M. Greiner, C. A. Regal, and D. S. Jin, Emergence of a Molecular Bose-Einstein Condensate from a Fermi Gas, *Nature (London)* **426**, 537 (2003).
- [12] M. W. Zwierlein, C. A. Stan, C. H. Schunck, S. M. F. Raupach, S. Gupta, Z. Hadzibabic, and W. Ketterle, Observation of Bose-Einstein Condensation of Molecules, *Phys. Rev. Lett.* **91**, 250401 (2003).
- [13] M. Greiner, O. Mandel, T. Esslinger, T. W. Hänsch, and I. Bloch, Quantum phase transition from a superfluid to a Mott insulator in a gas of ultracold atoms, *Nature (London)* **415**, 39 (2002).
- [14] M. Horikoshi, S. Nakajima, M. Ueda, and T. Mukaiyama, Measurement of universal thermodynamic functions for a unitary Fermi gas, *Science* **327**, 442 (2010).
- [15] N. Navon, S. Nascimbène, F. Chevy, and C. Salomon, The Equation of State of a Low-Temperature Fermi Gas with Tunable Interactions, *Science* **328**, 729 (2010).
- [16] M. J. H. Ku, A. T. Sommer, L. W. Cheuk, and M. W. Zwierlein, Revealing the Superfluid Lambda Transition in the Universal Thermodynamics of a Unitary Fermi Gas, *Science* **335**, 563 (2012).
- [17] T. Kraemer, M. Mark, P. Waldburger, J. G. Danzl, C. Chin, B. Engeser, A. D. Lange, K. Pilch, A. Jaakkola, H.-C. Nägerl, and R. Grimm, Evidence for Efimov quantum states in an ultracold gas of caesium atoms, *Nature (London)* **440**, 315 (2006).
- [18] P. Naidon and S. Endo, Efimov physics: a review, *Rep. Prog. Phys.* **80**, 056001 (2017).
- [19] J. L. Roberts, N. R. Clausen, S. L. Cornish, E. A. Donley, E. A. Cornell, and C. E. Wieman, Controlled collapse of a Bose-Einstein condensate, *Phys. Rev. Lett.* **86**, 4211 (2001).
- [20] H. Kadau, M. Schmitt, M. Wenzel, C. Wink, T. Maier, I. Ferrier-Barbut, and T. Pfau, Observing the Rosensweig instability of a quantum ferrofluid, *Nature (London)* **530**, 194 (2016).
- [21] F. Böttcher, J.-N. Schmidt, M. Wenzel, J. Hertkorn, M. Guo, T. Langen, and T. Pfau, Transient Supersolid Properties in an Array of Dipolar Quantum Droplets, *Phys. Rev. X* **9**, 011051 (2019).
- [22] L. Tanzi, E. Lucioni, F. Famà, J. Catani, A. Fioretti, C. Gabbanini, R. N. Bisset, L. Santos, and G. Modugno, Observation of a Dipolar Quantum Gas with Metastable Supersolid Properties, *Phys. Rev. Lett.* **122**, 130405 (2019).

- [23] L. Chomaz, D. Petter, P. Ilzhöfer, G. Natale, A. Trautmann, C. Politi, G. Durastante, R. M. W. van Bijnen, A. Patscheider, M. Sohmen, M. J. Mark, and F. Ferlaino, Long-Lived and Transient Supersolid Behaviors in Dipolar Quantum Gases, *Phys. Rev. X* **9**, 021012 (2019).
- [24] D. Greif, T. Uehlinger, G. Jotzu, L. Tarruell, and T. Esslinger, Short-range quantum magnetism of ultracold fermions in an optical lattice, *Science* **340**, 1307 (2013).
- [25] G. Roati, C. D’Errico, L. Fallani, M. Fattori, C. Fort, M. Zaccanti, G. Modugno, M. Modugno, and M. Inguscio, Anderson localization of a non-interacting Bose–Einstein condensate, *Nature* **453**, 895 (2008).
- [26] T. Bothwell, D. Kedar, E. Oelker, J. M. Robinson, S. L. Bromley, W. Tew, J. Ye, and C. J. Kennedy, JILA SrI optical lattice clock with uncertainty of 2.0×10^{-18} , *Metrologia* **56**, 065004 (2019).
- [27] P. R. Berman, *Atom interferometry* (Academic press, 1997).
- [28] J. Kitching, S. Knappe, and E. A. Donley, Atomic sensors—a review, *IEEE Sensors Journal* **11**, 1749 (2011).
- [29] K.-H. Bennemann and J. B. Ketterson, *Novel Superfluids: Volumes 1 and 2* (Oxford University Press, Oxford, 2013, 2014).
- [30] W. Ketterle, D. S. Durfee, and D. M. Stamper-Kurn, Making, probing and understanding Bose-Einstein condensates, Proceedings of the International School of Physics - Enrico Fermi **67** (1999), arXiv:cond-mat/9904034.
- [31] R. Haussmann and W. Zwerger, Thermodynamics of a trapped unitary Fermi gas, *Phys. Rev. A* **78**, 063602 (2008).
- [32] K. Gubbels and H. Stoof, Imbalanced Fermi gases at unitarity, *Phys. Rep.* **525**, 255 (2013).
- [33] J. Wang, Y. Che, L. Zhang, and Q. Chen, Enhancement effect of mass imbalance on Fulde-Ferrell-Larkin-Ovchinnikov type of pairing in Fermi-Fermi mixtures of ultracold quantum gases, *Sci. Rep.* **7**, 39783 (2017).
- [34] M. Inguscio, W. Ketterle, and C. Salomon, eds., *Ultra-cold Fermi Gases* (IOS Press, Amsterdam, 2008) Proceedings of the International School of Physics “Enrico Fermi”, Course CLXIV, Varenna, 20-30 June 2006.
- [35] W. Ketterle and N. J. van Druten, Evaporative Cooling of Trapped Atoms, *Adv. At. Mol. Opt. Phys.* **37**, 181 (1996).

- [36] J. L. Bohn, M. Cavagnero, and C. Ticknor, Quasi-universal dipolar scattering in cold and ultracold gases, [New J. Phys. **11**, 055039 \(2009\)](#).
- [37] B. DeMarco and D. S. Jin, Onset of Fermi Degeneracy in a Trapped Atomic Gas, [Science **285**, 1703 \(1999\)](#).
- [38] A. G. Truscott, K. E. Strecker, W. I. McAlexander, G. B. Partridge, and R. G. Hulet, Observation of Fermi Pressure in a Gas of Trapped Atoms, [Science **291**, 2570 \(2001\)](#).
- [39] F. Schreck, L. Khaykovich, K. L. Corwin, G. Ferrari, T. Bourdel, J. Cubizolles, and C. Salomon, Quasipure Bose-Einstein Condensate Immersed in a Fermi Sea, [Phys. Rev. Lett. **87**, 080403 \(2001\)](#).
- [40] T. Fukuhara, Y. Takasu, M. Kumakura, and Y. Takahashi, Degenerate Fermi gases of ytterbium, [Phys. Rev. Lett. **98**, 030401 \(2007\)](#).
- [41] J. M. McNamara, T. Jelten, A. S. Tychkov, W. Hogervorst, and W. Vassen, Degenerate Bose-Fermi Mixture of Metastable Atoms, [Phys. Rev. Lett. **97**, 080404 \(2006\)](#).
- [42] B. J. DeSalvo, M. Yan, P. G. Mickelson, Y. N. Martinez de Escobar, and T. C. Killian, Degenerate Fermi Gas of ^{87}Sr , [Phys. Rev. Lett. **105**, 030402 \(2010\)](#).
- [43] M. K. Tey, S. Stellmer, R. Grimm, and F. Schreck, Double-degenerate Bose-Fermi mixture of strontium, [Phys. Rev. A **82**, 011608 \(2010\)](#).
- [44] B. Naylor, A. Reigue, E. Maréchal, O. Gorceix, B. Laburthe-Tolra, and L. Vernac, Chromium dipolar Fermi sea, [Phys. Rev. A **91**, 011603 \(2015\)](#).
- [45] M. Lu, N. Q. Burdick, and B. L. Lev, Quantum Degenerate Dipolar Fermi Gas, [Phys. Rev. Lett. **108**, 215301 \(2012\)](#).
- [46] L. De Marco, G. Valtolina, K. Matsuda, W. G. Tobias, J. P. Covey, and J. Ye, A degenerate Fermi gas of polar molecules, [Science **363**, 853 \(2019\)](#).
- [47] K. Aikawa, A. Frisch, M. Mark, S. Baier, R. Grimm, and F. Ferlaino, Reaching Fermi Degeneracy via Universal Dipolar Scattering, [Phys. Rev. Lett. **112**, 010404 \(2014\)](#).
- [48] N. Q. Burdick, Y. Tang, and B. L. Lev, Long-Lived Spin-Orbit-Coupled Degenerate Dipolar Fermi Gas, [Phys. Rev. X **6**, 031022 \(2016\)](#).
- [49] P. Courteille, R. S. Freeland, D. J. Heinzen, F. A. van Abeelen, and B. J. Verhaar, Observation of a Feshbach Resonance in Cold Atom Scattering, [Phys. Rev. Lett. **81**, 69 \(1998\)](#).

- [50] C. Chin, R. Grimm, P. S. Julienne, and E. Tiesinga, Feshbach resonances in ultracold gases, *Rev. Mod. Phys.* **82**, 1225 (2010).
- [51] K. M. O'Hara, S. L. Hemmer, M. E. Gehm, S. R. Granade, and J. E. Thomas, Observation of a Strongly Interacting Degenerate Fermi Gas, *Science* **298**, 2179 (2002).
- [52] C. A. Regal, M. Greiner, and D. S. Jin, Observation of Resonance Condensation of Fermionic Atom Pairs, *Phys. Rev. Lett.* **92**, 040403 (2004).
- [53] M. Bartenstein, A. Altmeyer, S. Riedl, S. Jochim, C. Chin, J. Hecker Denschlag, and R. Grimm, Collective Excitations of a Degenerate Gas at the BEC-BCS Crossover, *Phys. Rev. Lett.* **92**, 203201 (2004).
- [54] J. Kinast, S. L. Hemmer, M. E. Gehm, A. Turlapov, and J. E. Thomas, Evidence for Superfluidity in a Resonantly Interacting Fermi Gas, *Phys. Rev. Lett.* **92**, 150402 (2004).
- [55] C. Chin, M. Bartenstein, A. Altmeyer, S. Riedl, S. Jochim, J. Hecker Denschlag, and R. Grimm, Observation of the Pairing Gap in a Strongly Interacting Fermi Gas, *Science* **305**, 1128 (2004).
- [56] P. Pieri, A. Perali, G. C. Strinati, S. Riedl, M. J. Wright, A. Altmeyer, C. Kohstall, E. R. Sánchez Guajardo, J. Hecker Denschlag, and R. Grimm, Pairing-gap, pseudogap, and no-gap phases in the radio-frequency spectra of a trapped unitary ^6Li gas, *Phys. Rev. A* **84**, 011608 (2011).
- [57] M. W. Zwierlein, J. R. Abo-Shaeer, A. Schirotzek, C. H. Schunck, and W. Ketterle, Vortices and Superfluidity in a Strongly Interacting Fermi Gas, *Nature (London)* **435**, 1047 (2005).
- [58] D. E. Miller, J. K. Chin, C. A. Stan, Y. Liu, W. Setiawan, C. Sanner, and W. Ketterle, Critical Velocity for Superfluid Flow across the BEC-BCS Crossover, *Phys. Rev. Lett.* **99**, 070402 (2007).
- [59] L. A. Sidorenkov, M. K. Tey, R. Grimm, Y.-H. Hou, L. Pitaevskii, and S. Stringari, Second sound and the superfluid fraction in a Fermi gas with resonant interactions, *Nature* **498**, 78 (2013).
- [60] D. Stadler, S. Krinner, J. Meineke, J.-P. Brantut, and T. Esslinger, Observing the drop of resistance in the flow of a superfluid Fermi gas, *Nature (London)* **491**, 736 (2012).
- [61] D. Husmann, S. Uchino, S. Krinner, M. Lebrat, T. Giamarchi, T. Esslinger, and J.-P. Brantut, Connecting strongly correlated superfluids by a quantum point contact, *Science* **350**, 1498 (2015).

- [62] A. Sommer, M. Ku, G. Roati, and M. W. Zwierlein, Universal spin transport in a strongly interacting Fermi gas, *Nature* **472**, 201 (2011).
- [63] M. W. Zwierlein, A. Schirotzek, C. H. Schunck, and W. Ketterle, Fermionic Superfluidity with Imbalanced Spin Populations, *Science* **311**, 492 (2006).
- [64] Y. Shin, C. H. Schunck, A. Schirotzek, and W. Ketterle, Phase diagram of a two-component Fermi gas with resonant interactions, *Nature (London)* **451**, 689 (2008).
- [65] L. Radzihovsky and D. E. Sheehy, Imbalanced Feshbach-resonant Fermi gases, *Rep. Prog. Phys.* **73**, 076501 (2010).
- [66] Y. Liao, A. S. C. Rittner, T. Paprotta, W. Li, G. B. Partridge, R. G. Hulet, S. K. Baur, and E. J. Mueller, Spin-imbalance in a one-dimensional Fermi gas, *Nature (London)* **467**, 567 (2010).
- [67] S. Kuhr, Quantum-gas microscopes: a new tool for cold-atom quantum simulators, *Natl. Sci. Rev.* **3**, 170 (2016).
- [68] A. Mazurenko, C. S. Chiu, G. Ji, M. F. Parsons, M. Kanász-Nagy, R. Schmidt, F. Grusdt, E. Demler, D. Greif, and M. Greiner, A cold-atom Fermi–Hubbard antiferromagnet, *Nature* **545**, 462 (2017).
- [69] D. J. Scalapino, The case for $d_{x^2-y^2}$ pairing in the cuprate superconductors, *Phys. Rep.* **250**, 329 (1995).
- [70] W. Hofstetter, J. I. Cirac, P. Zoller, E. Demler, and M. D. Lukin, High-Temperature Superfluidity of Fermionic Atoms in Optical Lattices, *Phys. Rev. Lett.* **89**, 220407 (2002).
- [71] M. Taglieber, A.-C. Voigt, T. Aoki, T. W. Hänsch, and K. Dieckmann, Quantum Degenerate Two-Species Fermi-Fermi Mixture Coexisting with a Bose-Einstein Condensate, *Phys. Rev. Lett.* **100**, 010401 (2008).
- [72] F. M. Spiegelhalder, A. Trenkwalder, D. Naik, G. Kerner, E. Wille, G. Hendl, F. Schreck, and R. Grimm, All-optical production of a degenerate mixture of ^6Li and ^{40}K and creation of heteronuclear molecules, *Phys. Rev. A* **81**, 043637 (2010).
- [73] T. G. Tiecke, M. R. Goosen, A. Ludewig, S. D. Gensemer, S. Kraft, S. J. J. M. F. Kokkelmans, and J. T. M. Walraven, Broad Feshbach resonance in the ^6Li - ^{40}K mixture, *Phys. Rev. Lett.* **104**, 053202 (2010).
- [74] H. Hara, Y. Takasu, Y. Yamaoka, J. M. Doyle, and Y. Takahashi, Quantum Degenerate Mixtures of Alkali and Alkaline-Earth-Like Atoms, *Phys. Rev. Lett.* **106**, 205304 (2011).

- [75] A. Green, H. Li, J. H. S. Toh, X. Tang, K. McCormick, M. Li, E. Tiesinga, S. Kotochigova, and S. Gupta, Feshbach resonances in p -wave three-body recombination within Fermi-Fermi mixtures of open-shell ${}^6\text{Li}$ and closed-shell ${}^{173}\text{Yb}$ atoms, arXiv:1912.04874 (2019).
- [76] S. Taie, Y. Takasu, S. Sugawa, R. Yamazaki, T. Tsujimoto, R. Murakami, and Y. Takahashi, Realization of a $\text{SU}(2) \times \text{SU}(6)$ System of Fermions in a Cold Atomic Gas, *Phys. Rev. Lett.* **105**, 190401 (2010).
- [77] D. Naik, A. Trenkwalder, C. Kohstall, F. M. Spiegelhalder, M. Zaccanti, G. Hendl, F. Schreck, R. Grimm, T. Hanna, and P. Julienne, Feshbach resonances in the ${}^6\text{Li}$ - ${}^{40}\text{K}$ Fermi-Fermi mixture: Elastic versus inelastic interactions, *Eur. Phys. J. D* **65**, 55 (2011).
- [78] M. Jag, M. Cetina, R. S. Lous, R. Grimm, J. Levinsen, and D. S. Petrov, Lifetime of Feshbach dimers in a Fermi-Fermi mixture of ${}^6\text{Li}$ and ${}^{40}\text{K}$, *Phys. Rev. A* **94**, 062706 (2016).
- [79] D. S. Petrov, C. Salomon, and G. V. Shlyapnikov, Weakly bound dimers of fermionic atoms, *Phys. Rev. Lett.* **93**, 090404 (2004).
- [80] S. Jochim, M. Bartenstein, A. Altmeyer, G. Hendl, C. Chin, J. Hecker Denschlag, and R. Grimm, Pure Gas of Optically Trapped Molecules Created from Fermionic Atoms, *Phys. Rev. Lett.* **91**, 240402 (2003).
- [81] J. Cubizolles, T. Bourdel, S. J. J. M. F. Kokkelmans, G. V. Shlyapnikov, and C. Salomon, Production of Long-Lived Ultracold Li_2 Molecules from a Fermi Gas, *Phys. Rev. Lett.* **91**, 240401 (2003).
- [82] C. A. Regal, M. Greiner, and D. S. Jin, Lifetime of Molecule-Atom Mixtures near a Feshbach Resonance in K, *Phys. Rev. Lett.* **92**, 083201 (2004).
- [83] A. Trenkwalder, C. Kohstall, M. Zaccanti, D. Naik, A. I. Sidorov, F. Schreck, and R. Grimm, Hydrodynamic Expansion of a Strongly Interacting Fermi-Fermi Mixture, *Phys. Rev. Lett.* **106**, 115304 (2011).
- [84] M. Jag, M. Zaccanti, M. Cetina, R. S. Lous, F. Schreck, R. Grimm, D. S. Petrov, and J. Levinsen, Observation of a Strong Atom-Dimer Attraction in a Mass-Imbalanced Fermi-Fermi Mixture, *Phys. Rev. Lett.* **112**, 075302 (2014).
- [85] C. Kohstall, M. Zaccanti, M. Jag, A. Trenkwalder, P. Massignan, G. M. Bruun, F. Schreck, and R. Grimm, Metastability and coherence of repulsive polarons in a strongly interacting Fermi mixture, *Nature (London)* **485**, 615 (2012).
- [86] P. S. Zuchowski, J. Aldegunde, and J. M. Hutson, Ultracold RbSr

- molecules can be formed by magnetoassociation, *Phys. Rev. Lett.* **105**, 153201 (2010).
- [87] V. Barbé, A. Ciamei, B. Pasquiou, L. Reichsöllner, F. Schreck, P. S. Żuchowski, and J. M. Hutson, Observation of Feshbach resonances between alkali and closed-shell atoms, *Nat. Phys.* **14**, 881 (2018).
 - [88] E. Neri, A. Ciamei, C. Simonelli, I. Goti, M. Inguscio, A. Trenkwalder, and M. Zaccanti, Realization of a Cold Mixture of Fermionic Chromium and Lithium Atoms, *arXiv preprint arXiv:2001.11616* (2020).
 - [89] D. S. Petrov, C. Salomon, and G. V. Shlyapnikov, Diatomic molecules in ultracold Fermi gases - novel composite bosons, *J. Phys. B* **38**, S645 (2005).
 - [90] A. Petrov, E. Tiesinga, and S. Kotochigova, Anisotropy induced Feshbach resonances in a quantum dipolar gas of magnetic atoms, *Phys. Rev. Lett.* **109**, 103002 (2012).
 - [91] M. Lu, S. H. Youn, and B. L. Lev, Spectroscopy of a narrow-line laser-cooling transition in atomic dysprosium, *Phys. Rev. A* **83**, 012510 (2011).
 - [92] K. D. Bonin and V. V. Kresin, *Electric-dipole polarizabilities of atoms, molecules, and clusters* (World Scientific, 1997).
 - [93] J. Mitroy, M. S. Safronova, and C. W. Clark, Theory and applications of atomic and ionic polarizabilities, *J. Phys. B: At. Mol. Opt. Phys.* **43**, 202001 (2010).
 - [94] H. H. Stroke, *Advances in atomic, molecular, and optical physics*, Vol. 51 (Gulf Professional Publishing, 2005).
 - [95] R. Grimm, M. Weidemüller, and Y. B. Ovchinnikov, Optical dipole traps for neutral atoms, *Adv. At. Mol. Opt. Phys.* **42**, 95 (2000).
 - [96] L. J. LeBlanc and J. H. Thywissen, Species-specific optical lattices, *Phys. Rev. A* **75**, 053612 (2007).
 - [97] A. D. Ludlow, M. M. Boyd, J. Ye, E. Peik, and P. O. Schmidt, Optical atomic clocks, *Rev. Mod. Phys.* **87**, 637 (2015).
 - [98] V. Galitski and I. B. Spielman, Spin-orbit coupling in quantum gases, *Nature (London)* **494**, 49 (2013).
 - [99] D. Sukachev, A. Sokolov, K. Chebakov, A. Akimov, S. Kanorsky, N. Kolachevsky, and V. Sorokin, Magneto-optical trap for thulium atoms, *Phys. Rev. A* **82**, 011405 (2010).

- [100] M. Lu, N. Q. Burdick, S. H. Youn, and B. L. Lev, Strongly Dipolar Bose-Einstein Condensate of Dysprosium, [Phys. Rev. Lett. **107**, 190401 \(2011\)](#).
- [101] K. Aikawa, A. Frisch, M. Mark, S. Baier, A. Rietzler, R. Grimm, and F. Ferlaino, Bose-Einstein Condensation of Erbium, [Phys. Rev. Lett. **108**, 210401 \(2012\)](#).
- [102] K. Aikawa, S. Baier, A. Frisch, M. Mark, C. Ravensbergen, and F. Ferlaino, Observation of Fermi surface deformation in a dipolar quantum gas, [Science **345**, 1484 \(2014\)](#).
- [103] J. Miao, J. Hostetter, G. Stratis, and M. Saffman, Magneto-optical trapping of holmium atoms, [Phys. Rev. A **89**, 041401 \(2014\)](#).
- [104] B. Hemmerling, G. K. Drayna, E. Chae, A. Ravi, and J. M. Doyle, Buffer gas loaded magneto-optical traps for Yb, Tm, Er and Ho, [New J. Phys. **16**, 063070 \(2014\)](#).
- [105] D. Dreon, L. Sidorenkov, C. Bouazza, W. Maineult, J. Dalibard, and S. Nascimbène, Optical cooling and trapping of highly magnetic atoms: the benefits of a spontaneous spin polarization, [J. Phys. B **50**, 065005 \(2017\)](#).
- [106] X. Cui, B. Lian, T.-L. Ho, B. L. Lev, and H. Zhai, Synthetic gauge field with highly magnetic lanthanide atoms, [Phys. Rev. A **88**, 011601 \(2013\)](#).
- [107] V. A. Dzuba, V. V. Flambaum, and B. L. Lev, Dynamic polarizabilities and magic wavelengths for dysprosium, [Phys. Rev. A **83**, 032502 \(2011\)](#).
- [108] M. Lepers, J.-F. Wyart, and O. Dulieu, Anisotropic optical trapping of ultracold erbium atoms, [Phys. Rev. A **89**, 022505 \(2014\)](#).
- [109] D. Sukachev, S. Fedorov, I. Tolstikhina, D. Tregubov, E. Kalganova, G. Vishnyakova, A. Golovizin, N. Kolachevsky, K. Khabarova, and V. Sorokin, Inner-shell magnetic dipole transition in Tm atoms: A candidate for optical lattice clocks, [Phys. Rev. A **94**, 022512 \(2016\)](#).
- [110] H. Li, J.-F. Wyart, O. Dulieu, S. Nascimbène, and M. Lepers, Optical trapping of ultracold dysprosium atoms: transition probabilities, dynamic dipole polarizabilities and van der Waals C_6 coefficients, [J. Phys. B: At. Mol. Opt. Phys. **50**, 014005 \(2017\)](#).
- [111] H. Li, J.-F. Wyart, O. Dulieu, and M. Lepers, Anisotropic optical trapping as a manifestation of the complex electronic structure of ultracold lanthanide atoms: The example of holmium, [Phys. Rev. A **95**, 062508 \(2017\)](#).

- [112] A. A. Golovizin, E. Kalganova, D. Sukachev, G. Vishnyakova, D. Tregubov, K. Khabarova, V. Sorokin, and N. Kolachevsky, Methods for determining the polarisability of the fine structure levels in the ground state of the thulium atom, *Quantum Electron.* **47**, 479 (2017).
- [113] T. Maier, *Interactions in a Quantum Gas of Dysprosium Atoms*, Ph.D. thesis, University of Stuttgart (2015).
- [114] M. Schmitt, *A Self-bound Dilute Quantum Liquid of Dysprosium Atoms*, Ph.D. thesis, University of Stuttgart (2017).
- [115] J. H. Becher, S. Baier, K. Aikawa, M. Lepers, J.-F. Wyart, O. Dulieu, and F. Ferlaino, Anisotropic polarizability of erbium atoms, *Phys. Rev. A* **97**, 012509 (2018).
- [116] I. H. Deutsch and P. S. Jessen, Quantum control and measurement of atomic spins in polarization spectroscopy, *Opt. Commun.* **283**, 681 (2010).
- [117] A. Khramov, A. H., W. Dowd, R. J. Roy, C. Makrides, A. Petrov, S. Kotochigova, and S. Gupta, Ultracold Heteronuclear Mixture of Ground and Excited State Atoms, *Phys. Rev. Lett.* **112**, 033201 (2014).
- [118] B. Neyenhuis, B. Yan, S. A. Moses, J. P. Covey, A. Chotia, A. Petrov, S. Kotochigova, J. Ye, and D. S. Jin, Anisotropic Polarizability of Ultracold Polar $^{40}\text{K}^{87}\text{Rb}$ Molecules, *Phys. Rev. Lett.* **109**, 230403 (2012).
- [119] J. G. Danzl, M. J. Mark, E. Haller, M. Gustavsson, R. Hart, J. Aldegunde, J. M. Hutson, and H.-C. Nägerl, An ultracold high-density sample of rovibronic ground-state molecules in an optical lattice, *Nat. Phys.* **6**, 265 (2010).
- [120] M. S. Safronova, U. I. Safronova, and C. W. Clark, Magic wavelengths for optical cooling and trapping of potassium, *Phys. Rev. A* **87**, 052504 (2013).
- [121] M. S. Safronova, private communication (2017).
- [122] T. Maier, H. Kadau, M. Schmitt, A. Griesmaier, and T. Pfau, Narrow-line magneto-optical trap for dysprosium atoms, *Opt. Lett.* **39**, 3138 (2014).
- [123] D. Fernandes, F. Sievers, N. Kretschmar, S. Wu, C. Salomon, and F. Chevy, Sub-Doppler laser cooling of fermionic ^{40}K atoms in three-dimensional gray optical molasses, *Europhys. Lett.* **100**, 63001 (2012).
- [124] F. Dalfovo, S. Giorgini, L. P. Pitaevskii, and S. Stringari, Theory of Bose-Einstein condensation in trapped gases, *Rev. Mod. Phys.* **71**, 463 (1999).

- [125] V. Flambaum and M. Dzuba, private communication (2017).
- [126] M. Lepers and O. Dulieu, private communication (2017).
- [127] L. D. Carr, D. DeMille, R. V. Krems, and J. Ye, Cold and ultracold molecules: Science, technology and applications, *New J. Phys.* **11**, 055049 (2009).
- [128] G. Quéméner and P. S. Julienne, Ultracold Molecules under Control!, *Chem. Rev.* **112**, 4949 (2012).
- [129] E. B. Norrgard, D. J. McCarron, M. H. Steinecker, M. R. Tarbutt, and D. DeMille, Submillikelvin Dipolar Molecules in a Radio-Frequency Magneto-Optical Trap, *Phys. Rev. Lett.* **116**, 063004 (2016).
- [130] E. Chae, L. Anderegg, B. L. Augenbraun, A. Ravi, B. Hemmerling, N. R. Hutzler, A. L. Collopy, J. Ye, W. Ketterle, and J. M. Doyle, One-dimensional magneto-optical compression of a cold CaF molecular beam, *New J. Phys.* **19**, 033035 (2017).
- [131] P. Soldan, P. S. Zuchowski, and J. M. Hutson, Prospects for sympathetic cooling of polar molecules: NH with alkali-metal and alkaline-earth atoms - a new hope, *Faraday Discuss.* **142**, 191 (2009).
- [132] J. Lim, M. D. Frye, J. M. Hutson, and M. R. Tarbutt, Modeling sympathetic cooling of molecules by ultracold atoms, *Phys. Rev. A* **92**, 053419 (2015).
- [133] M. L. González-Martínez and J. M. Hutson, Ultracold Hydrogen Atoms: A Versatile Coolant to Produce Ultracold Molecules, *Phys. Rev. Lett.* **111**, 203004 (2013).
- [134] W. V. Liu and F. Wilczek, Interior Gap Superfluidity, *Phys. Rev. Lett.* **90**, 047002 (2003).
- [135] M. Iskin and C. A. R. Sá de Melo, Two-Species Fermion Mixtures with Population Imbalance, *Phys. Rev. Lett.* **97**, 100404 (2006).
- [136] M. M. Parish, F. M. Marchetti, A. Lamacraft, and B. D. Simons, Polarized Fermi Condensates with Unequal Masses: Tuning the Tricritical Point, *Phys. Rev. Lett.* **98**, 160402 (2007).
- [137] M. A. Baranov, C. Lobo, and G. V. Shlyapnikov, Superfluid pairing between fermions with unequal masses, *Phys. Rev. A* **78**, 033620 (2008).
- [138] A. Gezerlis, S. Gandolfi, K. E. Schmidt, and J. Carlson, Heavy-light fermion mixtures at unitarity, *Phys. Rev. Lett.* **103**, 060403 (2009).
- [139] J. E. Baarsma, K. B. Gubbels, and H. T. C. Stoof, Population and

- mass imbalance in atomic Fermi gases, [Phys. Rev. A **82**, 013624 \(2010\)](#).
- [140] J. Braun, J. E. Drut, and D. Roscher, Zero-Temperature Equation of State of Mass-Imbalanced Resonant Fermi Gases, [Phys. Rev. Lett. **114**, 050404 \(2015\)](#).
- [141] M. Tinkham, *Introduction to Superconductivity*, 2nd ed. (McGraw-Hill, New York, 1996).
- [142] G. Brown and H. Bethe, A scenario for a large number of low-mass black holes in the galaxy, *Astrophys. J.* **423**, 659 (1994).
- [143] A. Sedrakian, T. Alm, and U. Lombardo, Superfluidity in asymmetric nuclear matter, [Phys. Rev. C **55**, R582 \(1997\)](#).
- [144] R. Casalbuoni and G. Nardulli, Inhomogeneous superconductivity in condensed matter and QCD, [Rev. Mod. Phys. **76**, 263 \(2004\)](#).
- [145] A. Rapp, G. Zaránd, C. Honerkamp, and W. Hofstetter, Color Superfluidity and “Baryon” Formation in Ultracold Fermions, [Phys. Rev. Lett. **98**, 160405 \(2007\)](#).
- [146] F. Wilczek, Quantum chromodynamics: Lifestyles of the small and simple, [Nat. Phys. **3**, 375 \(2007\)](#).
- [147] D. Bailin and A. Love, Superfluidity and superconductivity in relativistic fermion systems, [Phys. Rep. **107**, 325 \(1984\)](#).
- [148] B. C. Barrois, Superconducting quark matter, [Nucl. Phys. B **129**, 390 \(1977\)](#).
- [149] P. Fulde and R. A. Ferrell, Superconductivity in a Strong Spin-Exchange Field, [Phys. Rev. **135**, A550 \(1964\)](#).
- [150] A. I. Larkin and Y. N. Ovchinnikov, Inhomogeneous state of superconductors, *Sov. Phys. JETP* **20**, 762 (1965).
- [151] G. Sarma, On the influence of a uniform exchange field acting on the spins of the conduction electrons in a superconductor, [J. Phys. Chem. Solids **24**, 1029 \(1963\)](#).
- [152] E. Gubankova, W. V. Liu, and F. Wilczek, Breached Pairing Superfluidity: Possible Realization in QCD, [Phys. Rev. Lett. **91**, 032001 \(2003\)](#).
- [153] K. B. Gubbels, J. E. Baarsma, and H. T. C. Stoof, Lifshitz Point in the Phase Diagram of Resonantly Interacting ${}^6\text{Li}$ - ${}^{40}\text{K}$ Mixtures, [Phys. Rev. Lett. **103**, 195301 \(2009\)](#).

- [154] I. Bausmerth, A. Recati, and S. Stringari, Chandrasekhar-Clogston limit and phase separation in Fermi mixtures at unitarity, *Phys. Rev. A* **79**, 043622 (2009).
- [155] K. M. Daily and D. Blume, Thermodynamics of the two-component Fermi gas with unequal masses at unitarity, *Phys. Rev. A* **85**, 013609 (2012).
- [156] R. B. Diener and M. Randeria, BCS-BEC crossover with unequal-mass fermions, *Phys. Rev. A* **81**, 033608 (2010).
- [157] P. Massignan, M. Zaccanti, and G. M. Bruun, Polarons, dressed molecules and itinerant ferromagnetism in ultracold Fermi gases, *Rep. Prog. Phys.* **77**, 034401 (2014).
- [158] A. Amico, F. Scazza, G. Valtolina, P. E. S. Tavares, W. Ketterle, M. Inguscio, G. Roati, and M. Zaccanti, Time-Resolved Observation of Competing Attractive and Repulsive Short-Range Correlations in Strongly Interacting Fermi Gases, *Phys. Rev. Lett.* **121**, 253602 (2018).
- [159] D. S. Petrov, G. E. Astrakharchik, D. J. Papoular, C. Salomon, and G. V. Shlyapnikov, Crystalline Phase of Strongly Interacting Fermi Mixtures, *Phys. Rev. Lett.* **99**, 130407 (2007).
- [160] M. Knap, A. Shashi, Y. Nishida, A. Imambekov, D. A. Abanin, and E. Demler, Time-Dependent Impurity in Ultracold Fermions: Orthogonality Catastrophe and Beyond, *Phys. Rev. X* **2**, 041020 (2012).
- [161] J.-S. You, R. Schmidt, D. A. Ivanov, M. Knap, and E. Demler, Atomtronics with a spin: Statistics of spin transport and nonequilibrium orthogonality catastrophe in cold quantum gases, *Phys. Rev. B* **99**, 214505 (2019).
- [162] Y. Nishida, Transport measurement of the orbital Kondo effect with ultracold atoms, *Phys. Rev. A* **93**, 011606 (2016).
- [163] J. Levinsen, T. G. Tiecke, J. T. M. Walraven, and D. S. Petrov, Atom-dimer scattering and long-lived trimers in fermionic mixtures, *Phys. Rev. Lett.* **103**, 153202 (2009).
- [164] Y. Nishida and S. Tan, Confinement-induced Efimov resonances in Fermi-Fermi mixtures, *Phys. Rev. A* **79**, 060701(R) (2009).
- [165] F. M. Spiegelhalder, A. Trenkwalder, D. Naik, G. Hendl, F. Schreck, and R. Grimm, Collisional stability of ^{40}K immersed in a strongly interacting Fermi Gas of ^6Li , *Phys. Rev. Lett.* **103**, 223203 (2009).
- [166] A. Ridinger, S. Chaudhuri, T. Salez, U. Eismann, D. R. Fernandes, K. Magalhães, D. Wilkowski, C. Salomon, and F. Chevy, Large atom

- number dual-species magneto-optical trap for fermionic ^6Li and ^{40}K atoms, [Eur. Phys. J. D **65**, 223 \(2011\)](#).
- [167] M. Cetina, M. Jag, R. S. Lous, J. T. M. Walraven, R. Grimm, R. S. Christensen, and G. M. Bruun, Decoherence of Impurities in a Fermi Sea of Ultracold Atoms, [Phys. Rev. Lett. **115**, 135302 \(2015\)](#).
- [168] M. Cetina, M. Jag, R. S. Lous, I. Fritsche, J. T. M. Walraven, R. Grimm, J. Levinsen, M. M. Parish, R. Schmidt, M. Knap, and E. Demler, Ultrafast many-body interferometry of impurities coupled to a Fermi sea, [Science **354**, 96 \(2016\)](#).
- [169] E. Wille, F. M. Spiegelhalder, G. Kerner, D. Naik, A. Trenkwalder, G. Hendl, F. Schreck, R. Grimm, T. G. Tiecke, J. T. M. Walraven, S. J. J. M. F. Kokkelmans, E. Tiesinga, and P. S. Julienne, Exploring an ultracold Fermi-Fermi mixture: Interspecies Feshbach resonances and scattering properties of ^6Li and ^{40}K , [Phys. Rev. Lett. **100**, 053201 \(2008\)](#).
- [170] B. D. Esry, C. H. Greene, and H. Suno, Threshold laws for three-body recombination, [Phys. Rev. A **65**, 010705 \(2001\)](#).
- [171] H. Suno, B. D. Esry, and C. H. Greene, Recombination of three ultracold fermionic atoms, [Phys. Rev. Lett. **90**, 053202 \(2003\)](#).
- [172] D. S. Petrov, Three-body problem in Fermi gases with short-range interparticle interaction, [Phys. Rev. A **67**, 010703 \(2003\)](#).
- [173] D. S. Petrov, C. Salomon, and G. V. Shlyapnikov, Scattering properties of weakly bound dimers of fermionic atoms, [Phys. Rev. A **71**, 012708 \(2005\)](#).
- [174] B. Marcelis, S. J. J. M. F. Kokkelmans, G. V. Shlyapnikov, and D. S. Petrov, Collisional properties of weakly bound heteronuclear dimers, [Phys. Rev. A **77**, 032707 \(2008\)](#).
- [175] K. Dieckmann, C. A. Stan, S. Gupta, Z. Hadzibabic, C. H. Schunck, and W. Ketterle, Decay of an Ultracold Fermionic Lithium Gas near a Feshbach Resonance, [Phys. Rev. Lett. **89**, 203201 \(2002\)](#).
- [176] S. Baier, D. Petter, J. H. Becher, A. Patscheider, G. Natale, L. Chomaz, M. J. Mark, and F. Ferlaino, Realization of a Strongly Interacting Fermi Gas of Dipolar Atoms, [Phys. Rev. Lett. **121**, 093602 \(2018\)](#).
- [177] L. Pitaevskii and S. Stringari, *Bose-Einstein Condensation and Superfluidity* (Oxford University Press, 2016).
- [178] W. Zwerger, ed., *The BCS-BEC Crossover and the Unitary Fermi Gas* (Springer, Berlin Heidelberg, 2012).

- [179] G. C. Strinati, P. Pieri, G. Röpke, P. Schuck, and M. Urban, The BCS-BEC crossover: From ultra-cold Fermi gases to nuclear systems, *Phys. Rep.* **738**, 1 (2018).
- [180] A. Trautmann, P. Ilzhöfer, G. Durastante, C. Politi, M. Sohmen, M. J. Mark, and F. Ferlaino, Dipolar Quantum Mixtures of Erbium and Dysprosium Atoms, *Phys. Rev. Lett.* **121**, 213601 (2018).
- [181] M. L. González-Martínez and P. S. Żuchowski, Magnetically tunable Feshbach resonances in Li+Er, *Phys. Rev. A* **92**, 022708 (2015).
- [182] C. Ravensbergen, V. Corre, E. Soave, M. Kreyer, S. Tzanova, E. Kiri-
lov, and R. Grimm, Accurate Determination of the Dynamical Polar-
izability of Dysprosium, *Phys. Rev. Lett.* **120**, 223001 (2018).
- [183] K. Aikawa, A. Frisch, M. Mark, S. Baier, R. Grimm, J. L. Bohn, D. S.
Jin, G. M. Bruun, and F. Ferlaino, Anisotropic Relaxation Dynamics
in a Dipolar Fermi Gas Driven Out of Equilibrium, *Phys. Rev. Lett.*
113, 263201 (2014).
- [184] A. H. Hansen, A. Khramov, W. H. Dowd, A. O. Jamison, V. V. Ivanov,
and S. Gupta, Quantum degenerate mixture of ytterbium and lithium
atoms, *Phys. Rev. A* **84**, 011606 (2011).
- [185] A. H. Hansen, A. Y. Khramov, W. H. Dowd, A. O. Jamison,
B. Plotkin-Swing, R. J. Roy, and S. Gupta, Production of quantum-
degenerate mixtures of ytterbium and lithium with controllable inter-
species overlap, *Phys. Rev. A* **87**, 013615 (2013).
- [186] M. Landini, S. Roy, G. Roati, A. Simoni, M. Inguscio, G. Modugno,
and M. Fattori, Direct evaporative cooling of ^{39}K atoms to Bose-
Einstein condensation, *Phys. Rev. A* **86**, 033421 (2012).
- [187] K. Baumann, N. Q. Burdick, M. Lu, and B. L. Lev, Observation of
low-field Fano-Feshbach resonances in ultracold gases of dysprosium,
Phys. Rev. A **89**, 020701 (2014).
- [188] Y. Takasu, K. Maki, K. Komori, T. Takano, K. Honda, M. Kumakura,
T. Yabuzaki, and Y. Takahashi, Spin-singlet Bose-Einstein condensa-
tion of two-electron atoms, *Phys. Rev. Lett.* **91**, 040404 (2003).
- [189] S. Stellmer, M. K. Tey, B. Huang, R. Grimm, and F. Schreck, Bose-
Einstein condensation of strontium, *Phys. Rev. Lett.* **103**, 200401
(2009).
- [190] C.-L. Hung, X. Zhang, N. Gemelke, and C. Chin, Accelerating evap-
orative cooling of atoms into Bose-Einstein condensation in optical
traps, *Phys. Rev. A* **78**, 011604(R) (2008).

- [191] R. S. Lous, I. Fritsche, M. Jag, B. Huang, and R. Grimm, Thermometry of a deeply degenerate Fermi gas with a Bose-Einstein condensate, *Phys. Rev. A* **95**, 053627 (2017).
- [192] T. Weber, J. Herbig, M. Mark, H.-C. Nägerl, and R. Grimm, Bose-Einstein condensation of cesium, *Science* **299**, 232 (2003).
- [193] A. Mosk, S. Kraft, M. Mudrich, K. Singer, W. Wohlleben, R. Grimm, and M. Weidemüller, Mixture of ultracold lithium and cesium atoms in an optical dipole trap, *Appl. Phys. B* **73**, 791 (2001).
- [194] S. Tassy, N. Nemitz, F. Baumer, C. Höhl, A. Batär, and A. Görlitz, Sympathetic cooling in a mixture of diamagnetic and paramagnetic atoms, *J. Phys. B* **43**, 205309 (2010).
- [195] A. Guttridge, S. A. Hopkins, S. L. Kemp, M. D. Frye, J. M. Hutson, and S. L. Cornish, Interspecies thermalization in an ultracold mixture of Cs and Yb in an optical trap, *Phys. Rev. A* **96**, 012704 (2017).
- [196] S. Kotochigova, Controlling interactions between highly magnetic atoms with Feshbach resonances, *Rep. Prog. Phys.* **77**, 093901 (2014).
- [197] A. Frisch, M. Mark, K. Aikawa, F. Ferlaino, J. L. Bohn, C. Makrides, A. Petrov, and S. Kotochigova, Quantum chaos in ultracold collisions of gas-phase erbium atoms, *Nature (London)* **507**, 475 (2014).
- [198] T. Maier, I. Ferrier-Barbut, H. Kadau, M. Schmitt, M. Wenzel, C. Wink, T. Pfau, K. Jachymski, and P. S. Julienne, Broad universal Feshbach resonances in the chaotic spectrum of dysprosium atoms, *Phys. Rev. A* **92**, 060702 (2015).
- [199] E. Lucioni, L. Tanzi, A. Fregosi, J. Catani, S. Gozzini, M. Inguscio, A. Fioretti, C. Gabbanini, and G. Modugno, Dysprosium dipolar Bose-Einstein condensate with broad Feshbach resonances, *Phys. Rev. A* **97**, 060701 (2018).
- [200] K. Dieckmann, R. J. C. Spreeuw, M. Weidemüller, and J. T. M. Walraven, Two-dimensional magneto-optical trap as a source of slow atoms, *Phys. Rev. A* **58**, 3891 (1998).
- [201] J. Levinsen and D. Petrov, Atom-dimer and dimer-dimer scattering in fermionic mixtures near a narrow Feshbach resonance, *Eur. Phys. J. D* **65**, 67 (2011).
- [202] C. Ravensbergen, V. Corre, E. Soave, M. Kreyer, E. Kirilov, and R. Grimm, Production of a degenerate Fermi-Fermi mixture of dysprosium and potassium atoms, *Phys. Rev. A* **98**, 063624 (2018).
- [203] M. Arndt, M. B. Dahan, D. Guéry-Odelin, M. Reynolds, and J. Dal-

- ibard, Observation of a Zero-Energy Resonance in Cs-Cs Collisions, *Phys. Rev. Lett.* **79**, 625 (1997).
- [204] M. E. Gehm, S. L. Hemmer, K. M. O'Hara, and J. E. Thomas, Unitarity-limited elastic collision rate in a harmonically trapped Fermi gas, *Phys. Rev. A* **68**, 011603 (2003).
- [205] M. Anderlini, D. Ciampini, D. Cossart, E. Courtade, M. Cristiani, C. Sias, O. Morsch, and E. Arimondo, Model for collisions in ultracold-atom mixtures, *Phys. Rev. A* **72**, 033408 (2005).
- [206] T. Bourdel, J. Cubizolles, L. Khaykovich, K. M. F. Magalhães, S. J. J. M. F. Kokkelmans, G. V. Shlyapnikov, and C. Salomon, Measurement of the Interaction Energy near a Feshbach Resonance in a ${}^6\text{Li}$ Fermi Gas, *Phys. Rev. Lett.* **91**, 020402 (2003).
- [207] S. Jochim, *Bose-Einstein Condensation of Molecules*, Ph.D. thesis, Innsbruck University (2004).
- [208] G. Barontini, C. Weber, F. Rabatti, J. Catani, G. Thalhammer, M. Inguscio, and F. Minardi, Observation of heteronuclear atomic Efimov resonances, *Phys. Rev. Lett.* **103**, 043201 (2009).
- [209] R. A. W. Maier, M. Eisele, E. Tiemann, and C. Zimmermann, Efimov Resonance and Three-Body Parameter in a Lithium-Rubidium Mixture, *Phys. Rev. Lett.* **115**, 043201 (2015).
- [210] L. J. Wacker, N. B. Jørgensen, D. Birkmose, N. Winter, M. Mikkelsen, J. Sherson, N. Zinner, and J. J. Arlt, Universal Three-Body Physics in Ultracold KRb Mixtures, *Phys. Rev. Lett.* **117**, 163201 (2016).
- [211] R. S. Bloom, M.-G. Hu, T. D. Cumby, and D. S. Jin, Tests of Universal Three-Body Physics in an Ultracold Bose-Fermi Mixture, *Phys. Rev. Lett.* **111**, 105301 (2013).
- [212] R. Pires, J. Ulmanis, S. Häfner, M. Repp, A. Arias, E. D. Kuhnle, and M. Weidemüller, Observation of Efimov Resonances in a Mixture with Extreme Mass Imbalance, *Phys. Rev. Lett.* **112**, 250404 (2014).
- [213] S.-K. Tung, K. Jiménez-García, J. Johansen, C. V. Parker, and C. Chin, Geometric Scaling of Efimov States in a ${}^6\text{Li}-{}^{133}\text{Cs}$ Mixture, *Phys. Rev. Lett.* **113**, 240402 (2014).
- [214] J. Ulmanis, S. Häfner, R. Pires, F. Werner, D. S. Petrov, E. D. Kuhnle, and M. Weidemüller, Universal three-body recombination and Efimov resonances in an ultracold Li-Cs mixture, *Phys. Rev. A* **93**, 022707 (2016).
- [215] R. S. Lous, I. Fritsche, M. Jag, F. Lehmann, E. Kirilov, B. Huang,

- and R. Grimm, Probing the Interface of a Phase-Separated State in a Repulsive Bose-Fermi Mixture, *Phys. Rev. Lett.* **120**, 243403 (2018).
- [216] S. Tzanova, Ph.D. thesis, University of Innsbruck (in preparation).
- [217] M. W. Zwierlein, A. Schirotzek, C. H. Schunck, and W. Ketterle, Direct observation of the superfluid phase transition in ultracold Fermi gases, *Nature (London)* **442**, 54 (2006).
- [218] A. D. Lange, K. Pilch, A. Prantner, F. Ferlaino, B. Engeser, H.-C. Nägerl, R. Grimm, and C. Chin, Determination of atomic scattering lengths from measurements of molecular binding energies near Feshbach resonances, *Phys. Rev. A* **79**, 013622 (2009).
- [219] K. Jachymski and P. S. Julienne, Analytical model of overlapping Feshbach resonances, *Phys. Rev. A* **88**, 052701 (2013).
- [220] K. M. O'Hara, S. L. Hemmer, S. R. Granade, M. E. Gehm, J. E. Thomas, V. Venturi, E. Tiesinga, and C. J. Williams, Measurement of the zero crossing in a Feshbach resonance of fermionic ${}^6\text{Li}$, *Phys. Rev. A* **66**, 041401 (2002).
- [221] S. Jochim, M. Bartenstein, G. Hendl, J. Hecker Denschlag, R. Grimm, A. Mosk, and W. Weidemüller, Magnetic Field Control of Elastic Scattering in a Cold Gas of Fermionic Lithium Atoms, *Phys. Rev. Lett* **89**, 273202 (2002).
- [222] J. R. Taylor, *An Introduction to Error Analysis* (University Science Books, 1997).
- [223] D. S. Petrov, Three-boson problem near a narrow Feshbach resonance, *Phys. Rev. Lett.* **93**, 143201 (2004).
- [224] T. Weber, J. Herbig, M. Mark, H.-C. Nägerl, and R. Grimm, Three-Body Recombination at Large Scattering Lengths in an Ultracold Atomic Gas, *Phys. Rev. Lett.* **91**, 123201 (2003).
- [225] C. Lobo, A. Recati, S. Giorgini, and S. Stringari, Normal State of a Polarized Fermi Gas at Unitarity, *Phys. Rev. Lett.* **97**, 200403 (2006).
- [226] A. Frisch, *Dipolar Quantum Gases of Erbium*, Ph.D. thesis, University of Innsbruck (2014).
- [227] M. Kreyer, *Double-stage magneto-optical trap system for fermionic potassium atoms*, Master's thesis, University of Innsbruck, Austria (2017).
- [228] K. Dieckmann, R. J. C. Spreeuw, M. Weidemüller, and J. T. M. Walraven, Two-dimensional magneto-optical trap as a source of slow atoms, *Phys. Rev. A* **58**, 3891 (1998).

- [229] T. Kuwamoto, K. Honda, Y. Takahashi, and T. Yabuzaki, Magneto-optical trapping of Yb atoms using an intercombination transition, *Phys. Rev. A* **60**, R745 (1999).
- [230] A. Frisch, K. Aikawa, M. Mark, A. Rietzler, J. Schindler, E. Zupanič, R. Grimm, and F. Ferlaino, Narrow-line magneto-optical trap for erbium, *Phys. Rev. A* **85**, 051401 (2012).
- [231] A. C. Wilson, C. Ospelkaus, A. P. VanDevender, J. A. Mlynek, K. R. Brown, D. Leibfried, and D. J. Wineland, A 750-mW, continuous-wave, solid-state laser source at 313 nm for cooling and manipulating trapped $^9\text{Be}^+$ ions, *Appl. Phys. B* **105**, 741 (2011).
- [232] F. Sievers, N. Kretzschmar, D. R. Fernandes, D. Suchet, M. Rabinovic, S. Wu, C. V. Parker, L. Khaykovich, C. Salomon, and F. Chevy, Simultaneous sub-Doppler laser cooling of fermionic ^6Li and ^{40}K on the D_1 line: Theory and experiment, *Phys. Rev. A* **91**, 023426 (2015).
- [233] D. Dreon, *Designing and building an ultracold Dysprosium experiment: a new framework for light-spin interaction*, Ph.D. thesis, Paris Sciences Lettres PSL Research University (2017).
- [234] D. O. Sabulsky, C. V. Parker, N. D. Gemelke, and C. Chin, Efficient continuous-duty Bitter-type electromagnets for cold atom experiments, *Rev. Sci. Instrum.* **84**, 104706 (2013).
- [235] N. Gröbner, P. Weinmann, F. Meinert, K. Lauber, E. Kirilov, and H.-C. Nägerl, A new quantum gas apparatus for ultracold mixtures of K and Cs and KCs ground-state molecules, *J. Mod. Opt.* **63**, 1829 (2016).

Acknowledgements

I would like to start by thanking Rudi Grimm for welcoming me into his group, allowing me to build a new experiment, and helping us to explore new results. His unbridled enthusiasm for all things physics really stimulated and motivated me. My thanks also goes out to everyone that has been part of the team, Vincent, Slava, Marian, Elisa, Alex, Emil, and Jeong. It really shows all of your determination that we got most of our breakthroughs on Fridays, and even though our music tastes are wildly different, I do think we complement each other in many ways.

When I started my PhD in Innsbruck, Albert showed me all the ins and outs of an ultracold atom machine, his experience and guidance was of incredible value to my endeavors to build a new experiment. Thank you also to all the people from the ultracold groups, you were a very abundant source of help and good advice.

Both the Iqoqi and experimental physics workshops helped us greatly, by showing me how to design parts that actually can be made, providing a strong pair of hands to empty an old lab, and building many crucial parts of our setup. Here I would especially like to thank Andreas, Toni, Christoph, and Armin, who were able to quickly fix issues we encountered while building our setup, and saved us from serious delays. All my scientific efforts would be fruitless without the continuous support from all the administrative staff, thank you Christine, Verena, Klaus, Elisabeth and Doris.

My special gratitude has to go to the people that made me enjoy my time here in the alps a lot, Rianne, Philipp, Tadas, Milena, Cosetta, and Deborah. Mountaineering and climbing together was truly awesome and a lifelong dream come true. And finally I would like to thank wholeheartedly my younger brother Timo for helping me through tough times, my parents for supporting and motivating me all the way, and my older siblings Lisanne and Simon for their company.

Heel erg bedankt!

Cornee